POROUS NANOFIBERS AS THE HOST FOR ENCAPSULATION AND TUNABLE

RELEASE OF FUNCTIONAL MATERIAL AND STRUCTURAL ENERGY

STORAGE

A Dissertation

by

YIJUN CHEN

Submitted to the Office of Graduate and Professional Studies of
Texas A&M University
in partial fulfillment of the requirements for the degree of

DOCTOR OF PHILOSOPHY

Chair of Committee,	Mohammad Naraghi
Co-Chair of Committee,	James Boyd
Committee Members,	Dimitris Lagoudas
	Hung-Jue Sue
Head of Department,	Rodney Bowersox

May 2020

Major Subject: Aerospace Engineering

ABSTRACT

Encapsulating functional materials inside fibrous structures with the ability to dispense them on demand is an enabling technology that can open new frontiers in developing multifunctional composites and smart textiles. Conventional encapsulation techniques include simultaneous processing of the filler and the fiber (such as co-axial electrospinning and blend electrospinning). These methods often suffer from limited material choices, imposed by the strict material and processing compatibility requirements, and limited dose of the functional material.

In this work, we have investigated the utilization of porous fibers as a platform to store functional materials and energy (ions) and release them on demand. The work has been carried out in two phases. First, we have established a broadly applicable porous fiber encapsulation technique based on sequential processing. In this method, electrically non-conductive or conductive porous fibers are fabricated, subsequently loaded with functional materials and encapsulated by a polymer coating in three different steps. Controllable passive release was demonstrated on non-conductive porous Poly(methyl methacrylate) (PMMA) fibers containing high mass loading of an antibacterial salt (Benzalkonium Chloride) encapsulated with sub-micron PMMA coating. In addition, activate release in response to an electric signal was demonstrated using conductive porous carbon nanofibers (CNF) yarns containing high mass loading of antibacterial material (Gentian Violet) encapsulated by a thin Polycaprolactone (PCL) coating. Active release of the

functional material was achieved by heating up the yarn with Joule heating which facilitate the diffusion of the functional material through the PCL coating.

The second phase of the project was with regards to the use of the porous fibers as structural energy storage platforms. Due to the excellent mechanical properties and the high specific surface area of the porous CNFs, they are also good candidate for multifunctional structural energy storage applications. The trade-off between energy storage and load bearing in porous CNFs was demonstrated for the first time by analyzing porous CNFs activated with KOH with different concentrations and activation temperatures. It was found that moderate activation can lead to dramatic improvement in capacitance(by >300%), at a rather moderate loss in strength($< 17\%$). The gain in specific surface area and capacitance in CNFs is many times those observed in bulk carbon structures, such as carbon fibers, indicating that activation is mainly effective near the free surfaces and for low-dimensional materials.

ACKNOWLEDGEMENTS

CONTRIBUTORS AND FUNDING SOURCES

NOMENCLATURE

AFM	Atomic force microscopy
BAC	Benzalkonium Chloride
BET	Brunauer-Emmett-Teller theory
CD	Galvanostatic charge/discharge
CF	Carbon fiber
CNF	Carbon nanofibers
CNT	Carbon nanotube
CV	Cyclic voltammetry
DCM	Dichloromethane
DI	Deionized Water
DIC	Digital Image Correlation
DMF	Dimethylformamide
ESR	Equivalent series resistance
FEA	Finite Element Analysis
FIB	Focused Ion Beam
GV	Gentian Violet
KOH	Potassium hydroxide
MEMS	Microelectromechanical Systems
NG	Nucleation and growth
PAN	Polyacrylonitrile

PCL	Polycaprolactone
PLA	Polylactic Acid
PMMA	Poly(methyl methacrylate)
PS	Polystyrene
PVDF	Polyvinylidene Fluoride
QSDFT	Quenched Solid Density Functional Theory
RH	Relative humidity
RVE	Representative Volume Element
SD	Spinodal decomposition
SEM	Scanning electron microscope
SSA	Specific surface area
TEM	Transmission electron microscope
TIPS	Thermally Induced Phase Separation
UV	Ultraviolet
UV-vis	Ultraviolet–visible spectroscopy
VIPS	Non-Solvent Vapor Induced Phase Separation
XPS	X-Ray photoelectron spectroscopy

TABLE OF CONTENTS

LIST OF FIGURES

LIST OF TABLES

1. INTRODUCTION [*]

Encapsulating functional materials inside fibers with the ability to release them controllably is an enabling technology that can open new frontiers in developing smart textile/fabrics and adaptable composites. This broadly applicable technology can be used for instance to develop smart and multifunctional textiles and self-healing composites such as wound healing fabrics which contain high concentration of healing agent to be released controllably in contact with body fluid, smart military clothing that can release insect repellents and antibacterial materials in response to rupture caused by combat injury or on-demand by external stimuli, and self-healing composites that repair damage autonomously or on demand by releasing healing agent near damage site.

Fibers which contain functional materials as volumetric inclusions, surface or skin deposits are used in commercial textiles for odor control, UV protection, thermal regulation, and as biocides or insect repellent[1, 2]. Moreover, significant research efforts are devoted to processing fibers for wound dressings[3, 4], drug delivery[5-9] and autonomous self-healing composites[10-13]. It is to be emphasized that there is a clear distinction between encapsulation of functional materials inside fibers, which is the subject of this work, and encapsulation of materials inside particles. The latter is well established with applications in drug delivery or autonomous self-healing composites [14, 15].

---

[*] Part of this section is reprinted with permission from "Porous fibres with encapsulated functional materials and tunable release." by Y. Chen, J. G. Boyd, M. Naraghi, Journal of Microencapsulation, 2017, 34 (4), 383-394. Copyright [2017] by Taylor & Francis and "Promising Trade-Offs Between Energy Storage and Load Bearing in Carbon Nanofibers as Structural Energy Storage Devices." by Chen, Y., Amiri, A., Boyd, J. G., Naraghi, M, Advanced Functional Materials, 2019, 29 (33). Copyright [2019] by American Chemical Society.

Despite the versatility of this technology, current development on encapsulating functional materials in fiber form is at an embryonic stage. Generally, three configurations are used to incorporate substances into nanofibers and microfibers (Figure 1.1): (1) Functional molecules are dissolved[3, 16, 17] or functional particles are dispersed[5, 9, 18, 19] in a polymer solution from which polymeric fibers with molecule/particle inclusions are spun, (2) Particles are attached onto the surface of fibers[20, 21], and (3) the substance is contained coaxially in the fiber during the fiber processing[10, 11, 22, 23].

Many of these methods relies on electrospinning, which is a low-cost and versatile technique to fabricate polymeric, carbon and ceramic fibers with a diameter ranging from tens of nanometers to a few microns. Electrospinning can be easily employed in laboratory or scaled up for industrial process[24]. This method in its various forms has attracted great attention in research in recent decade due to its simplicity and cost-effectiveness. This technique will be briefly reviewed in the next section.
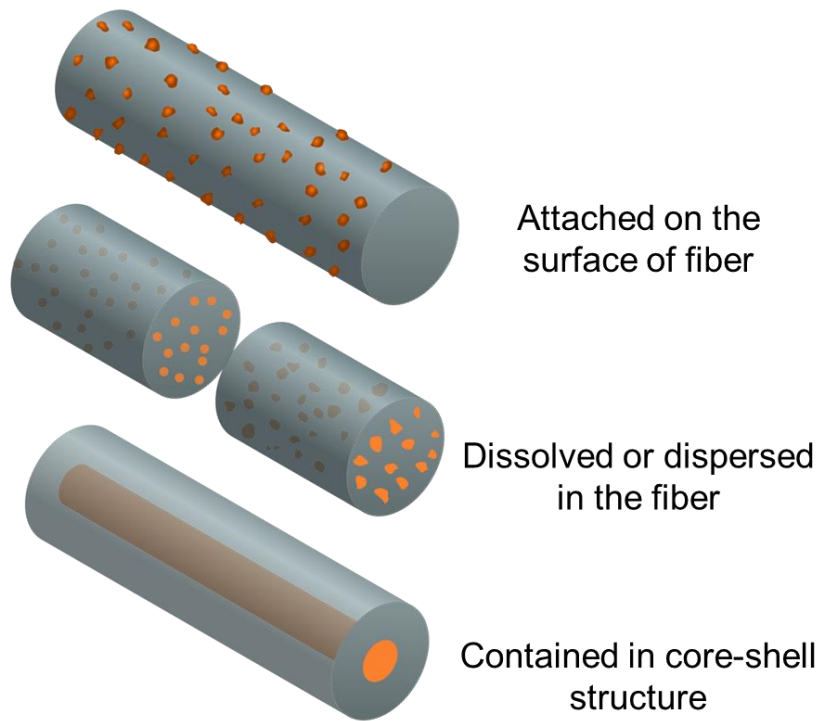
Figure 1.1 Configurations of fiber loaded with of functional materials. Reprinted from [41] with permission.

1.1. Electrospinning

Although the process of electrospinning was introduced in the early 1900s and the patent for commercialized electrospinning dates back to the 1930s. It did not attract much attention until the boom of nanomaterials in the early 2000s. Nowadays it is widely used in multiple engineering and biomedical fields for applications including filtration, textile, composites, energy storage, sensor, drug delivery, tissue engineering and cosmetics[25]. The process for electrospinning is relatively simple: a typical setup for electrospinning is presented in Figure 1.2. The typical electrospinning apparatus consists of four components, a high voltage power supply, a polymer infusion system, a needle which is

3

connected to the high voltage and a grounded target. The polymer source will be fed through the needle into the electric field. The polymer source can be a polymer solution or a polymer melt. The target can be either stationary or moving (including rotary targets to induce fiber alignment).
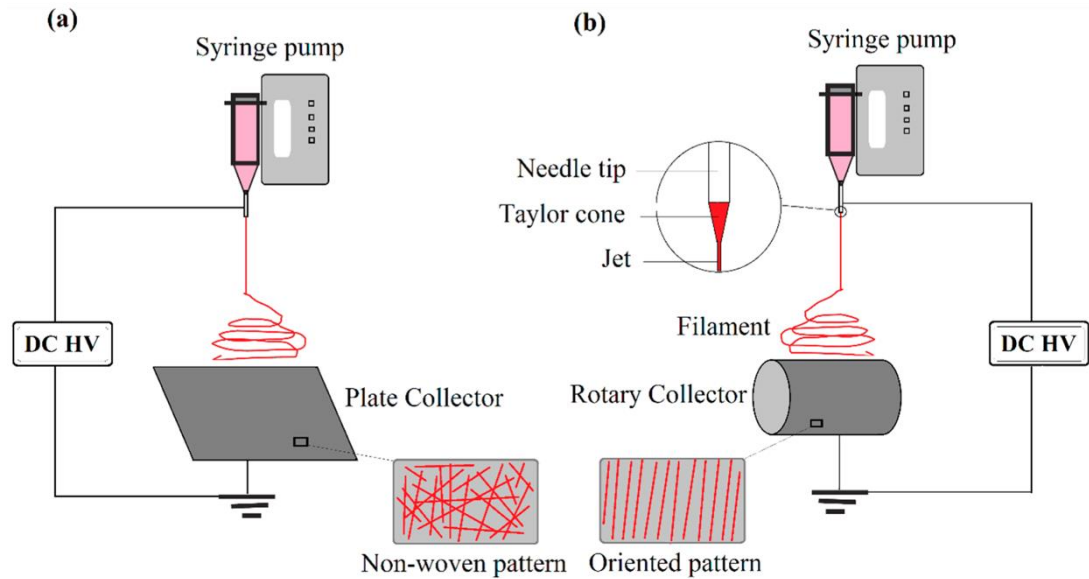
Figure 1.2 Schematic of electrospinning [26]. Reprinted from [26] with permission.

During the electrospinning process, the polymer is charged by the high voltage and form a conical structure at the tip of the needle, which is also known as Taylor cone, its structure is shown in Figure 1.3. When the electrostatic force overcome the surface tension and the viscoelastic force of the polymer droplet, a polymer jet forms at the tip of Taylor cone and the jet will be attracted by the grounded target. During the flight of the jet, it enters a whipping motion due to bending instability caused by the positive charges accumulated on the jet. This whipping motion combined with stretching from the electrostatic force stretches the polymer jets. In addition, the electrostatic repulsion can

also split the polymer jet into multiple jets. As a result, the polymer jets stretch and split into submicron or nanometer size fibers until they are finally collected on the target[25]. Both random and aligned fibers can be collected on the target depending on the type of collector.
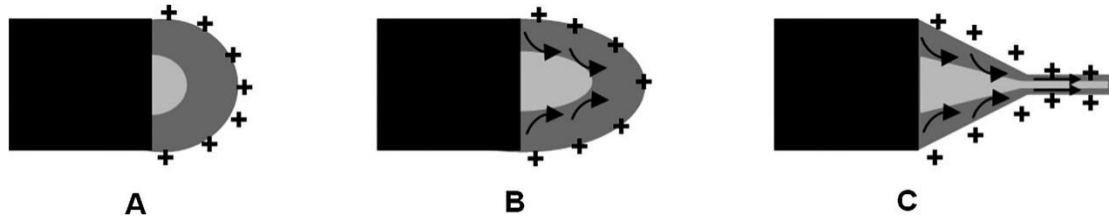
Figure 1.3 Schematic illustration of compound Taylor cone formation. (A) Surface charges on the sheath solution, (B) viscous drag exerted on the core by the deformed sheath droplet and (C) sheath– core compound Taylor cone formed due to continuous viscous drag.[27] Reprinted from [27] with permission.

The electrospinning process is affected by many factors which can be summarized in two categories: solution parameters and set up parameters. The solution parameters include the molecular weight of the polymer, concentration, viscosity, surface tension, evaporation rate of the solvent and electrical conductivity, etc. The set-up parameters include the strength of the electric field, distance between the needle and the collector, pumping rate, temperature and humidity of the environment. All these parameters play an important role in the fiber morphology including fiber diameter, diameter uniformity, shape and microstructure. Many review articles have discussed the contribution of the solution and set-up parameters on the outcome of the electrospinning, including fiber diameter range. Interested readers may refer to these articles[25, 26, 28].

1.2. State of the art method for loading of functional materials in fiber form

Several methods are developed to load functional materials in fiber form using electrospinning or variations of electrospinning as shown in Figure 1.4. These methods include attaching the functional material on the surface, blend electrospinning, emulsion electrospinning and coaxial electrospinning[29].

The most straightforward way to load functional on nanofibers is by physical/chemical attaching the functional material onto electrospun fiber surface[21, 30, 31], as shown in Figure 1.4a,b. Although the process is simple, the lack of control on the release kinetics limits the application of this approach.

Variations of the electrospinning have been developed to encapsulate functional materials in fibers with different structures. For instance, blend electrospinning has been used to encapsulate functional material into fibers[6, 32-34]. Blend electrospinning is based on mixing molecules or nano/micro particles of functional material with the polymer solution (Figure 1.4b) prior to electrospinning process. The functional material is dissolved or dispersed in the polymeric matrix. However, solubility requirements of functional material inside polymer solution imposes considerable restrictions on mass loading and type of functional materials that can loaded onto the fibers.
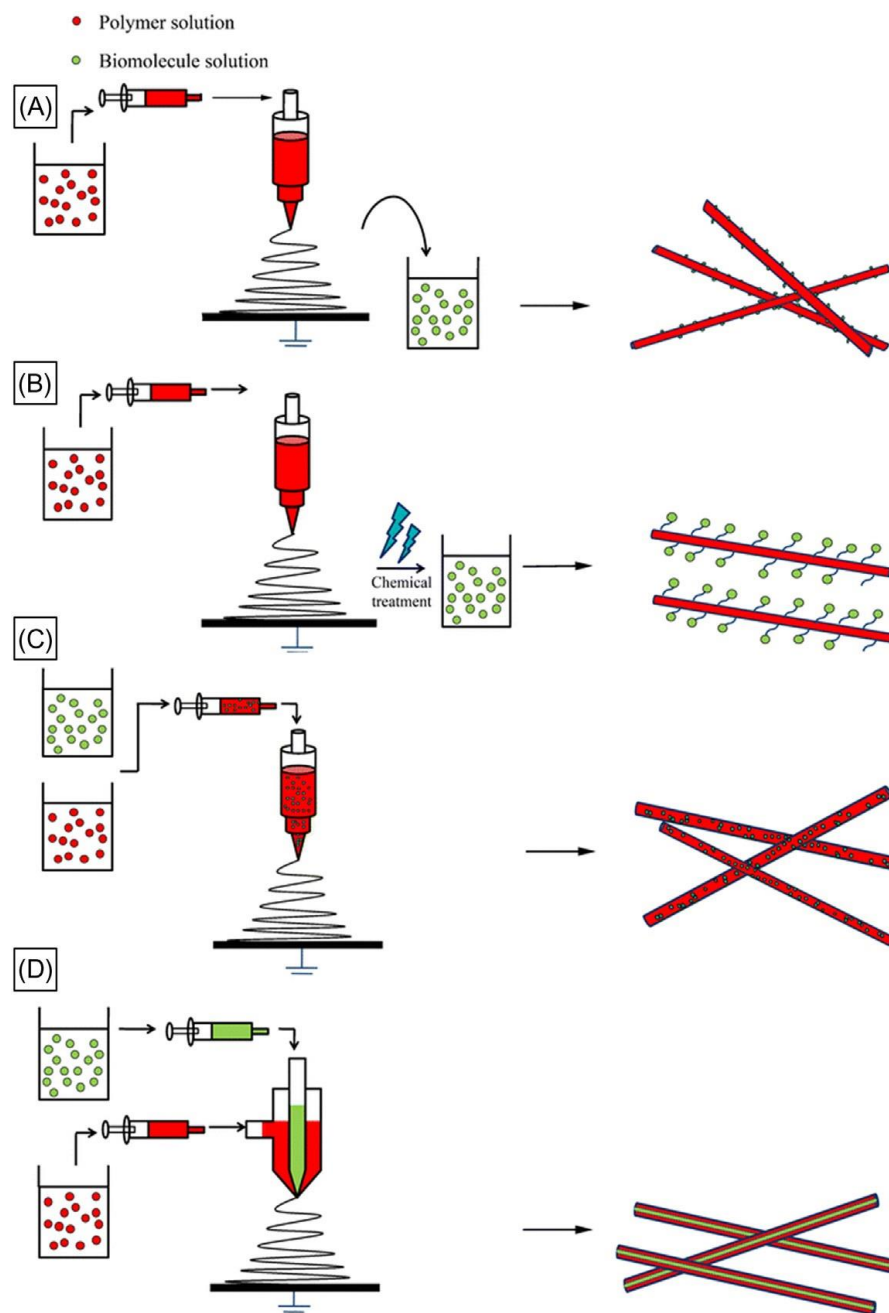
Figure 1.4 Functional material loading method for electrospun fibers: (A) physical adsorption; (B) covalent immobilization; (C) blend/emulsion electrospinning; and (D) coaxial electrospinning.[24] Reprinted from [24] with permission.

Emulsion electrospinning is another technique to fabricate multicomponent fibers to encapsulate functional materials in fiber form[35, 36]. It is similar to blend electrospinning, instead of direct dissolving or mixing the functional material with the polymer solution, a stable emulsion of two or more liquid is used. The liquid can consist of different functional materials and a polymer solution. To form the stable emulsion, it often requires surfactant to form either water-in-oil or oil-in-water emulsion. However, requirements for solubility/insolubility between phases (polymer solution, surfactant and encapsulated phase) substantially limits material selection and scope of the applicability of the technology.

To develop a continuous phase of functional material within a fiber, coaxial electrospinning has been developed[37-39] as shown in Figure 1.4d. In coaxial electrospinning, a coaxially aligned needle is used instead of a single needle, two different liquid can be pump to the two needles. The Taylor cone in coaxial electrospinning will be formed with the core solution surrounded by the shell solution, as a result, a core-shell structure fiber can be obtained. In addition to the parameters that affect the electrospinning, the interaction between the two liquid also plays an important role in the fiber morphology. For successful coaxial electrospinning, the shell solution must be electro-spinnable. In other words, the molecular weight, concentration, and entanglement of polymeric chains must be sufficient to produce stable fiber jets. On the other hand, the core solution does not have to be electrospinnable (such as liquid with low viscosity). In addition, the two solution must be immiscible and the interfacial tension between two liquid must enable drawing of core liquid.[29] These processing parameters of

electrospinning may significantly limit material selection and effectiveness of this approach.[37] In addition, the slow release through a solid polymer shell can be another limiting factor for this technique[40].

1.3. Proposed method for encapsulation of functional materials through a porous fiber platform

The existing methods to encapsulation functional material inside the fibers (blend, emulsion and coaxial electrospinning) are all limited one way or another. Despite the difference in the techniques, they all have one characteristic in common: all of them involve simultaneous processing of the fiber and encapsulated material. This imposes significant limitations in terms of material selection and morphology of the functional material loaded fibers. For example, the axial continuity of the encapsulated materials/particles in blend/coaxial electrospinning is often very poor and cannot be adjusted. Axial connectivity, when the encapsulated material is electrically/thermally conductive, can turn an otherwise nonconductive fiber into a passage to transfer charges and heat along the fiber. Moreover, axial continuity of the encapsulated functional material can be used to adjust the quantity of the material that will be released in response to local damages occurring to the fiber, e.g. fiber or coating fracture or degradation of the coating. This can be used, for example, to release controlled dose of antibacterial agents around a flesh wound when the fibers are fractured, or the coating is dissolved in contact with body fluids. Second, although encapsulated material in coaxial electrospinning is axially continuous, processing parameters of electrospinning significantly limit material selection

and effectiveness of this approach as discussed earlier. Moreover, post-electrospinning fiber treatments, for instance to change the microstructure of the fiber, will be limited to those treatments that will not harm the encapsulated material. For instance, this technique cannot be used to make carbon fibers via carbonizing a polymeric fiber without degrading the embedded functional material.

In contrast, we propose a novel method to encapsulate materials inside fibers with distinct advantages compared to the existing methods. Our approach is based on sequential processing of porous fibers, encapsulated materials and coatings, as shown in Figure 1.5. In this method, porous fibers are first fabricated by electrospinning, although the encapsulation method can also be applied to fibers made with other processing techniques. Second, the porous fibers are loaded with the functional materials. In the last step, porous fibers are coated with a polymer coating to encapsulate the functional material. The coating serves the purpose of adjusting the release of loaded material.
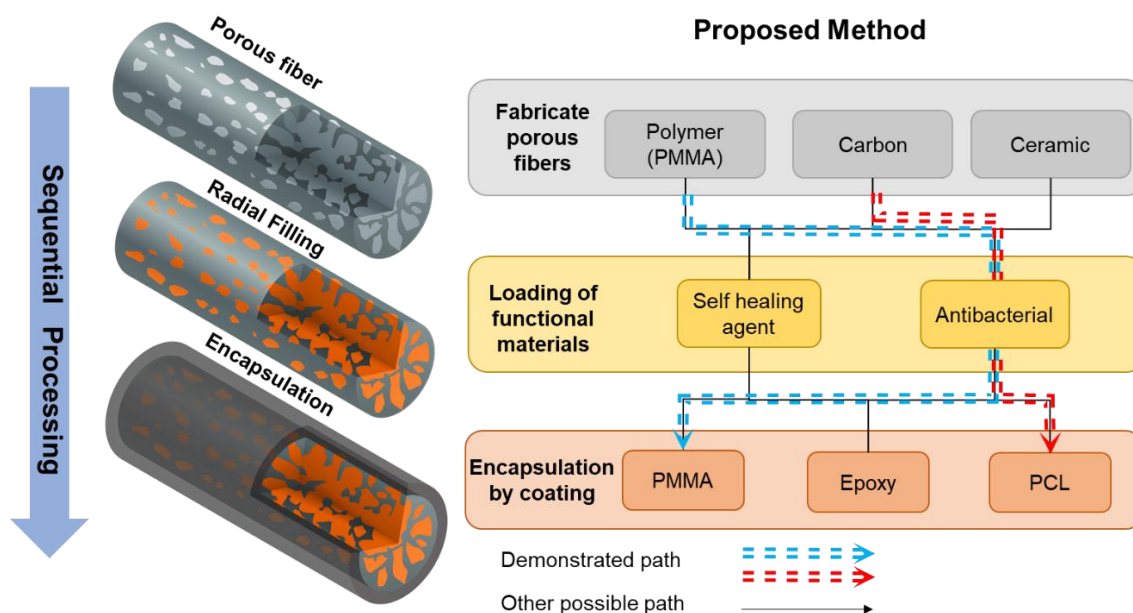
Figure 1.5 Schematic of our proposed methods for encapsulating substance in fiber form based on sequential processing of porous fibers, loading the porous fiber with functional material, followed by encapsulation with a polymer coating[41]. Reprinted from [41] with permission.

This sequential processing proposed here is relatively material agnostic which allows for greater freedom in selection of fiber/functional material/coating material combinations. Since the porous fiber is processed independent of the functional materials, it can be processed using methods that are incompatible with or would degrade the functional material. As an example, the fiber can be made of a pre-ceramic/pre-carbon polymer that is pyrolyzed to form a ceramic or porous carbon (electrically conducting fiber). Different types of functional (liquid or solid dissolve in solvent) can be loaded into the porous fiber with high mass loading through capillary effect. In the final coating process, different type of polymers can be coated with a dip or spray coating process.

In addition, the release mechanism of our porous fiber based platform can be highly flexible compared to existing methods. In existing method, the release rates are controlled by diffusion of the loaded material in the polymers, the release kinetics are mainly determined by the material property and distance of the diffusion, i.e. the size of the fibers in blend/emulsion electrospinning or the thickness of the shell in coaxial electrospinning. In our method, the coating property (thickness, or permeability) determines the release kinetics, which can reliably be adjusted independent of the previous steps (fiber fabrication and loading).

On top of that, our method enables on-demand and active dispensing the functional material in response to external stimuli such as fiber fracture or electric signal. For instance, an electric current passed through an electrically conducting porous fiber, such as a carbon nanofiber, can heat the fiber by Joule heating[42, 43], thereby facilitate the diffusion of the functional material through the coating by increasing the diffusion coefficient[44, 45], or in extreme cases melt the coating for large dose dispensing. The proposed release mechanisms are presented in Figure 1.6. A table is used to summarize the pros and cons of our proposed method and existing method is shown in Table 1.1.
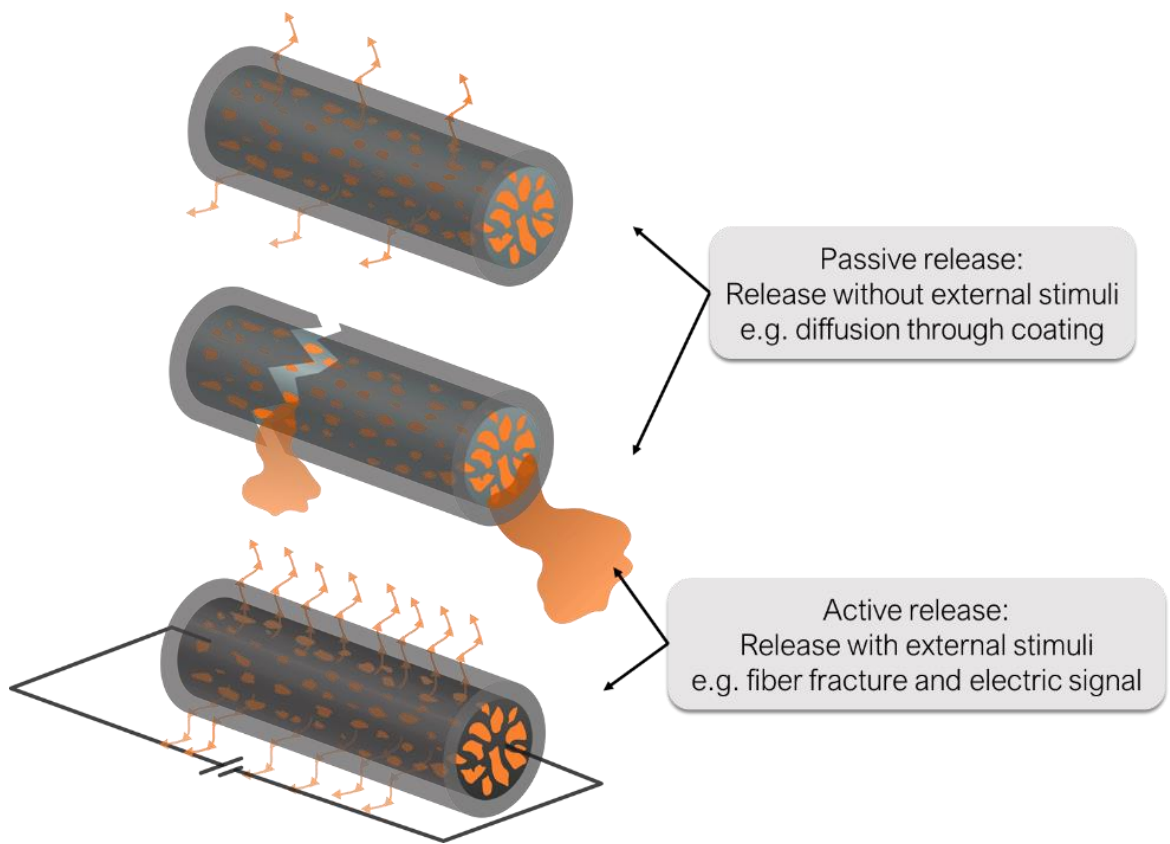
Figure 1.6 Schematics of proposed release mechanisms.

Table 1.1 Comparison of different fiber encapsulation method

Encapsulation method	Process simplicity	Material selection	Mass loading%	Adjustable release mechanism
Blend electrospinning	+ +	-	- -	- -
Emulsion electrospinning	+	+	+	+
Coaxial electrospinning	+	-	+	--
Porous fiber platform	+	+ +	+ +	+ +

1.4. State of the art multifunctional structural energy storage materials

In case of conductive porous fibers, their high porosity and surface area will also make them suitable candidates for energy storage applications. For this purpose, the multifunctional structural energy storage device will be introduced in this section.

The growth in electric vehicles, consumer electronics and wearable technology has created an ever-increasing demand for higher energy density in energy storage devices such as lithium ion batteries and supercapacitors. Despite the tremendous efforts worldwide, energy density in the electrochemical storage devices has grown at a rather slow rate (less than 10% per year)[46]. Recent efforts to improve the effective energy density relies on multifunctional materials, in which energy storage can be combined with other functionalities to achieve weight or volume savings on a system's level[47, 48]. In weight-sensitive applications such as ground and air vehicles with electric propulsion, the energy storage device and the structural frame are usually the heaviest components. Naturally, significant weight saving can be achieved by combining these functionalities through the development of structural energy storage materials[49]. In traditional energy storage devices such as lithium ion batteries and supercapacitors, the electrochemically active material does not carry external loads applied to the structure, and the mechanical integrity of the devices relies on the packaging material, which adds additional weight to the system. In structural energy storage, the electrode simultaneously stores energy and carries load, allowing for electrochemical energy storage in load-bearing frames to achieve energy storage with minimal weight penalty.

Different types of energy storage devices such as batteries[50-53] and supercapacitors[53, 54] have been investigated for structural energy storage. Among them, supercapacitors show great potential as structural energy storage due to their rather simple laminated structure, which is similar to laminated structural composites[48, 55]. Supercapacitors usually have a laminated structure which consists of two electrodes and a separator which is filled with electrolyte, as shown in Figure 1.7. The energy is stored in the electrostatic double layer at the electrode-electrolyte interface. Their specific energy is proportional to the specific surface area (SSA) of the electrodes. On the other hand, high SSA in supercapacitors is regularly achieved via developing highly porous structures, and the pores may adversely affect strength by inducing stress concentration. Therefore, there seems to be a tradeoff between these functionalities which needs to be evaluated.
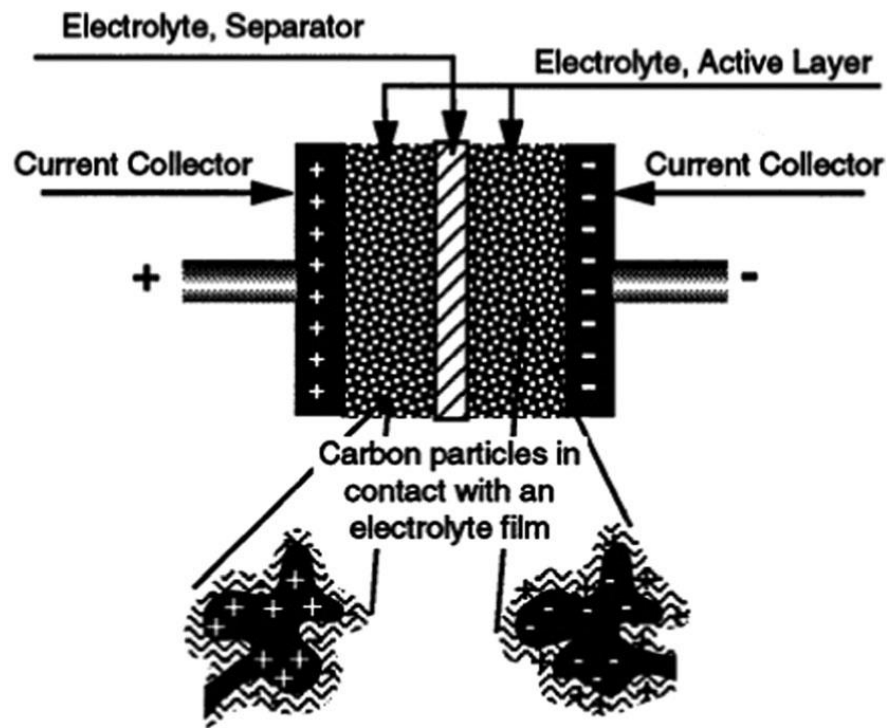
Figure 1.7 Schematic of supercapacitor[56]. Reprinted from [56] with permission.

Several carbon nanostructures with good mechanical properties, excellent electrical conductivity, excellent chemical resistance and high SSA such as carbon nanotube (CNT)[46, 57] and graphene[58-61] have been employed. Individual CNTs can have a strength over 10 GPa (reported also to be as high as 100 GPa)[62, 63] and a modulus over 320 GPa[64], and graphene has a strength over 12 GPa and a modulus around 1 TPa[65]. Although the individual CNT and graphene have excellent mechanical properties, the structural performance of the electrode made with graphene and CNT is still far from ideal, the specific capacitance and strength of graphene and CNT based electrode from literature are summarized in **Figure 1.8**. Plain graphene electrodes usually show a tensile strength less than 10 MPa[58, 61]. Many researchers attempt to improve the mechanical properties of graphene electrodes by adding reinforcement and binders[59, 60, 66]. Graphene paper electrodes containing aramid nanofiber showed a balance between the structural and energy storage functions, a capacitance of 121 F/g and a tensile strength of 100.6 MPa[59]. CNT based structural electrodes have slightly higher mechanical properties comparing to their graphene-based counterparts[46, 67-71]. A nanomembrane based on CNT sheet reached a strength of 135 MPa and a capacitance of 67 F/g[69]. A CNT/PANI composite electrode demonstrates a strength of 484 MPa with a capacitance of 230 F/g[46]. CNT buckypaper coated with polypyrrole achieved a strength of 68.7 MPa and a capacitance of 320 F/g[68]. A high strength CNT yarn (367 MPa) was used in a supercapacitor to achieve a high volumetric capacitance of 179 F/cm.[71] Continuous CNT fibers[70] were also used as structural supercapacitor electrode with a capacitance of 28 F/g, but a relatively low strength of 53 MPa was reported. Despite various strategies to improve the mechanical

16

properties of graphene and CNT based electrodes, there is still a large gap between the remarkable mechanical properties of CNT and graphene, and the low mechanical properties of electrodes. This is mostly due to the discontinuity of the nanoparticles as reinforcement and the insufficient bonding strength between the nanoparticles and the surrounding matrix material.
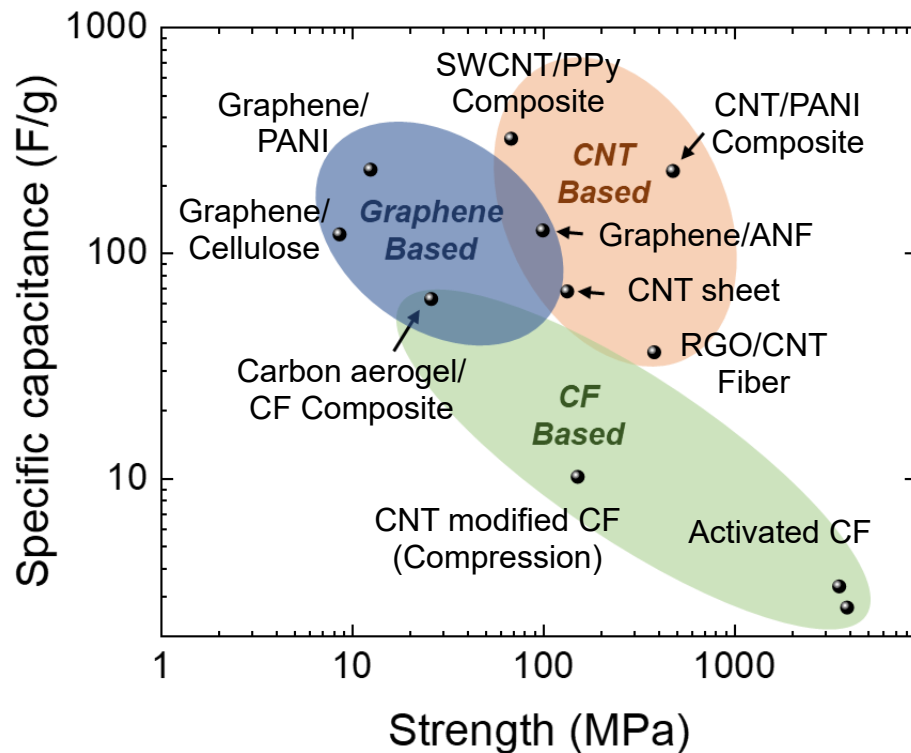
Figure 1.8. Ashby plot of specific capacitance vs strength for structural supercapacitor electrode materials in literature[72]. Reprinted from [72] with permission.

One way to get around this limitation and realize the optimum mechanical properties for structural energy storage is to use continuous reinforcement such as carbon fiber (CF). CFs have typical strength of 3-6 GPa and modulus of 200-300 GPa. CF-based structural energy storage have excellent mechanical properties.[47, 73-76] However, most CF-

based structural supercapacitors have low capacitance due to low SSA.[47, 74, 75] For instance, CFs activated with KOH with single fiber strength up to 3960 MPa were used in structural supercapacitors, but a relatively low SSA of 21.3 m^2/g (comparing to over 2000 m^2/g for graphene[77]) and a low capacitance of 2.63 F/g were achieved.[75] Various methods have been attempted to improve the capacitance of CF-based supercapacitors by modifying CFs with nanomaterial such as CNT,[55, 73] conductive nanowire[78, 79] and carbon aerogels.[80, 81] However, the capacitance of such capacitors is still relatively low compared to the graphene and CNT based counterparts.[47]

Carbon nanofibers (CNFs) derived from electrospun polymer fibers attracted great attention as supercapacitor electrode material in recent years due to their high SSA, excellent electrical conductivity and structural stability.[82] Various forms of electrospun CNFs,[82] such as porous CNFs,[83, 84] hollow CNFs[84, 85] and activated CNFs[86-90] have been used as electrodes in supercapacitors and capacitance up to 200 F/g has been achieved.[82] The higher capacitance of CNFs relative to CFs is attributed to their much higher surface-to-volume ratio (it scales inversely with the diameter of the fiber). The much higher SSA in CNFs also facilitates further enhancement of available surface area by means of activation. Meanwhile, recent studies have showed the excellent mechanical properties of electrospun CNFs,[91-93] a tensile strength and modulus of 7.6 GPa and 268 GPa was recently reported for individual CNFs.[91] Our previous work has also demonstrated the possibility of using high surface area porous CNFs as a load-bearing material.[49]

Porous CNF shares similar continuous structure as CF and CNF, thus, they may be good candidate for load bearing. At the same time, the porous structure offers abundant

18

surfaces for energy storage. In energy storage application, the energy density is proportional to the SSA of the electrode material. However, higher SSA requires more pores in the fibers which will reduce the load bearing capability of the structures by inducing stress concentration. Apparently, there is a trade-off between the energy storage and load bearing in porous CNFs.

1.5. Research objectives and outlines

As discussed in previous sections, the porous fiber based platform for encapsulation and release of functional material as well as ions is inherently advantageous than existing methods both during processing and in service. During processing, it offers a wider range of material selection. In service, it allows for highly flexible release mechanisms, including controllable release rate and release on demand. Despite these advantages, using porous fiber for this purpose have never been explored before and a lot of challenges still exist. One of the issues is on how to fabricate porous fiber, both conductive and non-conductive, with the desired microstructure and morphology which can maximize the loading of functional materials and how to enable controlled and adjustable release mechanisms of functional material. Another issue is on how to encapsulate the functional materials in the porous fibers with a polymer coating with controllable permeability which allows for controllable and active release.

In addition, the application of porous CNF in structural energy storage with a focus on identifying the tradeoffs between energy storage and load bearing (arising from the peculiar microstructure-property relations in each application) is also unexplored.

Challenge exists on how to design pore structure in the porous conductive fibers to achieve a minimum penalty on the mechanical performance and at the meantime maximizing the energy storage capacity.

To address the above challenges, my overarching goal is to establish the science and technology of using porous/hollow fiber as host for encapsulation and passive/active release of functional materials in response to external stimuli and structural energy storage. To achieve this goal, we have pursued these objectives:

- **Objective 1** (Chapter 2): Investigate the processing-morphology relationship for electrically non-conductive and conductive nanofibers.

- **Objective 2** (Chapter 3): Develop encapsulation method and investigate passive release of functional materials from non-conductive porous nanofibers.

- **Objective 3** (Chapter 4): Investigate active release of functional material in conductive porous fibers.

- **Objective 4** (Chapter 5): Investigate the trade-off between energy storage and load bearing in porous CNF as structural energy storage materials.

- The conclusion of all objectives and proposed future directions are discussed in Chapter 6.

2. PROCESSING-MORPHOLOGY RELATIONSHIP FOR ELECTRICALLY NON-CONDUCTIVE AND CONDUCTIVE NANOFIBERS[*]

Depending on the type of application, either electrically conductive or non-conductive porous fibers may be of interest. For example, in the application of encapsulation and passive release of functional material, such as in response to fiber fracture or timed release via diffusion, a non-conductive porous fiber could serve the purpose. Whereas in applications such as active release in response to an applied voltage and energy storage, a conductive porous fiber needs to be used either to generate heat through Joule heating or to conduct electrons. In all these cases, the morphology of these porous fibers is critical for fulfilling these functions. In encapsulation and release application, the porosity determines the amount of space available for the loaded material, and the connectivity of pores governs how the material can be loaded and released. In structural energy storage applications, the specific surface area of the porous fibers determines how much charges the materials can hold on the surface, and the shape and orientation of the pores determines the mechanical properties of the porous fibers. These factors are mainly determined by the fabrication process of the porous fibers. Therefore, understanding how the processing conditions affect the fiber morphologies is a critical step to successfully develop application-specific porous fibers.

---

[*] Part of this chapter is reprinted with permission from "Porous fibres with encapsulated functional materials and tunable release." by Y. Chen, J. G. Boyd, M. Naraghi, Journal of Microencapsulation, 2017, 34 (4), 383-394. Copyright [2017] by Taylor & Francis and "Mechanics of Emulsion Electrospun Porous Carbon Fibers as Building Blocks of Multifunctional Materials." by Chen, Y., Cai, J., Boyd, J. G., Kennedy, W. J., Naraghi, M, ACS Applied Materials & Interfaces, 2018, 10 (44), 38310-38318. Copyright [2018] by American Chemical Society

In this chapter, the existing fabrication methods for both type of porous fibers will be first reviewed. The fabrication of both conductive (carbon) and non-conductively (PMMA) porous fibers is investigated by experiments to develop porous fibers which are suitable for application of encapsulation/release and structural energy storage. The morphology-processing condition relationship will be discussed in detail.

2.1. Existing fabrication techniques for porous fibers

Several methods have been developed to fabricate porous fibers through electrospinning or its variation. These methods are based on mechanisms mainly categorized into two types: the first takes advantage of the phase separation and the other on relies on the selective removal of a sacrificial component. In this section, these methods for fabricating porous fibers will be reviewed.

2.1.1. Fabrication of porous fiber through phase separation

The most commonly used method to make porous fibers takes advantage of thermodynamics of electrospinning to form pores during electrospinning. These methods are based on solution phase separation and formation of breath figure. When phase separation occurs, thermodynamically unstable polymer solution separates into two phases: polymer rich and solvent rich phase. The evaporation of solvent in solvent rich phase during electrospinning leads to pores.

There are two methods to induce phase separation[94-96]: thermally induced phase separation (TIPS) and non-solvent vapor induced phase separation(VIPS). In both cases,

a highly volatile solvent is necessary. The TIPS requires a temperature drop caused by solvent evaporation[95, 97, 98], while VIPS requires water vapor to be condensed on the fiber surface due to the evaporative cooling to diffuse into the solution and induce phase separation. In water vapor-based VIPS, the electrospinning solvent dissolves in condensed water, and water is often a non-solvent for the polymer, thus, leading to the formation of polymer rich and solvent rich phases. The latter will eventually form pores.

Both TIPS and VIPS have been studied to find relation between the microstructure and factors including: relative humidity[96, 97, 99-103], temperature[101] and solvent volatility[95, 104, 105]. Different polymers have also been investigated such as Poly(methyl methacrylate) (PMMA)[95, 97, 100, 106, 107], polyacrylonitrile (PAN)[108-110], polystyrene (PS)[95, 96, 100, 102, 103, 105, 111-115] and polylactic acid (PLA)[94, 100, 104, 116].

Water vapor condensed on the surface of fiber also causes another mechanism referred to as breath figure. Breath figure was first discovered by Srinivasarao[117] in film casting under high relative humidity; water droplet condensed on the surface leave imprints after drying. This mechanism was used in electrospinning to explain pore formation on the fiber surface under high relative humidity[112, 118].

Different internal pore structures can form via phase separation. Based on composition and temperature of the solution, phase separation can occur by two mechanisms: spinodal decomposition (SD) and nucleation and growth (NG)[96]. Different internal pore structures form through different mechanisms. Interconnected pore structure is characteristics of SD, while closed pore structure is a result of NG[119]. In case of encapsulation and release application, interconnected pore structure is preferred because

23

of its high porosity and the fact that the interconnected pore provides path to fill the entire porous fibers.

2.1.2. Fabrication of porous fiber via multicomponent fibers and selective removal of one component

The other method involves electrospinning a multicomponent fiber then selectively remove one of the component through a post spinning treatment, different form of the second component have been incorporated using method including: emulsion electrospinning of a polymer blend and selective removal of one component[94, 120-122], and templating with sacrificial particles[123-125].

In this regard, various forms of CNF, such as porous CNF[84, 85, 126-128], hollow CNF[85, 128, 129] and activated CNF[127], have been used as electrodes in energy storage devices due to their excellent electrical conductivity, large specific surface area and good structural stability[82]. Electrospinning is commonly used to fabricate the precursors of CNFs out of polymers such as Polyacrylonitrile (PAN), Polyvinylidene fluoride (PVDF) and lignin. Among these polymers, PAN is the most widely used due to its excellent spinnability, low cost and high carbon yield [85]. The porosity can be induced by incorporating sacrificial components in the precursor[123, 128, 130-133], which can be decomposed during pyrolysis to form pores. Examples of sacrificial component are Poly(methyl methacrylate) PMMA[130, 132, 134], Polystyrene(PS)[122] and SiO_2 [126, 135]. To further increase the specific surface area, a sacrificial core can be added to the fibers by coaxial electrospinning to make hollow CNF[84, 85, 128].

2.2. Non-conductive porous nanofibers

To fabricate non-conductive porous fibers, the phase separation method was identified as the ideal method due the simplicity of its process and the high porosity that can be achieve. The experimental work on the fabrication of porous PMMA fibers will be presented in this section. As discussed in the previous section, the relative humidity (RH) and the volatility of the solvent are the most important parameters that determines the microstructure of the porous fibers fabricated through phase separation. The influence of these parameters will be analyzed to maximize the porosity to achieve high mass load for the encapsulation purpose.

2.2.1. Experimental method

Fabrication of non-conductive porous nanofibers:

PMMA (Mw ~350,000 g/mol) (Sigma-Aldrich) was dissolved at 10 wt.% in a binary solvent of dichloromethane (DCM) and dimethylformamide (DMF), both obtained from Sigma-Aldrich. The solvent ratios, DMF:DCM, were 0:1, 1:8, 1:4 and 1:3. Mixtures of PMMA and solvent were stirred for 6 hr before use. Fibers were made by electrospinning the PMMA solution at a feeding rate of 2ml/hr, a needle-to-collector distance of 10 cm and voltage of 22 kV. Electrospinning was conducted horizontally in a chamber with controllable relative humidity ranging from 20±2% to 95±2%, and the temperature inside the electrospinning chamber was 25±1°C for all experiments. A rotating drum collector was used to collect the fibers. The electrospinning setup is shown in Figure 2.1. To control relative humidity during the electrospinning process, an air hose

connected to a flask filled with boiling water is inserted into the chamber as a source of water vapor.
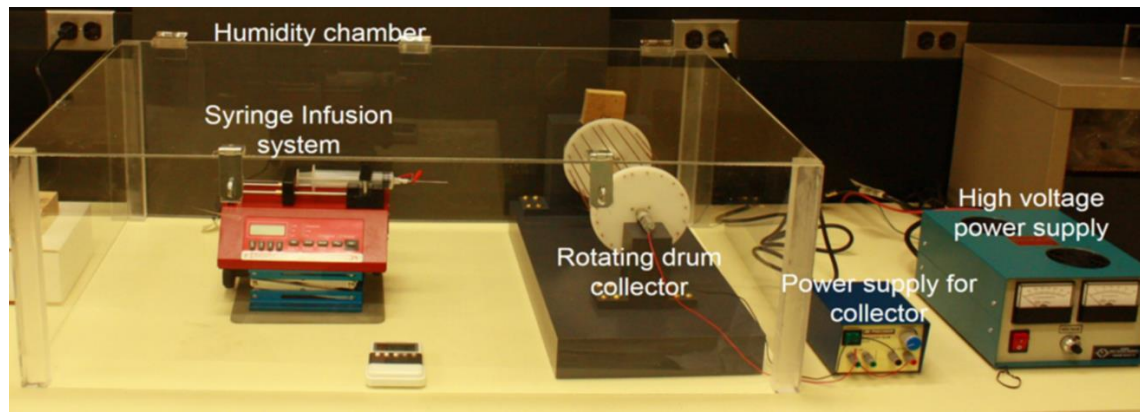
Figure 2.1 Electrospinning setup.

Microstructure characterization:

After electrospinning, the fiber mat was collected from the drum and the microstructure of the fiber surface and cross-section were observed in field-emission scanning electron microscope (FEI Quanta 600 FE-SEM). An accelerating voltage of 20 kV was used for all images. Before imaging, the fibers were coated with a 10 nm layer of Pt/Pd using sputter coater (Cressington 208HR sputter coater) to prevent charging during imaging. This layer cannot be directly discerned in the SEM images, but it highly enhances the image quality and contrast. To study the internal pore structure, the fibers were fractured before imaging. To this end, the fibers were attached to a piece of carbon conductive tape and then cut with a razor blade in liquid nitrogen. The latter was used to minimize plastic deformation of the sample and preserve its internal structure during fracture. The fractured surface was then observed via SEM.

2.2.2. Results and discussion

Effect of phase separation on the morphology of porous nanofibers:

Relative humidity (RH) and solvent volatility, controlled by using a binary solvent system composed of different ratios of volatile and non-volatile solvents, were chosen as processing parameters to study the formation of pores in electrospun PMMA fibers. The volatile and non-volatile solvents were dichloromethane (DCM) and dimethylformamide (DMF), respectively, different mixing ratio results in different volatility for the solvent. To this end, four DMF:DCM ratios (0:1, 1:8, 1:4 and 1:3) were studied at different RHs (from $20 \pm 2\%$ to $90 \pm 2\%$).

Porous PMMA fibers fabricated at DMF:DCM = 0:1 (DCM only) and various RH are presented in Figure 2.2. At RH = $30 \pm 2\%$, the fibers were nearly solid (Figure 2.2a). When RH was increased to $50 \pm 2\%$, regions with separate pores which are mostly spherical, reminiscent of NG, which was discussed in Section 2.1.1, began to emerge in the core of the fibers (Figure 2.2b). When further increasing RH to $90 \pm 2\%$, the pore structure became much larger. Furthermore, the pores become irregular in shape and this pore structure spread across the entire fiber cross-section, suggesting pore interconnection and SD (Figure 2c), as discussed in Section 2.1.1.
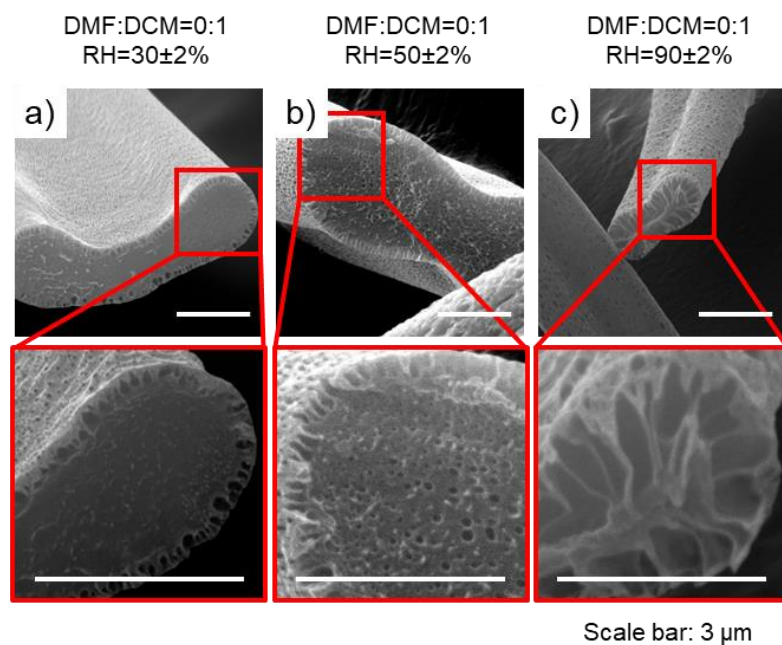
Figure 2.2 Porous PMMA fibers fabricated at DMF:DCM = 0:1. Reprinted from [41] with permission.
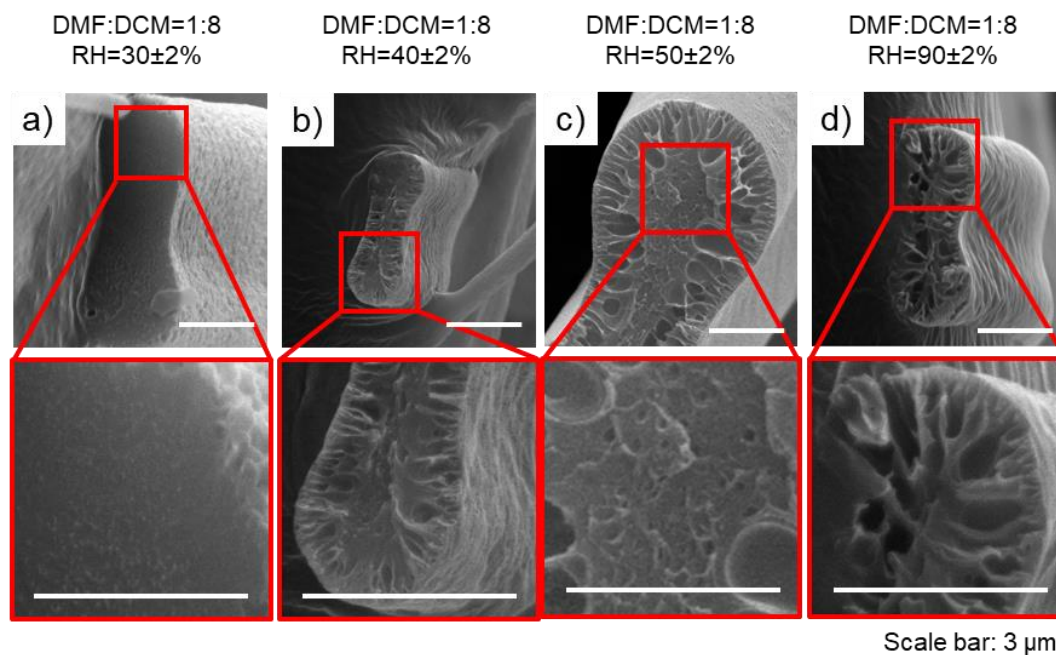
Figure 2.3 Porous PMMA fibers fabricated at DMF:DCM = 1:8 Reprinted from [41] with permission.

A similar trend in the evolution of the pore structure was also observed for DMF:DCM = 1:8, as shown in Figure 2.3. At low RH (30±2%), solid fibers were obtained, while with increasing RH (40±2%, 50±2% and 90±2%), larger pores with irregular shapes, reminiscent of SD, start to appear in the skin of fiber and finally occupy the entire fiber cross-section. Figure 2.4a,b shows fibers fabricated at DMF:DCM = 1:4, RH=50±2% and 90±2%, respectively. At lower RH (50±2%), solid fibers were obtained, while at higher RH (90±2%), SD regions with interconnected pores occupy the entire fiber. At higher relative non-volatile solvent content of DMF:DCM = 1:3, solid fibers were obtained for all RH (Figure 2.4c).
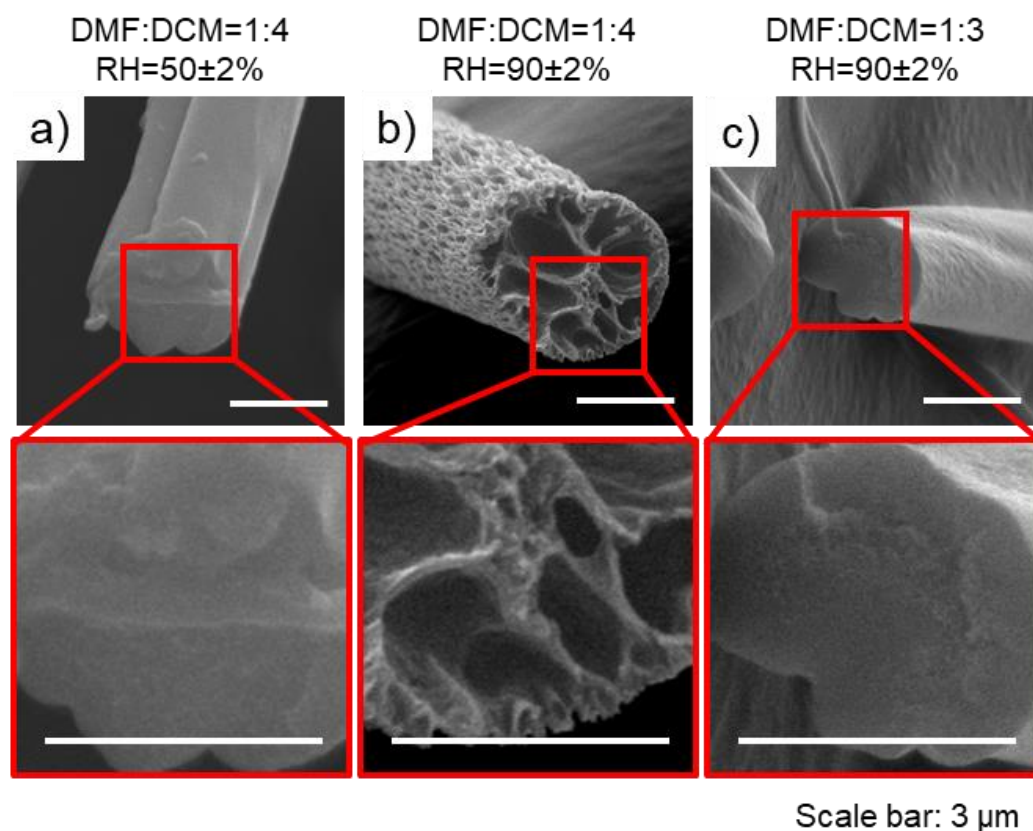
Figure 2.4 Porous PMMA fibers fabricated at DMF:DCM = 1:4 and 1:3. Reprinted from [41] with permission.

In addition to the porous structure, the fiber cross section geometry was also influenced by solvent volatility. A flat ribbon-like fiber geometry was observed at low DMF:DCM ratio (0:1 and 1:8) (Figure 2.2 and Figure 2.3). This geometry is a result of the buckling instability caused by fast solvent evaporation during electrospinning as reported by researchers[103, 136]. By increasing the DMF:DCM ratio to 1:4, the solvent volatility is reduced as well as the buckling instability, therefore circular fibers were obtained, as shown in Figure 2.4.

In order to analyze the pore formation mechanism, a map is used to summarize the porous structure as a function of the DMF:DCM ratio and RH as shown in Figure 2.5. Four different regions are identified on the map based on the type of pore that were observed on the SEM images. Region (I) corresponds to non-porous fibers (also shown in Figure 2.3a and Figure 2.4a,c), region (II) corresponds to fibers with solid core and likely SD skin (also shown in Figure 2.2a & Figure 2.3a), region (III) corresponds to fibers with likely NG core and SD skin (also shown in Figure 2.2b & Figure 2.3c) and region (IV) corresponds to fibers with interconnected pores, likely formed due to SD (also shown in Figure 2.2c, Figure 2.3d & Figure 2.4b).
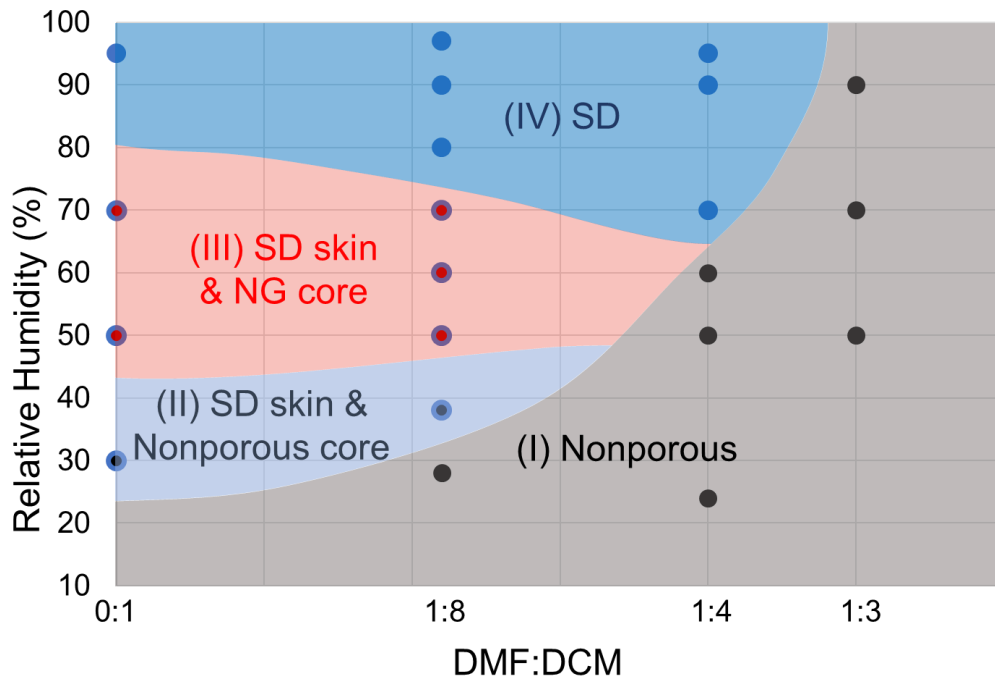
Figure 2.5. Summary of pore formation mechanisms at different RH and DMF:DCM ratios. Reprinted from [41] with permission.

A qualitative polymer-solvent-nonsolvent phase diagram which explains the pore formation in our fibers and in all four regions is shown in Figure 2.6. During electrospinning, as the polymer jet travels towards the collector, three types of composition paths are expected. In all cases, the arrows show the progress of the electrospinning in which the polymer concentration increases with time. The non-solvent in this figure is water which condenses on the fiber from the environment. As the jet is cooled down due to solvent evaporation, the amount of non-solvent scales with the relative content of the volatile solvent and humidity.
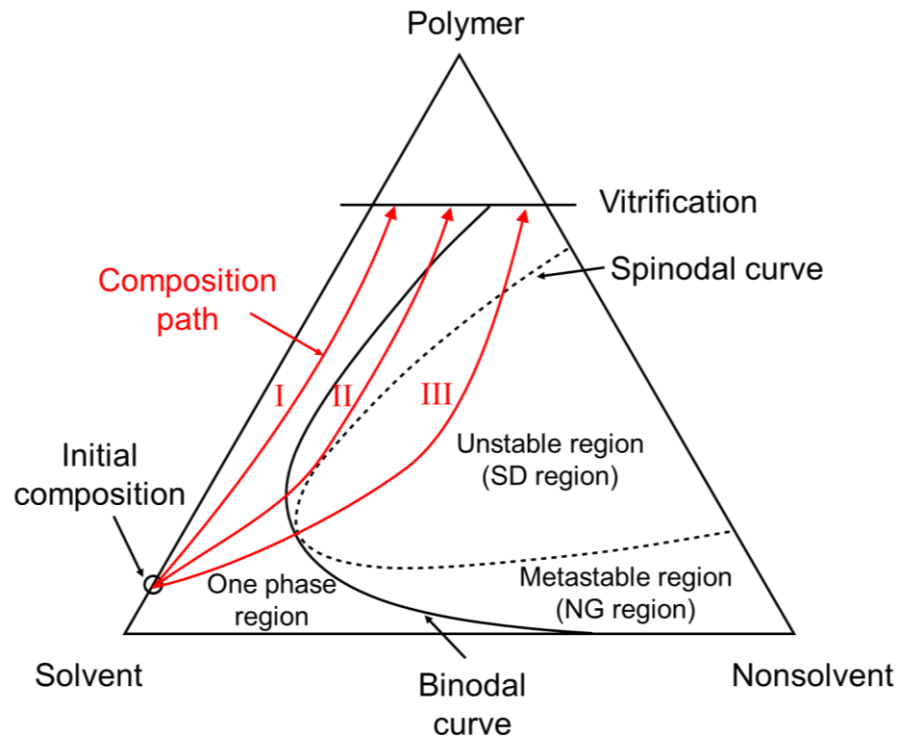
Figure 2.6 Typical ternary phase diagram for polymer-solvent-nonsolvent system. Reprinted from [41] with permission.

In path (I), the polymer solution does not enter a phase separated region, and solid fibers are formed. In path (II), the solution enters NG region which leads to isolated pores. In path (III), the solution enters SD region which leads to interconnected pores with irregular boundaries. For instance, electrospinning at low humidity or reduced content of volatile solvent should lead to the formation of solid fibers with no phase separation along path (I). That is indeed the case as solid fibers are formed in region (I) on Figure 2.5. Increasing the humidity or the content of volatile solvent should first promote NG along path (II), which is in agreement with the observed morphology of fibers in regions (II) and (III) on Figure 2.5. Moreover, electrospinning at very high humidity and high volatile

solvent content should lead to SD phase separation along path (III), in line with the morphology of fibers observed in region (IV) on Figure 2.5. The presented discussion is in line with the pore formation mechanism discussed in the literature [97, 101, 103, 106].

As discussed earlier in this chapter, the goal of this study is to identify processing parameters to maximize the porosity and axial connectivity of the pores in order to maximize the mass loading of functional material as well as enabling axial release after fiber fracture. In this regard, the porous structure formed by SD is the ideal, the pore formed by SD not only have high porosity, they are formed in an interconnected structure. Hence, the parameter in region IV on Figure 2.5 were selected for the rest of study. The morphology of the porous fiber fabricated using these parameters is shown in Figure 2.4b.

2.3. Conductive porous nanofibers

As discussed in Section 2.1.2, PAN will be used in this study to fabricate porous CNFs due to its good spinnability, low cost and high carbon yield. However, due to the high polarity of PAN chains, it does not dissolve in any volatile solvent, the lack of evaporative cooling makes phase separation difficult to be induced by humidity in the environment. Therefore, the phase separation method discussed in previous section cannot be easily applied to PAN to fabricate porous PAN fibers with high porosity[108, 110]. As a result, porous CNF will be fabricated through the method of selective removal of a sacrificial component at discussed in Section 2.1.2. In order to increase the mass loading of functional materials, hollow fiber with different shell structure was fabricated using coaxial electrospinning. The experimental work on the fabrication of porous CNF using

emulsion and coaxial electrospinning will be presented in this section. The processing parameter which affects the porosity and the mechanical properties of porous CNFs will be discussed in detail. Furthermore, a model based on finite element analysis will be developed to analyze the influence of the different pore structure on the mechanical properties of the porous CNFs.

2.3.1. Experimental method

Fabrication of porous CNFs:

Multiple polymer solution and mixtures were first made for the electrospinning. To this end, PAN(Mw~150,000), PMMA with high and low molecular weight (~350,000 g/mol and ~15,000 g/mol) and DMF were obtained from Sigma-Aldrich and used as received. High M_w PMMA was dissolved in DMF at 16 wt.%, this PMMA solution was to be used at a sacrificial core in the coaxial electrospinning. PAN was dissolved in DMF at 12 wt.% to be used to make hollow CNF with solid shell. PAN/PMMA emulsion with PAN/PMMA ratio of 1:1 and 1:2 was made by dissolving PAN and PMMA (15k) in DMF at 9.1 wt.%: 9.1 wt.% and 7.7 wt.%:15.4 wt.%, respectively. Due to different solubility parameters of PAN and PMMA, the mixture separates in two phases nearly spontaneously, one rich in PMMA and one rich in PAN. The blend solution was then stirred vigorously for 24 hr to form an stable emulsion with a continuous phase consisting of PAN solution and a dispersed phase of PMMA solution[120], as shown in Figure 2.7.
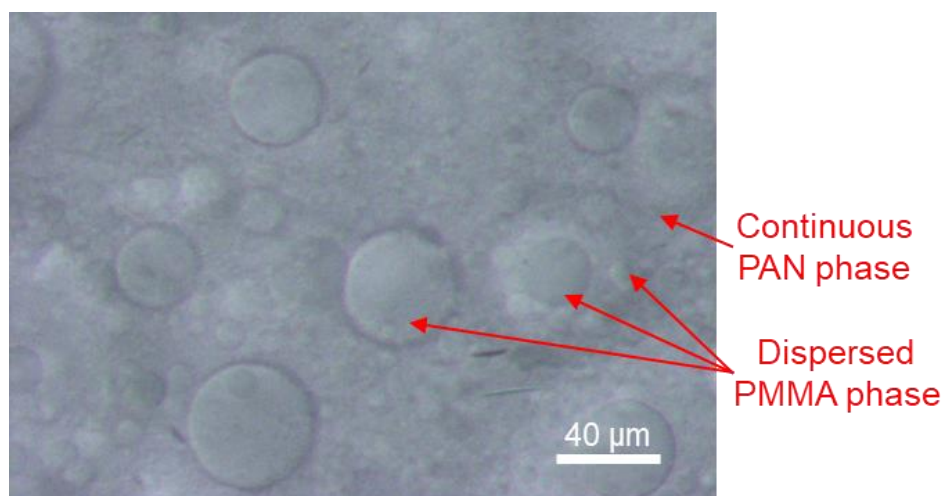
Figure 2.7 Optical image of the PAN/PMMA emulsion with PAN:PMMA = 1:2.

The polymer precursor fibers were then electrospun using a custom designed coaxial electrospinning setup, as shown in Figure 2.8. The coaxial needle was comprised of a 12 gauge outer needle and a 21 gauge inner needle. To fabricate the precursor fibers for solid shell CNF, the 16 wt.% PMMA(350 kDa)/DMF solution was supplied to the core needle, and the 12 wt.% PAN/DMF solution was supplied to the shell needle with two separate syringe pumps (Harvard Apparatus Model 11). The concentration of both solutions was selected to obtain smooth and beadless fibers. To fabricate the precursor fibers for porous shell CNFs, the PAN/PMMA emulsion with different PAN:PMMA ratio was supplied to the shell needle and the 16 wt.% PMMA/DMF solution was supplied to the core needle. The total concentration of the polymers was selected to have similar viscosity as the 12 wt.% PAN/DMF solution used for the solid shell CNF. The ratio between PMMA and PAN concentration in the emulsion was selected to obtain high porosity. The shell to core flow rate ratio of 1.4, 2.0 and 3.0 was used to achieve different shell thickness. In each case, the flow rate was adjusted to keep a steady Taylor cone size.

For flow rate ration of 1.4, the shell and core flow rate was 0.7 ml/hr and 0.5 ml/hr for the solid shell CNF, 0.56 ml/hr and 0.4 ml/hr for the PAN:PMMA=2:1 emulsion and 0.98 ml/hr and 0.7 ml/hr for PAN:PMMA = 1:1 emulsion. The electrospinning voltage and distance were set constant at 15 kV and 20 cm. Ribbons of fibers were collected on a grounded rotary drum at a take-up velocity of 3.9 m/s, corresponding to an angular velocity of 500 rpm. The temperature and relative humidity during electrospinning were controlled at 25±1°C and 40±2% respectively. After electrospinning, the precursor fibers were peeled off from the drum collector and stabilized in a convection oven at 270°C for 2 hr in an air atmosphere. The stabilized fibers were then thermally treated in nitrogen atmosphere at 1100°C for 1 hr in a tube furnace (MTI GSL-1700X) with a ramp rate of 5°C/min. Details of the stabilization and carbonization process were obtained from literature [93].
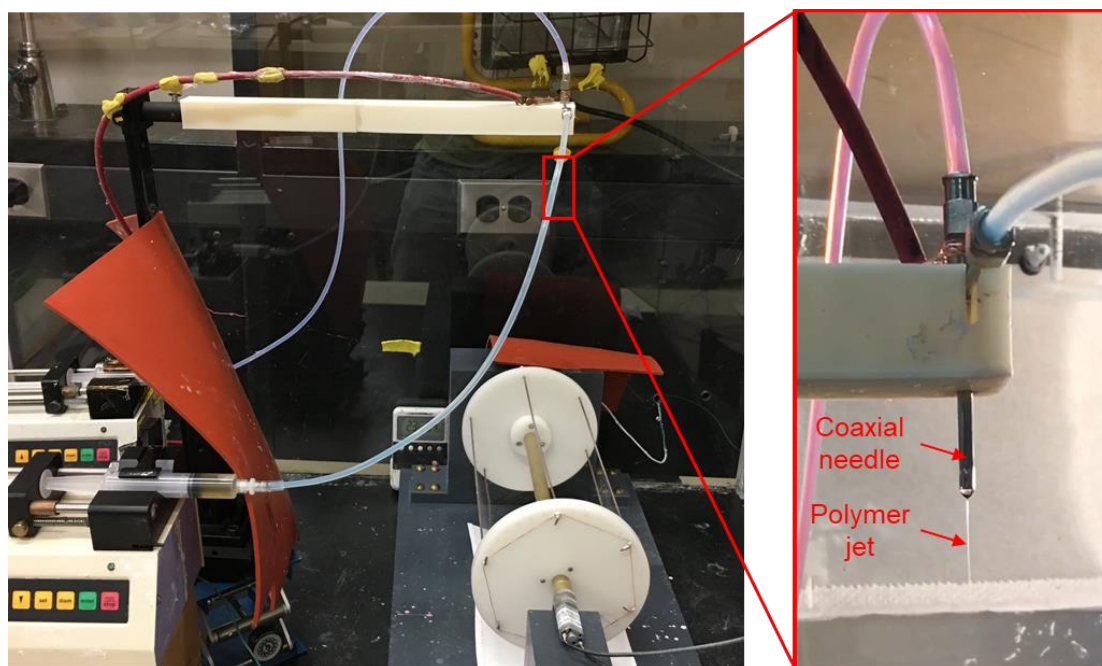
Figure 2.8 Coaxial electrospinning setup.

Material characterization:

The morphology of CNFs was analyzed by field-emission scanning electron microscope (FEI Quanta 600 FE-SEM). To image the cross section of the fibers, they were cut with a razor blade and mounted with the cross sections normal to the electron beam. The fiber diameter and shell thickness were measured from SEM images with ImageJ software. Raman spectra of CNFs were obtained by Horiba Jobin-Yvon LabRam Raman confocal microscope with a He-Ne laser (633nm). The pore structure of the fibers was studied by collecting N_2 adsorption isotherms at 77K with Quantachrome Autosorb iQ. Before the adsorption test, samples were degassed for 4 hrs at 250°C under vacuum. The specific surface area was calculated by Brunauer-Emmett-Teller (BET) theory. The pore size distribution was obtained by applying quenched solid density functional theory (QSDFT) assuming cylindrical pores. The total pore volume was obtained from total amount of N_2 adsorption at relative pressure close to 1.

Mechanical characterization of CNFs:

The mechanical properties of the CNF were obtained by single fiber tensile tests using an in-house designed MEMS device (fabricated by MEMSCAP Inc). Single CNF was placed on the MEMS device using a tungsten probe controlled by a micro-manipulator under an optical microscope. A Platinum block was deposited using Focused Ion Beam (FIB) (Tescan LYRA-3 Model GMH Focused Ion Beam Microscope) to grip the fiber. During the tensile test, the MEMS was actuated by a picomotor actuator (Newport Picomotor Actuator 8303), as shown in Figure 2.9. Optical images were captured using an

optical microscope during the test, as shown in Figure 2.10. The force and displacement were determined by analyzing the images using digital image correlation (DIC) software (VIC-2D). The resolution of the stress and strain measurements using this method are better than 4 MPa and 0.1% respectively [93]. The force applied to the CNFs in this method is calculated by multiplying the stiffness of the micromachined silicon compliant beams (*i.e.*, load cell) by the deflection of the load cell. The former is calculated based on Euler–Bernoulli beam theory by knowing the elastic modulus of silicon (a well-documented value) and the dimensions of the load cell, which is designed and controlled with high precision via micromachining techniques. Moreover, the deflection of the beam and the elongation of the CNF are both calculated by tracking the motion of the micropads on which the CNF ends and the load cell ends are anchored to. This is carried out via using DIC applied to the optical images taken from the loaded CNFs, with a resolution better than ~30 nm. More details on the accuracy and validity of MEMS device and single fiber test can be found in the literature [92, 137, 138]. After the test, the fiber fracture surface was observed by SEM and the cross-sectional area of the shell was measured on SEM images to determine the stress. For each type of sample, a minimum of 5 tests were performed and the average values and standard deviations were reported.
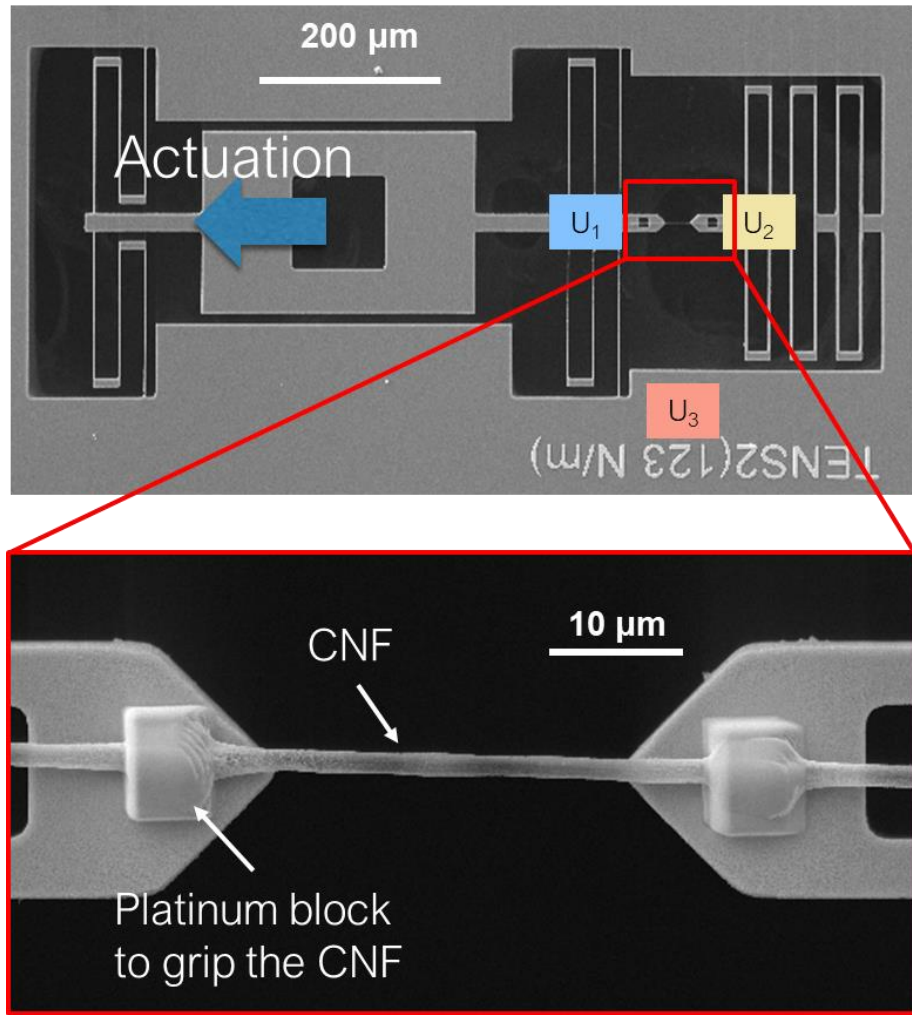
Figure 2.9 SEM images of MEMS device for the single fiber tensile test.
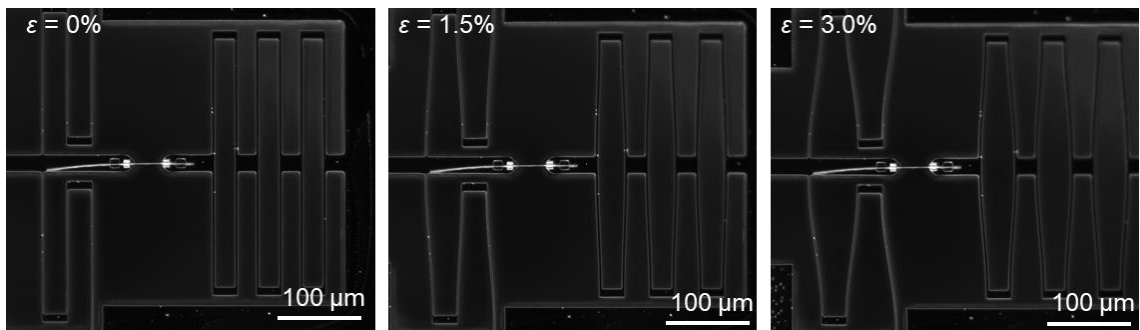
Figure 2.10 Optical images during the single fiber tensile test.

2.3.2. Results and discussion

Effect of electrospinning parameters on the morphology of porous CNFs:

The PAN/PMMA emulsion has an island in sea structure: The PAN/DMF phase has lower surface tension than the PMMA/DMF phase, as a result, PAN/DMF formed the continuous phase ("sea") and PMMA/DMF formed the dispersed phase ("island") [120, 128, 139]. During electrospinning, the island in sea structure emulsion is stretched and forms composite fibers consisting of PMMA phase embedded in a continuous PAN phase, as show in the schematic in Figure 2.11a. To study the structure of the composite fibers, emulsion electrospinning without the hollow core was studied first. Figure 2.11b,c shows the SEM images for the emulsion electrospun PAN/PMMA fiber before and after removing the PMMA phase by dipping the fibers in acetone for 10 s , since acetone is good solvent for PMMA and non-solvent for PAN, this solvent treatment preserves the PAN structure and removes the PMMA nanofibrils. Before removing the PMMA phase, PMMA nanofiber were embedded in the PAN matrix, as shown in Figure 2.11b. After removing the PMMA phase, pores are formed as shown in Figure 2.11c. It is to be noted the fact that PMMA can be removed by solvent proves that the pores are interconnected, and they can be accessed from the surface.
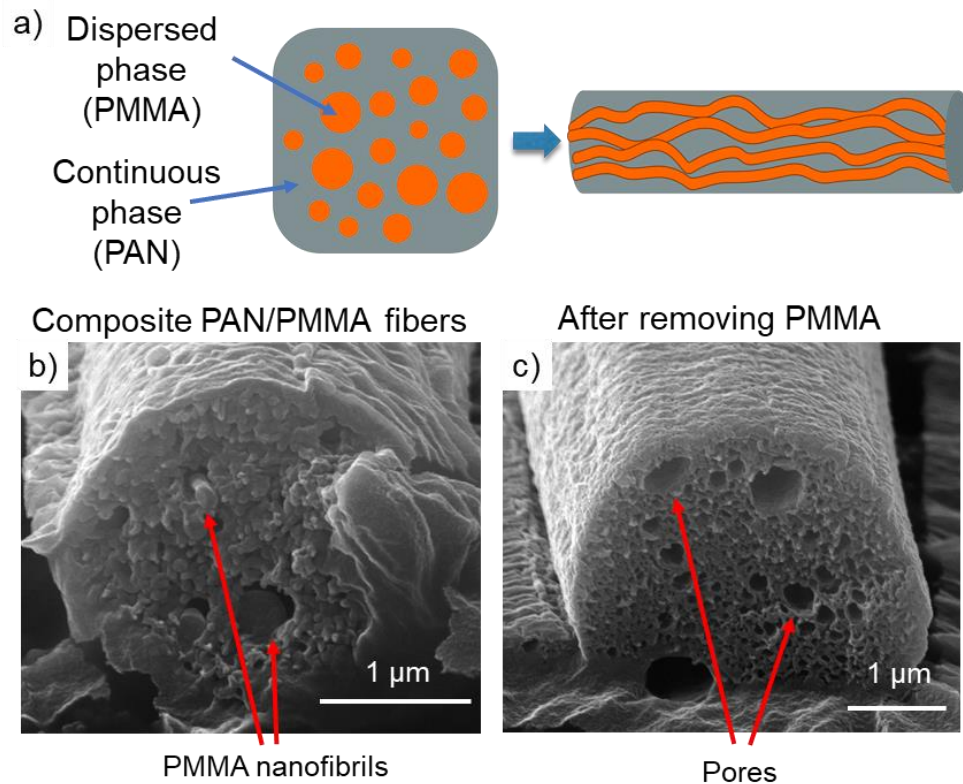
Figure 2.11 a) Schematic for emulsion electrospinning. SEM images of emulsion electrospun composite PAN/PMMA fiber b) before removing PMMA, c) after removing PMMA.

The composite PAN/PMMA fibers were further stabilized and carbonized to form porous CNFs. During the thermal treatment at 1100°C, PAN molecules undergo cyclization and form the carbon structure, PMMA in the both the shell and the core decomposes into gaseous phase and leave pores behind. As seen in Figure 2.12a, the PMMA has been remove by the thermal treatment and formed pores. Diameter of PAN/PMMA fibers at different stages are shown in Figure 2.12b.
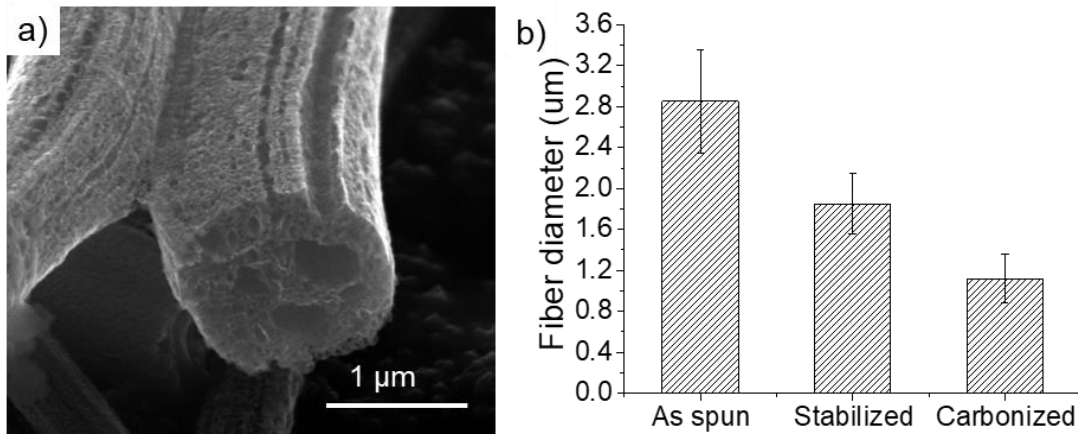
Figure 2.12 a) SEM images of porous CNF. b) Average fiber diameter for emulsion electrospun PAN/PMMA fibers at different stages.

Influence of shell/core flow ratio on the CNF structure:

To further increase the accessible volume for loading functional materials and the surface area for energy storage. A hollow core was introduced into the CNFs by coaxial electrospinning. Different shell/core solution flow ratio was studied. SEM images of porous hollow PAN nanofibers and CNFs were made at different flow ratio are shown in Figure 2.13. Average fiber diameter and shell thickness for the CNFs are shown in Figure 2.13g,h. The diameters and thicknesses were measured by SEM images with a minimum of 30 measurements.

As can be seen, changing the flow ratio has very small influence on the fiber diameter. However, the shell thickness increases significantly with increased flow ratio. This is because the fiber diameter was controlled by the viscosity of the shell solution, which stayed the same for different flow ratios. While the skin thickness has a direct dependence on the flow ratio due to the conservation of mass. This suggests that in order to maximize the available volume for loading functional material in the porous CNFs, the

flow ratio should be as low as possible to obtain a very thin shell with very large hollow core. However, in the experiments, flow ratio less than 1.4 resulted in unstable Taylor cone and polymer jet, therefore the minimum stable flow ratio 1.4 was selected for the rest of the study.
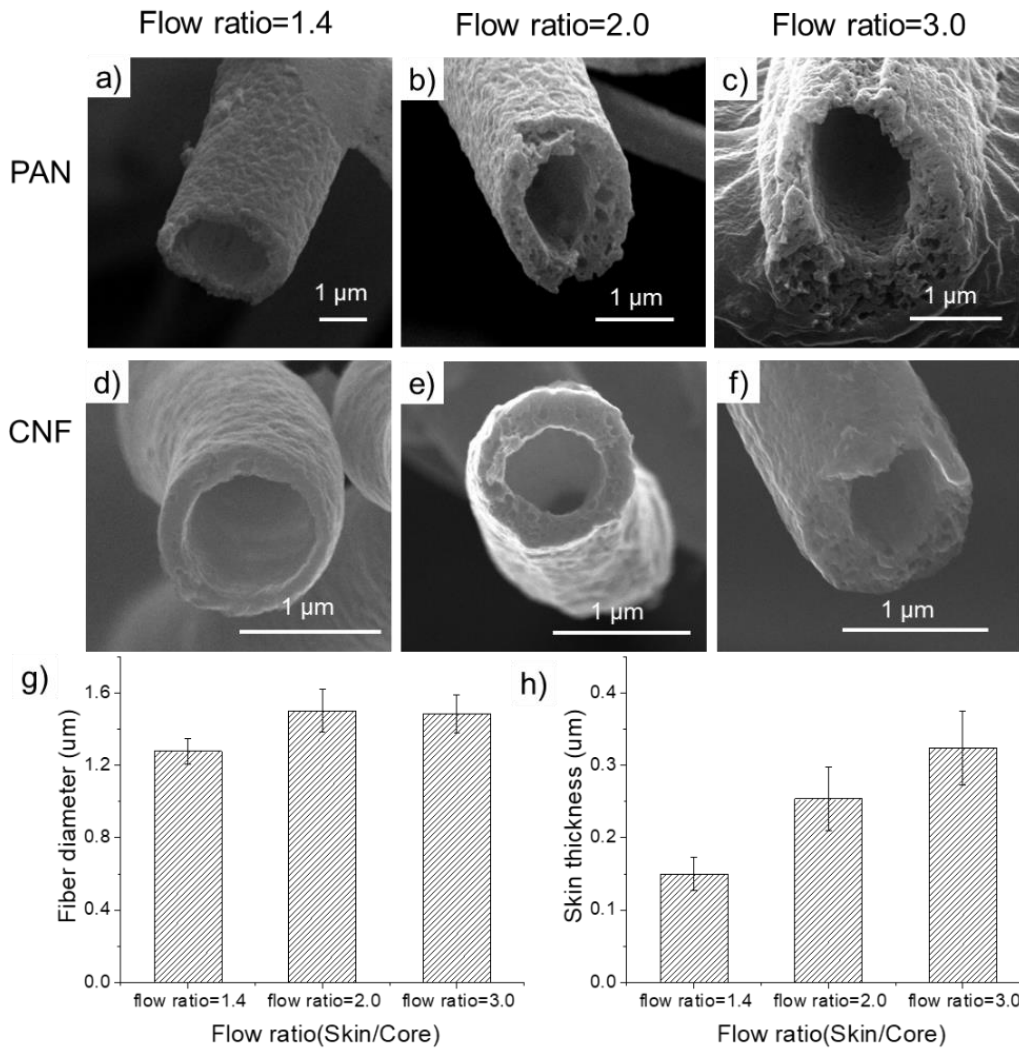
Figure 2.13 SEM images of porous PAN nanofibers made at flow ratio a) 1.4, b) 2.0 and c) 3.0. SEM images of porous CNF made at flow ratio a) 1.4, b) 2.0 and c) 3.0. g) Average porous CNF diameter made at different flow ratio. h) Average shell thickness for porous CNF made at different flow ratio.

Influence of PAN:PMMA ratio on the porous structure of porous CNFs:

PAN:PMMA ratio of 1:0 (pure PAN), 1:1 and 1:2 was used in the shell solution during the electrospinning to study its influence on the porous CNF structure. SEM images of the CNF fabricated under these conditions are shown in Figure 2.14. As can be seen, on the 1:0 sample, CNFs with solid shell were obtained, the cross-section is continuous with no observable voids (Figure 2.14b), whereas in 1:1 and 1:2 samples, CNFs with porous shell were obtained, highly porous structure was observed with a large number of pores spread across the cross-section on both conditions. (Figure 2.14d, f). The outer diameter of CNFs was measured on more than forty CNFs using SEM for each fabrication condition. The average and standard deviation of the outer diameter for CNFs with PAN:PMMA ratio of 1:0, 1:1 and 1:2 were 1.50 ± 0.23 μm , 1.72 ± 0.44 μm and 1.61 ± 0.29 μm, respectively. Similar method and sample size were used to measure the shell thickness. The average shell thickness for CNFs with PAN:PMMA ratio of 1:0, 1:1 and 1:2 were 0.23 ± 0.06 μm, 0.31 ± 0.06 μm and 0.24 ± 0.06 μm respectively.
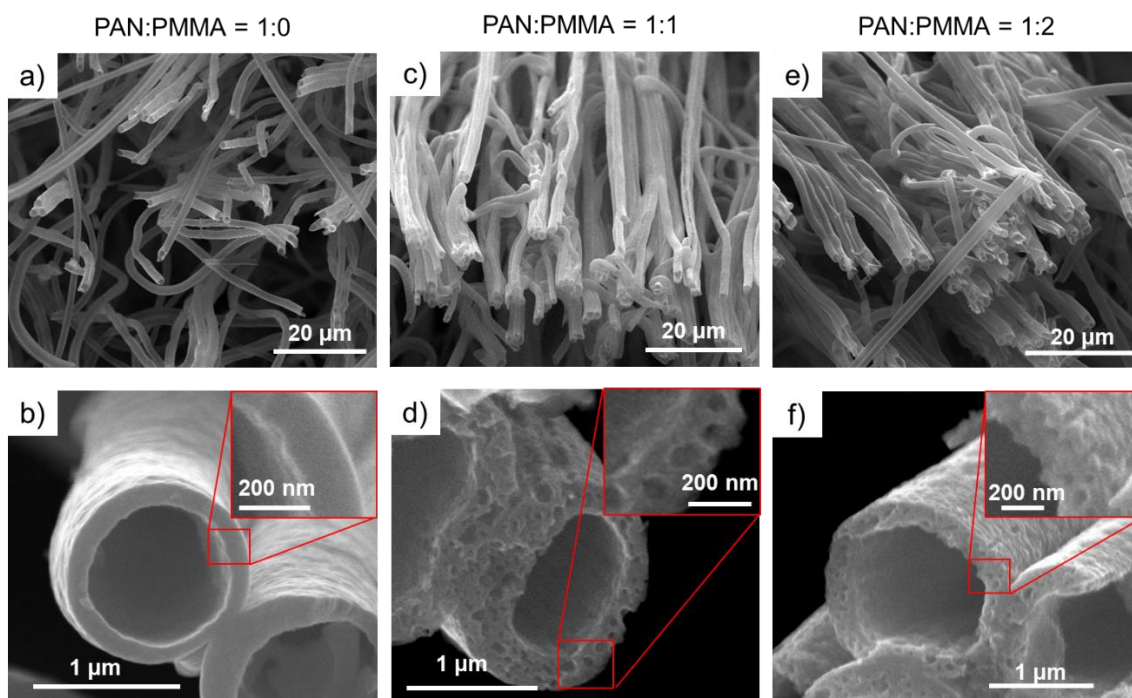
Figure 2.14 SEM images of porous CNFs fabricated with PAN:PMMA ratio of a), b) 1:0, c), d) 1:1 and e), f) 1:2. Reprinted from [49] with permission.

To analyze the influence of PAN:PMMA ratio on the porous structure, the samples were characterized by N_2 adsorption. The adsorption isotherm of CNFs fabricated at different PAN:PMMA ratios are presented in Figure 2.15a. The specific surface area (SSA) of the CNFs with PAN:PMMA of 1:0, 1:1 and 1:2 is 36.1 m^2/g, 53.0 m^2/g and 87.2 m^2/g, and the total pore volume is 0.070 cm^3/g, 0.246 cm^3/g and 0.243 cm^3/g respectively, as shown in

Table 2.1. The addition of PMMA in the shell resulted in an increase in SSA (1.5x for 1:1 and 2.4x for 1:2) and pore volume (3.5x for both 1:1 and 1:2). The porosity can be calculated using the total specific pore volume (*i.e.*, pore volume per unit mass, V_p) from adsorption and the density of PAN based carbon fiber (ρ = 1.7~1.9 g/cm^3)[140] as $P=V_p/(V_p+1/\rho)$. As a result, the porosity of CNF with PAN:PMMA of 1:1 and 1:2 was

45

calculated to be 11.2±0.6% , 30.7%±1.2% and 30.4±1.2%, respectively. Interestingly, increasing the PAN:PMMA ratio from 1:1 to 1:2 resulted in higher SSA without affecting the porosity.

Table 2.1. Porous structure properties of CNFs. Reprinted from [49] with permission.

Type of CNF	BET specific surface area (SSA) m^2/g	Specific pore volume (V_p) cm^3/g	Average pore diameter nm	Porosity(P)	Normalized porosity (P_n)
PAN:PMMA=1:0	36.1	0.070	7.8	11.2%	-
PAN:PMMA=1:1	53.0	0.246	18.6	30.7%	19.5%
PAN:PMMA=1:2	87.2	0.243	11.1	30.4%	19.2%
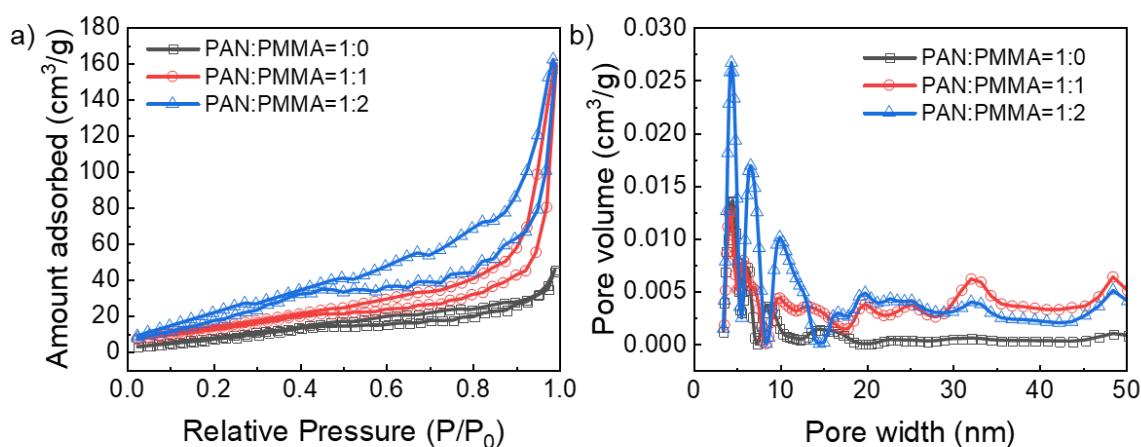
Figure 2.15 a) N_2 adsorption isotherm of solid and porous shell CNF, b) Pore size distribution of solid and porous shell CNF, calculated using QSDFT method. Reprinted from [49] with permission.

To better evaluate the changes in the porous structure as a function of the addition of PMMA, the pore size distribution is analyzed (Figure 2.15b). Adsorption at low relative pressure 0~0.2 is attributed to the filling of micropores during nitrogen adsorption (pore width smaller than ~3 nm)[141, 142]. In all samples, the low adsorption amount in this range

indicates that the micropores constitute a small portion of the porosity. These micropores are likely surface pores and roughness on the inner and outer surfaces of the shell. Adsorption at higher relative pressure 0.8~1 correspond to filling of mesopores (pores width between 3 nm to 50 nm)[141, 142]. The pore volume for small mesopores (3-10 nm) showed similar distribution on samples with PAN:PMMA ratio of 1:0 and 1:1 and slightly increased at ratio of 1:2. For larger mesopores (10-50nm), the pore volume for samples with PMMA (1:1 and 1:2) are significantly higher than the 1:0 sample, indicating large amount of mesopores was generated due to the decomposition of PMMA. For pores with the size of 30-50 nm, the pore volume for 1:1 is much higher than 1:2, indicating that the increase in the PAN:PMMA ratio lead to smaller average pore size, which is in agreement with the decrease in average pore size shown in

Table 2.1. This is also in line with the SEM images, as shown in Figure 2.14d and f. This could also explain the increase in SSA when PAN:PMMA ratio increased from 1:1 to 1:2 whereas the porosity stayed the same.

Despite differences in the morphology of the CNFs, the Raman spectra for different CNFs, shown in Figure 2.16, suggests that all types of CNFs have similar partially graphitic structures. The two peaks appeared at ~1336 cm^{-1} and ~1580 cm^{-1} corresponds to defects (D peak) and graphitic structures (G peak) of carbon materials. The intensity ratio of the D peak to G peak indicates the defect density and quality of graphitic domain, and it is related to the graphitic domain size and defect density within the graphitic domains [143-145]. The I_D/I_G ratio for all three cases are very close, 1.16, 1,16 and 1.21 for

PAN:PMMA of 1:0, 1:1 and 1:2 respectively. The similar I_D/I_G ratio suggests that the existence of PMMA in the shell did not affect the molecular structure of carbonized PAN.
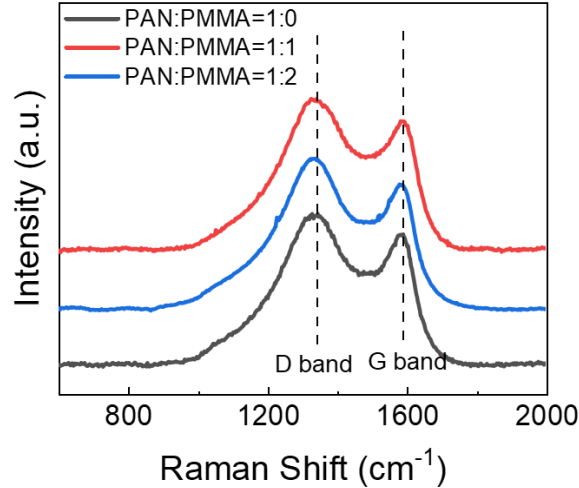
Figure 2.16 Raman Spectra of CNFs fabricated with different PAN:PMMA ratio. Reprinted from [49] with permission.

Mechanical property of porous CNFs:

To study the influence of the pores on the mechanical property of the CNFs. PAN:PMMA of 1:0 and 1:2 were selected and have been designated as solid shell and porous shell CNFs, respectively. Representative apparent stress-strain curves of CNFs with solid and porous shell CNFs are shown in Figure 2.17a. The apparent stress was calculated by $S_{apparent} = F / A_{shell}$ where F is the measured force applied to the fiber by the microdevices, and A_{shell} is the total cross-sectional shell area (as shown in Figure 2.18c), which is measured from the SEM images of the fractured surfaces. In both cases, CNF behaved in a linear elastic fashion until fracture and experienced brittle fracture. The mechanical properties are summarized in **Table 2.2** and Figure 2.17b. SEM images of the fracture surface are shown in Figure 2.18.

48
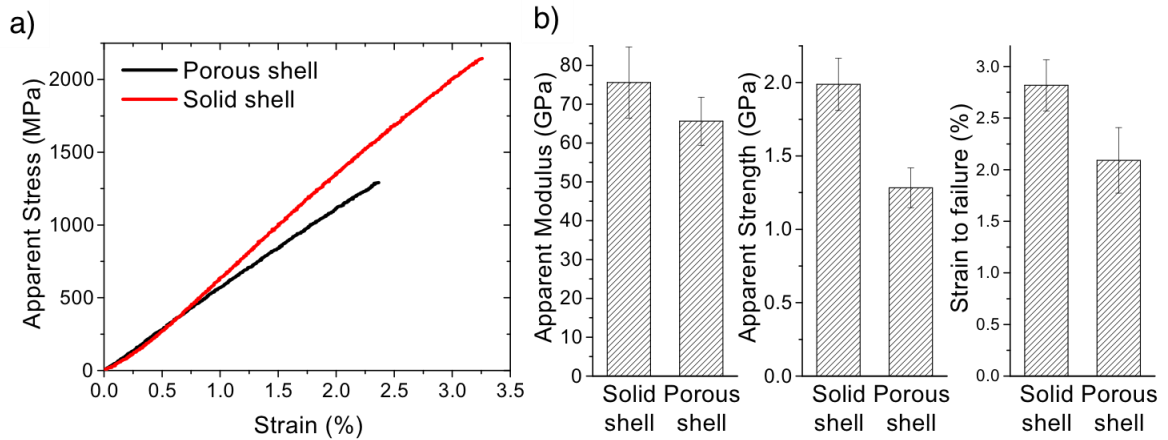
Figure 2.17 a) Representative apparent stress-strain curve of solid and porous shell CNFs tensile tests, b) average apparent modulus, apparent strength and stain to failure for solid and porous shell CNF. Reprinted from [49] with permission.

The average apparent modulus, apparent strength and strain to failure for the solid shell CNF was 75.6±9.2GPa, 1.99±0.18GPa and 2.8±0.2%. The average apparent modulus, strength and strain to failure for the porous shell CNF was 65.0±6.2GPa, 1.28±0.14GPa and 2.1±0.3%. Surprisingly, the mechanical properties of the porous shell CNF were not significantly lower than for the solid shell CNF: the apparent modulus, apparent strength and the strain to failure of the porous shell CNF reduced by ~14%, 36% and 26%, respectively.

Table 2.2. Mechanical properties of hollow CNF. Reprinted from [49] with permission.

	Apparent Modulus (GPa)	True Modulus (GPa)	Apparent Modulus (GPa)	True strength (GPa)	Strain to failure
Solid shell CNF	75.6±9.2	-	1.99±0.18	-	2.8±0.2%
Porous shell CNF	65.0±6.2	80.5±7.2	1.28±0.14	1.59±0.17	2.1±0.3 %
Reduction	13.9±2.1%	-6.5±1.0%	35.5±4.9%	20.1±2.8%	25.8±4.5%

As discussed in previous section, the similar I_D/I_G ratio in Raman spectra indicates similar graphitic domain quality for two cases. Thus, the loss of strength and modulus should be attributed to the differences in stress distribution between porous and solid shell CNFs. The pores can cause stress concentrations and also reduce the effective load bearing area which can in principle lower strength. The former will lead to first local and then propagating failure by generating nonuniform stress fields, while the strength loss in the latter is proportional to the porosity of the fibers.
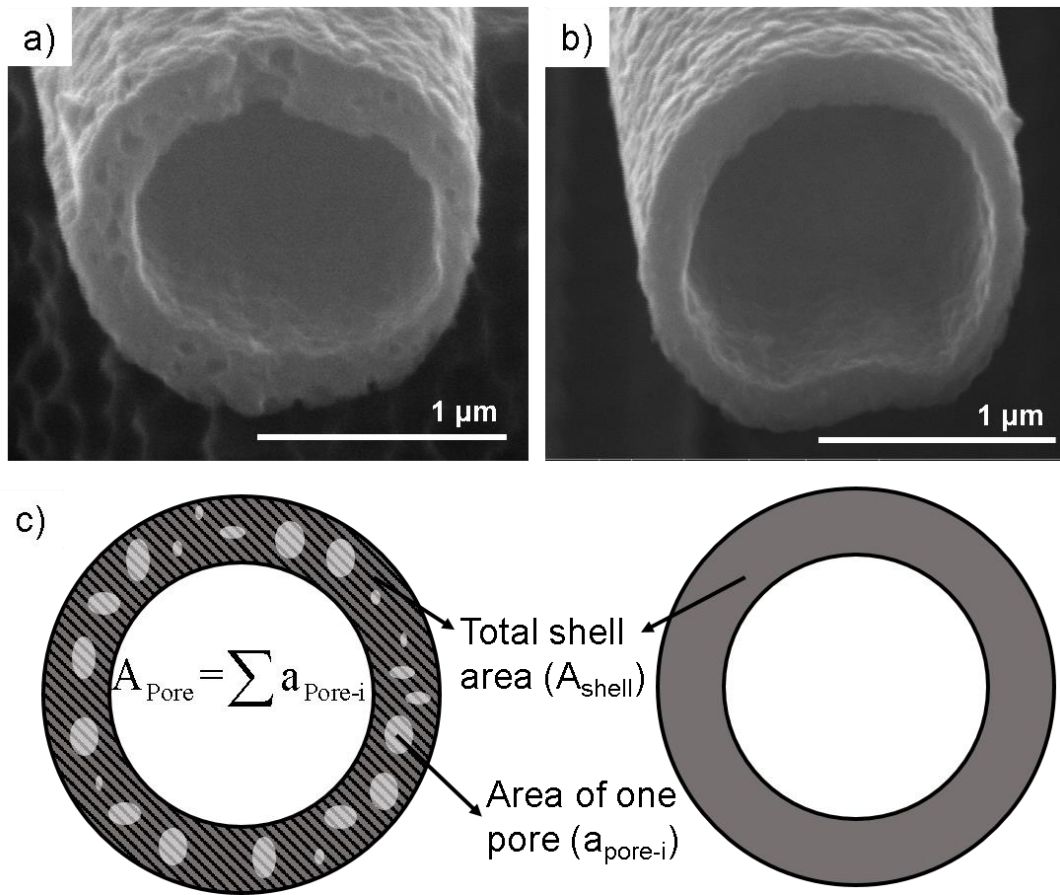
Figure 2.18. SEM images of failure surface of a) porous shell CNF and b) solid shell CNF c) schematic of hollow CNF. The total shell area in the porous CNFs is hatched and includes the area of the pores. Reprinted from [49] with permission.

50

On the other hand, the magnitude of stress concentration is strongly dependent on the curvature of pore cap along the loading direction. For instance, consider an elongated ellipsoidal pore with major axis of a and a minor axis of r $(a>r)$, and another spherical pore with radius of r. If the loading direction is along the major axis of the ellipsoidal pore, the ellipsoidal pore has lower curvature (r/a^2) than the spherical pore ($1/r$), resulting in a lower stress concentration and consequently lower loss in strength [146].

Therefore, to relate strength loss to porosity in CNFs, the shape of the pores was examined by SEM. To this end, internal pores were exposed by making longitudinal cuts in porous shell CNFs via FIB. As shown in Figure 2.19 b & c, the pores have high aspect ratio and are elongated along the fiber direction. This pore shape is due to the stretching of the dispersed PMMA in the emulsion during electrospinning, consistent with other findings in literature[120]. The formation of elongated pores may explain why the mechanical properties of porous shell CNT did not reduce significantly comparing the solid shell CNF.

In addition to stress concentration, the reduction in load bearing portions of the cross-section area (porosity) can also lower the strength. As shown previously, the CNF with solid shell has no observable pores inside the shell, therefore the porosity is mainly due to surface pores. To relate the mechanical properties to porosity in porous shell CNFs, the porosity in porous shell CNFs must be adjusted with respect to the porosity of solid shell CNFs. This adjustment assumes that the CNF with solid shell and porous shell have similar surface pore volume with similar contribution to the mechanical properties. Thus, a normalized porosity (P_n) for the porous shell CNF can be calculated as the porosity

difference between the porous and solid shell CNF. The normalized porosity (P_n) of the porous shell CNF is 19.2±1.3% (calculated by subtracting the porosity of solid shells from that of porous shell CNFs).
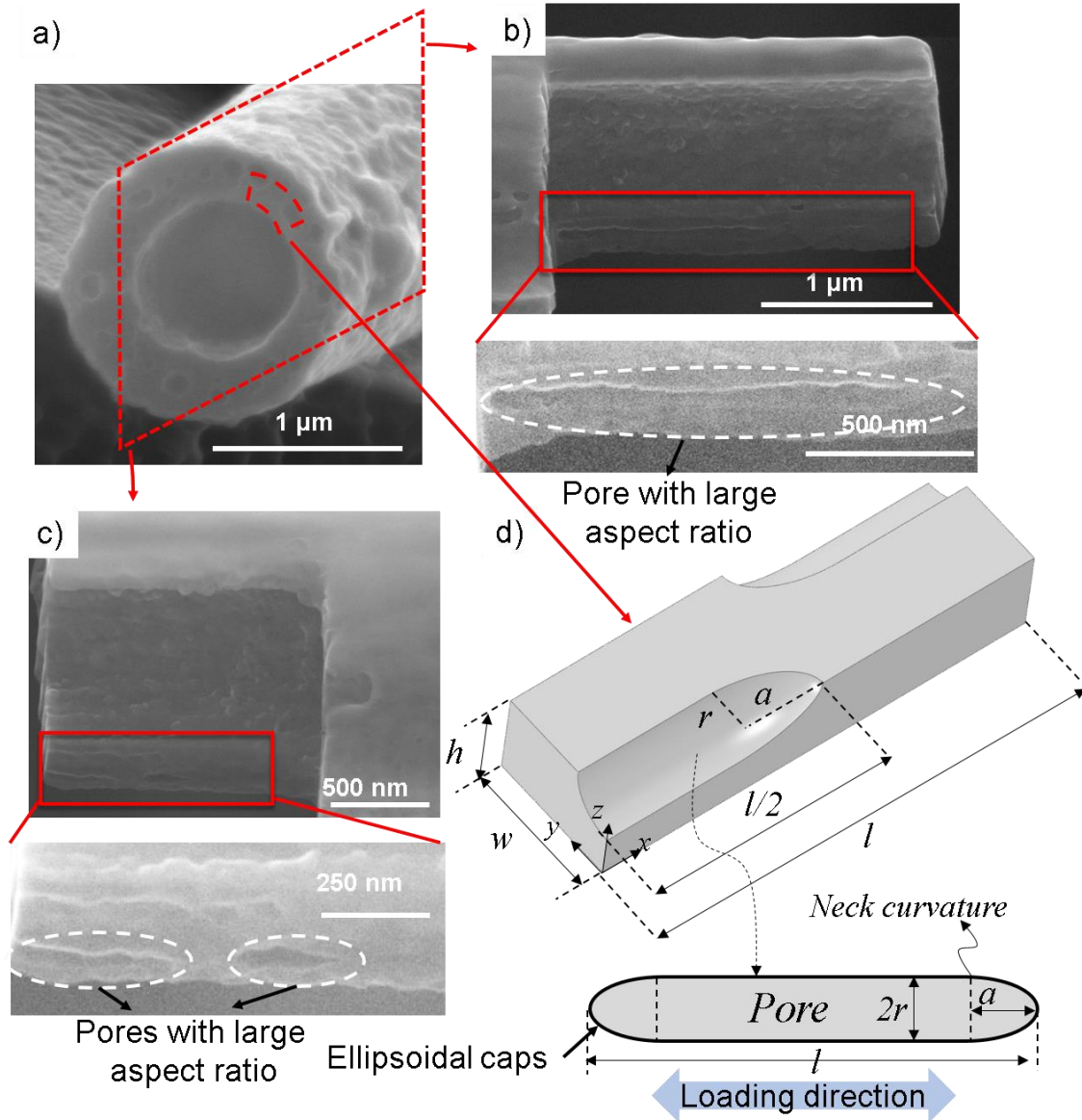
Figure 2.19 a) SEM image of porous shell CNF, fracture surface after mechanical test. b), c) Longitudinal cross-section of porous shell CNF obtained through FIB etching, d) Schematic for the shape of the pore and the RVE used in the finite element analysis. Reprinted from [49] with permission.

Considering the measured apparent mechanical properties, the loss in apparent modulus, 13.9±2.1%, is comparable to the normalized porosity especially when the uncertainties in measurements are taken into account, whereas the reduction in apparent strength of 35.5±4.9% is much higher than the normalized porosity. Thus, the loss in apparent modulus is mainly caused by the reduction in the load bearing area of the CNFs when pores are introduced. In other words, if pores are fully aligned with the fiber axis and have very high aspect ratio, the apparent modulus can be predicted by the rule of mixtures, and the reduction in modulus will be equal to the reduction in area. On the other hand, the reduction in apparent strength outweighs the reduction in load bearing area of CNFs by a large margin (loss in strength is ~36%), and therefore requires the consideration of stress concentrations.

To separate the effect of area loss and stress concentration on mechanical properties, the true modulus and true strength for the porous shell CNF can be calculated by excluding the pore area from the total cross-sectional area when calculating stress, i.e. $S_{true} = F / \left(A_{shell} - A_{pore} \right)$. Assuming the adjusted porosity (P_n) is only a result of the mesoporous structure, the area porosity is equal to the normalized porosity, the true modulus and strength will be equal to their corresponding apparent values divided by 1-P_n. Thus, the true modulus and true strength of porous CNFs are 80.5±7.2 GPa and 1.59±0.17 GPa. Compared to solid shell CNF, the true strength decreased by 20.1% and the strain to failure decreased by 25.8%. The losses in true strength and strain to failure

53

are very close, within the uncertainty. As such, the loss in strain to failure is also mainly attributed to stress concentration as discussed earlier in this section.

Prediction of strength reduction in porous CNFs via continuous mechanics model:

Although carbon fibers (CFs) have achieved great success in structural applications, the failure mechanics of CFs is still not well understood. Even less is known about the failure mechanics of CNFs. The failure of CFs initiates mostly at two types of defects: (1) misoriented turbostratic (i.e. crystalline) regions surrounded by oriented turbostratic regions, similar to a kink in a crystal, and (2) the interface between turbostratic and amorphous regions [147]. Misoriented crystalline regions are essentially shear stress concentrators. Penev et al [148] used molecular dynamics to study these defects and found that both the tensile strength and the strain to failure decreased with increasing angle of misorientation. A misorientation angle of 12 degrees can lower the strength by almost 50%. Continuum models have also been used to study the mechanics of carbonized structures with misoriented regions. A seminal study by Reynolds and Sharp [149] simply resolved the components of the applied stress to obtain the shearing stress acting on the misoriented plane. The analysis is independent of the size of the defect, only targeting orientation. Tagawa and Miyata [150] extended this method to include Weibull strength distributions that account for the volume (i.e. size) of the fiber, but not the defect size. Naraghi and Chawla [147] developed an experimentally verified model for the failure of the crystalline/amorphous interface by adapting failure models for short-fiber composites. Each CNF is considered to be a composite material, composed of amorphous carbon

(matrix), reinforced with turbostratic domains. According to the model, the strength of a portion of composite depends on the following variables: the angle between the direction of loading and the axis of the reinforcement, the strength of the matrix (amorphous carbon), the axial strength of the reinforcement (in plane strength of turbostratic domains), and the strength of the composite parallel and perpendicular to reinforcement, the shear strength of the interface between the reinforcement and the matrix, the volume fraction of reinforcements, the length and diameter of the reinforcements, and the critical length of the reinforcements. It was determined that the likely cause of the failure of CNFs is the detachment of the graphitic particles from amorphous carbon and pull-out.

The presence of pores can trigger additional failure mechanisms, further complicating strength predictions. To the best knowledge of the author, the failure mechanics of porous CNFs is not studied in the scientific literature. However, given the fact that the failure of CNFs is brittle, prior studies on failure of porous brittle materials, such as porous ceramics, can be elucidating, as discussed below.

Several models have been reported in the literature to study the relationship of porosity and strength of porous materials [151]. Balshin [152] suggested a model to capture the relationship of the tensile strength (often apparent strength) of porous metal and ceramics: $\sigma = \sigma_0 (1-P)^b$ where σ_0 is the strength with no porosity, P is the porosity and b is an empirical constant. Ryshkewitch [153] proposed another relationship between strength of porous material $\sigma = \sigma_0 e^{-kP}$ where k is an empirical constant. Another relationship between porosity and strength was developed by Hasselman [154]: $\sigma = \sigma_0 - cP$, where c is

empirical constant. A common theme in all these models is that the apparent strength of porous materials drops more than linearly with porosity, i.e., the true strength of the material drops when porosity is introduced into the material. An explanation for this drop is the development of gradient of stress fields in the material, which together with the requirement to satisfy overall equilibrium with the applied load, results in locally higher than average stress fields, promoting failure. Another common feature in all the aforementioned models is that they are empirical, requiring experimental calibration and validation, to identify the scope of applicability.

Less empirical models have also been developed. An example of that is the simple relationship suggested by Haynes [155] which relates tensile strength of brittle material to porosity: $\sigma = \sigma_0 (1-P)/K$. In this model, the stress concentration factor for spherical pores is determined by elastic theory. A non-spherical pore shape was not considered. The effect of porosity and the development of stress gradients in the material which can promote failure has also been developed by considering the details of the microstructure of hierarchical structures [156]. However, these models are mainly applicable to highly porous foams in which the structure can be simplified as a combination of simpler structural components such as beams and columns.

To address the limitations in understanding the effect of pores on mechanics of CNFs, we studied the mechanics of the building blocks of porous CNFs via Finite Element Analysis (FEA). The material properties used in the model was obtained from studies on PAN based carbon fiber [157]. To this end, a representative volume element (RVE) of the porous fiber was constructed, Figure 2.19d. The pores were modeled as cylinders with

semi-ellipsoidal caps (ellipsoid of revolution). The pore shape was defined by three parameters: length (l), minor axis of the ellipsoidal cap (r) and major axis of ellipsoidal cap (a). The RVE contains two identical pores with each one being one-eighth of a complete pore. The inclusion of two pores with finite length was guided by experimental observation of discontinuous pores. Moreover, the consideration of two pores allows us to take into account the effects each pore can have on the stress fields around the other. Based on SEM images of porous shell CNF, the ratio of between the major and minor axis, a/r, was chosen to be 1-5, and the aspect ratio of the pores (l/r) was chosen to be 5-40. In this RVE, the porosity is defined as $P \sim \dfrac{pr^2}{4hw}$, note this is the area porosity, which is equal to the adjusted volumetric porosity stated earlier in section 3.3.

In the FEA model (Figure 2.19d), symmetric boundary conditions were applied to planes at $x=0$, $y=w$, $z=h$. A planar constraint was applied to $y=0$, i.e. the flat plane remains planer and parallel to the initial undeformed plane after the deformation. A displacement boundary condition was applied at $x=l$, where the displacement $u=l*1\%$ (equivalent to a 1% strain). The resultant force F_d and the maximum principal stress σ_{max} was obtained from the output of the FEA analysis. Due to the existence of the pore, the stress field is nonuniform. In this model, the apparent stress is equal to the resultant force divided by the total cross section area, $\sigma_{apparent} = F_d/(hw)$, and the true stress is equal to the ratio of the resultant force over the net cross section area of the fiber excluding the area of the pores, $\sigma_{true} = F_d / \left(hw - \pi r^2/4 \right)$. Thus, the following relationship can be obtained between apparent and true stress: $\sigma_{true} = \sigma_{apparent}/(1-P)$. The apparent and true stress concentration

factors are then defined as $K_{apparent} = \dfrac{\sigma_{max}}{\sigma_{apparent}}$ and $K_{true} = \dfrac{\sigma_{max}}{\sigma_{true}}$. The relationship between

two stress concentration factors is $K_{true} = (1-P)K_{apparent}$. It is also to be noted that since

the material is linear elastic, both the maximum true stress and apparent stress scale

linearly with strain, and as such, their ratio is independent of the applied strain. Therefore,

the values of $K_{apparent}$ and K_{true} can be calculated regardless of the value of the applied

strain and strength of the CNF.

As a result of the applied displacement, the resultant force F_d and the maximum

principal stress σ_{max} was obtained from the output of the FEA analysis. It is to be noted

that due to the existence of the pore, F_d is a result of a nonuniform stress field. In this

model, the apparent stress is equal to the resultant force divided by the total cross section

area, $\sigma_{apparent} = F_d/(hw)$, and the true stress is equal to the ratio of the resultant force over

the net cross section area of the fiber excluding the area of the pores,

$\sigma_{true} = F_d/(hw - \pi r^2/4)$. A relationship between apparent and true stress can be obtained:

$\sigma_{true} = \sigma_{apparent}/(1-P)$. The apparent and true stress concentration factors are then defined

as $K_{apparent} = \dfrac{\sigma_{max}}{\sigma_{apparent}}$ and $K_{true} = \dfrac{\sigma_{max}}{\sigma_{true}}$. The relationship between two stress

concentration factors is $K_{true} = (1-P)K_{apparent}$.

Since the CNFs experienced brittle fracture, the maximum principal stress was

chosen as the failure criteria. Hence, the relative strength reduction of the porous shell

CNF can be calculated as $\dfrac{\Delta\sigma}{\sigma_0} = \dfrac{K-1}{K}$, where $\Delta\sigma$ is the strength loss and σ_0 is the strength of a fiber with no pores. When $K_{apparent}$ is used, the strength reduction is due to the combination of both area loss and stress concentration, shown as black line in the results, whereas when K_{true} is used, the strength reduction is only a result of stress concentration effect, shown as blue line in the results.

The real pore geometry in the porous CNFs is more complex than the model. Hence, the reliability of the model needs to be examined. In the model, with a porosity of 20%, $a/r=3$ and $l/r=20$, $K_{apparent}$ is 1.89 and the strength reduction is 47.1%. This result is relatively close to the 35.5±4.9% strength reduction with a porosity of 19.2±1.3% in the experimental results (gray box in Figure 2.20b,c). Therefore, the model is fairly accurate and can give good qualitative prediction for the strength of the porous CNF.
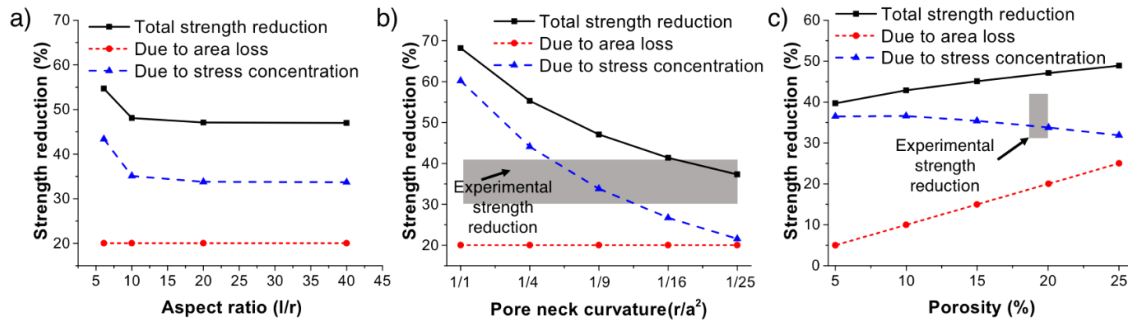
Figure 2.20 Influence of a) pore aspect ratio (l/r), b) pore neck curvature (r/a^2) and c) porosity on strength of porous shell CNF. Reprinted from [49] with permission.

With the verified model, we conducted a few simple parametric studies on the influence of pore geometry on the strength of the porous CNF. The influence of aspect ratio on the strength was first studied by changing l, with $r=50\,nm$, $a=150\,nm$ and $P=20\%$. The result is shown in Figure 2.20a. As shown in the result, the aspect ratio only affects

59

the strength when the aspect ratio is smaller than 10 and it has very small influence on the strength. In the following study, an aspect ratio of 20 was used for all cases. In order to study the influence of pore neck curvature (r/a^2) (curvature along the loading direction), r was kept constant at $r=50\ nm$ and a was changed to from 50 nm to 250 nm, $P=20\%$ was used. The results are shown in Figure 2.20b. There seems to be a strong dependence of strength on the pore neck curvature (r/a^2). With lower curvature, the stress concentration reduces significantly which leads to lower strength reduction. Furthermore, the influence of porosity on strength was also studied, $r=50\ nm$ and $a=150\ nm$ was used in this case, w was changed from 75 nm to 400 nm to have a porosity of 5% to 25%. The results are shown in Figure 2.20c. Thus the total porosity has very small influence on the stress concentration (blue line) and loss in strength. This insignificant reduction is mainly caused by a reduction in load bearing area. In Figure 2.20b & c, we have also presented the experimental results which clearly shows the reliability of the model. The results presented here can be used to design porous CNFs for multifunctional applications in which load bearing is one of the main functions.

2.4. Conclusion

In this Chapter, processing-morphology relationships of non-conductive PMMA porous fibers and conductive porous CNFs that were fabricated through phase separation and selective removal of sacrificial component, respectively, was established. The microstructure of porous PMMA fibers fabricated with different solvent volatility and relative humidity suggest a clear NG to SD transition by controlling relative humidity.

Near optimized parameters to fabricate porous PMMA fibers with high porosity and interconnected pores for loading functional material was identified to be DMF:DCM=1:4 at RH=90%.

Process parameters to fabricate porous CNFs were also investigated. The microstructural characterization showed a well-developed porous structure in the porous CNF. The ideal porous CNFs for loading functional material with high porosity and SSA is identified as using shell to core flow ratio of 1.4 and PAN:PMMA ratio of 1:1 and 1:2. The mechanical properties of the CNFs with porous and solid shell were characterized by single fiber MEMS test. The modulus, strength, and strain to failure of the solid shell CNF and porous shell CNF was 75.6±9.2GPa and 65.0±6.2GPa, 1.99±0.18GPa and 1.28±0.14GPa and 2.8±0.2% and 2.1±0.3% respectively. The modulus, strength, and the strain to failure decreased by 13.9±2.1%, 35.5±4.9% and 25.8%±4.5% when pores were introduced in CNFs. The loss in true mechanical properties, such as true strength and modulus, was mainly attributed to stress concentrations around pores. Continuum mechanics models of the porous shell CNF were built to study the influence of the pore geometry on the strength of porous CNF. The model predicts a 40%~70% strength reduction at 20% porosity, comparable to the experimentally measured loss in properties. Porosity and pore aspect ratio have limited influence on strength. Pore curvature along the loading direction was identified to have the most significant influence on the strength. It is important to note that since the intrinsic material properties was not affected by the pore generating process, a better designed pore geometry can be developed in the future to mitigate stress concentration and achieve even less strength loss.

3. ENCAPSULATION AND PASSIVE RELEASE OF FUNCTIONAL MATERIALS FROM NON-CONDUCTIVE POROUS NANOFIBERS[*]

As discussed in Section 1.3, the proposed porous fiber platform for encapsulation and release of functional material have several advantages comparing to existing methods including more freedom in material selection and flexible release mechanisms. The non-conductive porous fibers demonstrated in Section 2.2 are ideal candidate to encapsulate high loading of functional materials for passive release due to their high porosity and interconnected porous structure. In this chapter, the encapsulation and release of functional material is studied using the porous PMMA fibers. First, the method to load the porous PMMA fibers with functional materials is explored to achieve high mass loading. Next, the method to apply a polymer coating on the porous fibers to encapsulate the functional materials is presented. Moreover, the passive release of the functional material with different release mechanisms is studied.

3.1. Experimental method

To demonstrate the feasibility of the sequential process, benzalkonium chloride (BAC), an antibacterial salt, was selected as the functional material. BAC has been widely used as antibacterial agent in commercial product[158, 159]. Due to its good solubility in water

---

and ethanol, BAC can be carried into the porous fiber through by a carrier solvent to effectively load the porous PMMA fibers with BAC. The porous fibers containing BAC were spray coated with PMMA to encapsulate the material. The details of these processes will be presented in this section.

3.1.1. Loading porous PMMA nanofibers with functional materials

To load porous PMMA fibers with BAC, BAC (Sigma-Aldrich) was first dissolved at 68 wt.% in ethanol (Koptec) as the sacrificial solvent. The obtained BAC solution was doped with Rhodamine B (Sigma-Aldrich) for easier detection with fluorescence microscope. Porous PMMA fibers were attached to the frame and then soaked in BAC solution for 5 min. To expel trapped air in the fiber, the fibers were transferred into a low pressure chamber at pressure of -0.9 bar (relative to ambient conditions) for 5 min, pressure was then slowly released, and the fibers were taken out of the BAC solution and dried at 35 °C for 30 mins to remove the solvent before imaging or further treatment.

3.1.2. Contact angle measurement

The contact angle between the BAC/ethanol solution and PMMA film was measured using a self-assembled setup. The 10wt% PMMA solution in DMF:DCM (1:4) was casted on a glass slide and dried at 35 °C for 2 hours to form a PMMA film with a smooth surface. Before contact angle measurements, the obtained PMMA film was cleaned with isopropyl alcohol. Then, a 5 µL of the BAC/ethanol solution was slowly placed on the PMMA film using an Eppendorf Research pipette. An image of the droplet was captured with camera (Nikon D5100) and analysed using ImageJ with drop analysis plugin to measure the contact angle.

3.1.3. Spray coating on PMMA nanofiber

PMMA (M_w ~350 kDa) (Sigma-Aldrich) was dissolved at 0.1 wt.% in DMF (Sigma-Aldrich). The solution was sprayed onto the fibers (on the frame) for 8 minutes by using a spray nozzle (Burgener Mira Mist) at a distance of 20 cm, as shown in Figure 3.1. PMMA solution was supplied to the nozzle with syringe pump at a rate of 0.3 ml/min. Compressed air was used as the air supply for the spray nozzle, and the air pressure was set to 50 psi using a regulator. The PMMA solution was doped with fluorescein (Sigma-Aldrich), so that the coating uniformity can be examined via confocal fluorescent microscopy. Spray coating was carried out from four directions, each direction for 2 minutes, to achieve uniform coating.

To estimate the coating thickness, the average skin thickness of the as spun fibers was measured via SEM. After the spray coating, the average skin thickness was measured again via SEM. The difference between the two measurements was taken as the average coating thickness.
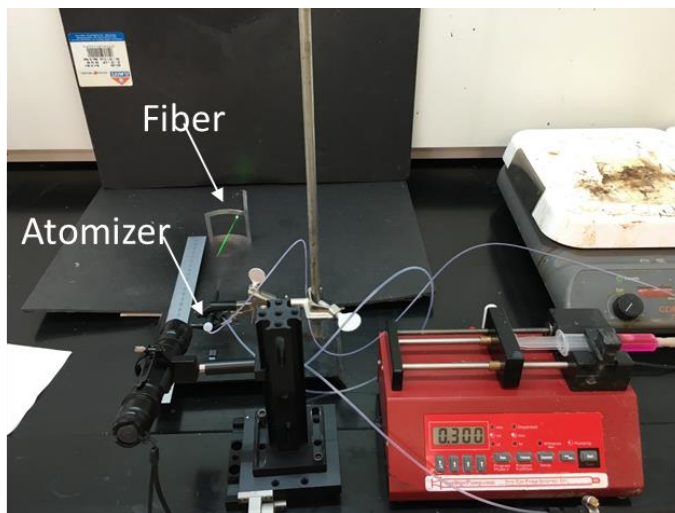
Figure 3.1 Spray coating setup for encapsulation of the fiber.

3.1.4. Solvent vapor treatment of the coating

DMF vapor treatment process was introduced to modify the morphology of the coating in order to change the release kinetics. To this end, a beaker containing DMF was first heated with a hotplate and covered with a glass chamber. The temperature inside the chamber was set to 50 °C. After the temperature reached 50 °C, the fibers were placed in the chamber and exposed to DMF vapor for 10 minutes.

3.1.5. Characterization of the release of functional materials

An Olympus FV1000 confocal microscope with 100x/1.4 oil immersion objective was used to examine the coating and study the release of encapsulated BAC. In some cases, imaging was carried out in an oil medium to enhance image resolution. Z-stacked images of fibers with a layer thickness of 0.4 μm was also obtained to better assess the filling quality. DI water was used as medium for radial release tests, and DI water doped with fluorescein (Sigma-Aldrich) was used as a medium to evaluate longitudinal release of the encapsulated material.

3.2. Results and discussion

3.2.1. Loading porous fiber with functional material via carrier solvent

The encapsulated functional materials were carried into the porous fiber in solution form. Hence, wettability of the fiber material by the solution is critical to achieve successful loading. This was achieved in our study by the proper choice of the carrier solvent (ethanol), but in a more general case it can also be enhanced by surface treatment of the fiber, such as plasma treatment or surface functionalization. A suitable solvent for

this process, in addition to being a good solvent for the encapsulated material, needs to: (1) be a nonsolvent for the porous fiber material, (2) be sufficiently volatile, such that it can be evaporated at temperatures below the T_g of the fiber, and (3) have high wettability for the fiber to facilitate the filling process. Ethanol as the solvent for BAC satisfies all these conditions: the solubility of BAC in ethanol is as high as 70 wt.%, ethanol can be evaporated even at room temperature, the solution wets the fiber material (PMMA) with a low contact angle (θ as shown in Figure 3.3a). The contact angle between the BAC solution and the fiber material (PMMA) is measured to be 21.4±0.4° (average and standard deviation of 5 tests), as shown in Figure 3.2. Moreover, ethanol is a nonsolvent for PMMA.
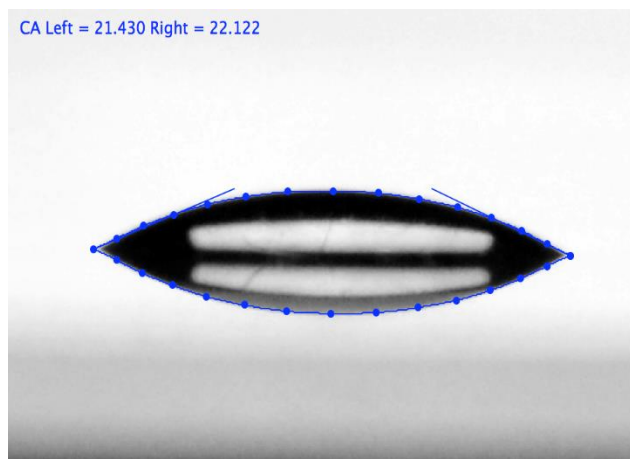
Figure 3.2 Contact angle test of BAC/ethanol on PMMA.

Fluid flow in a porous media can be described by Lucas-Washburn equation as shown in Equation (3.1)[160]:

$$l^2 = (\frac{g}{h}\frac{\cos q}{2})rt$$

(3.1)

66

where t is the time for a liquid with dynamic viscosity η, contact angle θ and surface tension γ to penetrate a distance l into the capillary with pore radius of r. In our experiment, the fiber was first filled under atmospheric pressure and then put into low pressure chamber to extract the trapped air. Based on the L-W equation, the theoretical filling time was calculated to be a fraction of a millisecond and could not be experimentally measured.

Figure 3.3b shows an SEM image of a BAC loaded fiber. When compared with images of an empty porous fiber (Figure 2.4b), a great portion of the fiber is loaded with BAC. The BAC loading was also confirmed with confocal fluorescence imaging (Figure 3.3c), in which fluorescent molecules had been added to the BAC solution. Spherical unfilled pockets inside the fiber, potentially trapped air, can also be seen. To qualitatively characterize the BAC loading, the loading efficiency, defined as the ratio of the filled volume to total volume of the fiber was estimated from SEM images (cross sectional average) and confocal fluorescence images (volumetric average):

$$\eta_{loading} = \frac{A_{filled}}{A_{fiber}} \times 100\% = \left(1 - \frac{A_{empty}}{A_{fiber}}\right) \times 100\% \tag{3.2}$$

A loading efficiency of 80%±7% and 73%±4% was measured from SEM images and confocal fluorescence images respectively, as shown in Figure 3.4. To estimate the loading efficiency, SEM images of fiber cross-section and z-stack confocal fluorescence images of BAC loaded fibers were analyzed by ImageJ software. The total fiber cross-section area of the fibers and area of empty pores were measured from SEM images. On z-stack confocal fluorescence images, the total fiber area and filled area were measured on each z slice and an average was calculated between different z slices to get the final

67

loading efficiency. Multiple fibers (6-8) were analyzed for each case to guarantee reproducibility of the results. We believe the loading efficiency estimated from confocal images is more reliable and representative, because it is calculated on the entire volume of the fiber.
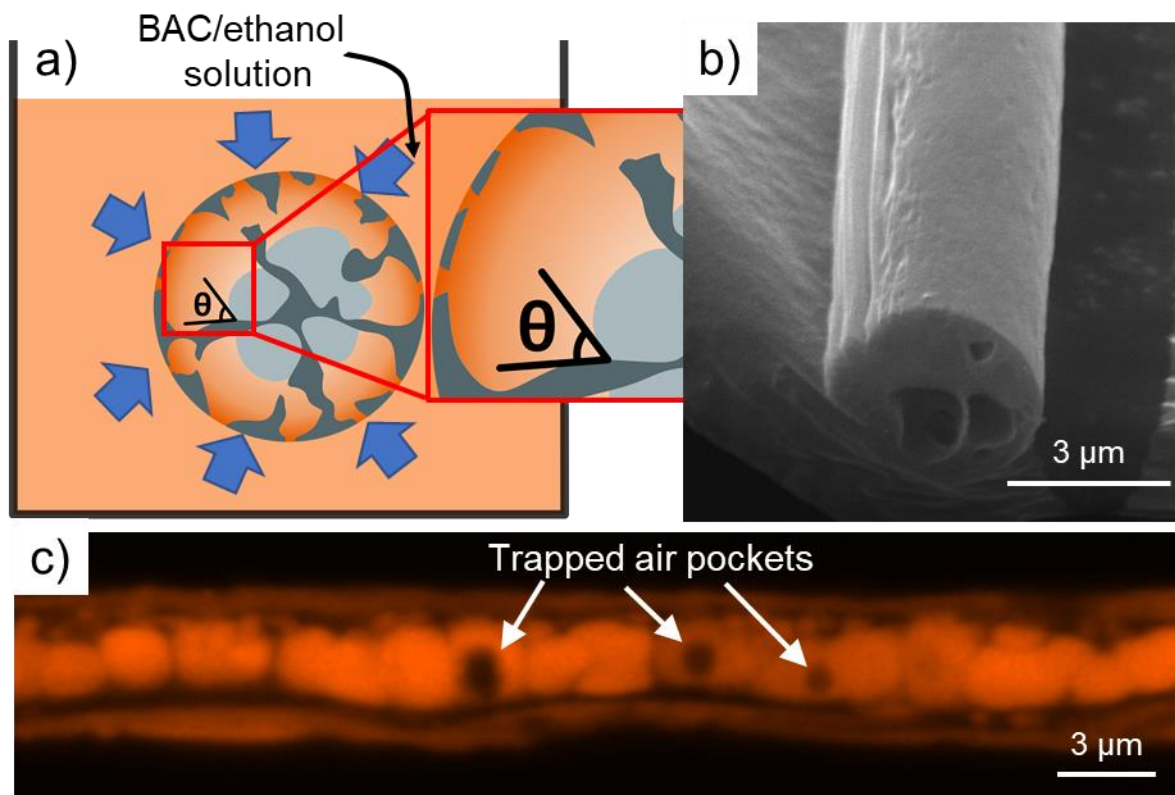
Figure 3.3. a) Schematic of our method to load the fibers assisted with surface tension. The functional material, BAC, is carried into the fiber via a carrier solvent, ethanol, which is subsequently evaporated out. b) SEM image of the cross section and c) Confocal fluorescence image of a BAC loaded porous PMMA fiber in which Rhodamine B was used as the fluorescent tag. Reprinted from [41] with permission.
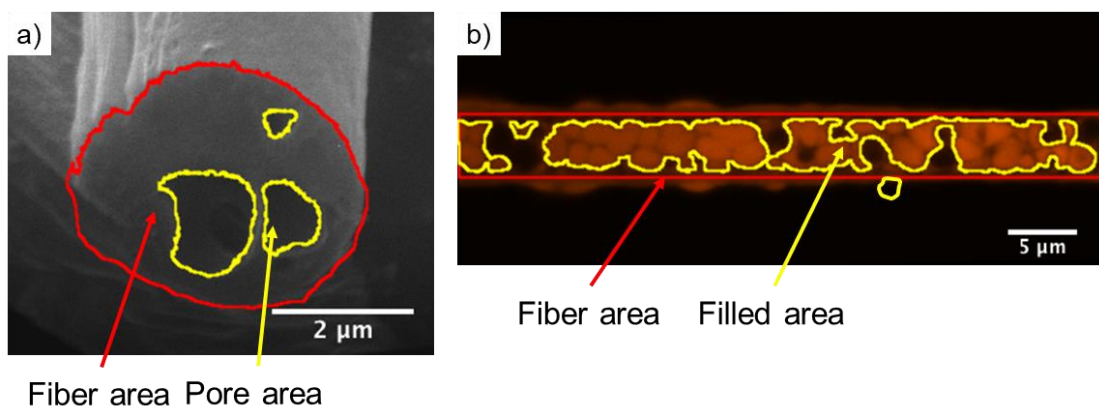
Figure 3.4 Estimation of loading efficiency from a) SEM images, b) confocal fluorescence images of the BAC loaded porous PMMA fibers. Reprinted from [41] with permission.

To further characterize the loading of BAC, the density of the BAC loaded in the fiber was estimated from the loading efficiency measurements of the confocal fluorescence images. Assuming that the BAC solution fills all the voids in the fiber during the filling process, and all the BAC that enters the fiber in the form of BAC-ethanol solution remains there after ethanol is evaporated, the mass of the BAC loaded inside the fiber can be estimated as the product of the total pore volume (obtained from confocal microscopy images) and solution concentration. By normalizing the estimated mass of the encapsulated BAC with the pore volume, the density of the encapsulated BAC was estimated to be 0.91 ± 0.04 g/cm^3. This value is comparable to the density of bulk BAC (0.98 g/cm^3). It is to be noted that the microscale voids such as those attributed to trapped air pockets in Figure 3.3c are excluded from the calculation of the BAC volume. Hence, the slightly lower measured density of the encapsulated BAC compared to bulk BAC suggests the formation of nanoscale voids below the resolution of optical microscopy in the encapsulated BAC.

69

3.2.2. Spray coating and annealing of the coating via solvent vapor treatment

Encapsulation of the functional material was achieved by applying a polymer coating on the fibers, the polymer coating serves the purpose of mediating the release of the functional material. For this purpose, PMMA solution was spray coated onto the fiber to encapsulate the functional material. In this approach, as the coating material is sprayed onto the fiber in a solution, the solvent gradually evaporates. If the fiber-nozzle distance is sufficiently long, the coating material can reach the fiber with nearly no solvent content. Hence, this approach if implemented with right processing parameters, can be considered a form of dry coating, which is essential to minimize filler-coating inter-diffusion and mixing.

The SEM, AFM and confocal fluorescence microscopy images of the dry-sprayed coating on an empty fiber is shown in Figure 3.5. As shown in the confocal fluorescence images, the coating material does not enter the fiber, suggesting suppressed mobility of the coating polymer chains as they reach the fiber. This is primarily due to sufficiently long nozzle-fiber distance, along which the coating solution has lost most of its solvent content. Moreover, the coating thickness was controlled by adjusting the spraying time. To characterize the coating thickness as a function of spraying time, spraying time of 1 min, 4 min and 10 min were studied. Coating thickness was measured via SEM imaging on 10-20 coated hollow fibers for each case (duration of spraying) and shown in Figure 3.6a. SEM images for different spraying time are shown in Figure 3.6b,c,d.

A more careful study of the coating morphology, however, reveals that although the dry coating covers most of the fiber surface, small cracks and openings can be seen on the coating in both SEM, AFM and confocal images (Figure 3.5a,b,c). These imperfections may serve as pathways for the encapsulated functional material to diffuse out which may lead to very high release rate. The cracks and openings are side effects of spray coating. In other words, as the droplets of the coating material dissolved in DMF fly from the spray nozzle towards the fiber, they lose solvent by evaporation. Therefore, the mobility of the chains in the coating material is suppressed considerably, and gaps remain between the coating particles on the fiber surface. Hence, we pursued further annealing to eliminate the surface gaps and openings.

To this end, fibers coated with the PMMA coating were treated with DMF vapor (schematic shown in Figure 3.5d). The diffusion of DMF molecules into the PMMA coating lowers the activation energy for self-diffusion (E_a), as described by the diffusion constant $D = D_0 e^{-E_a/RT}$ [161], so that the polymer chains can diffuse into less concentrated areas, i.e., crack-like openings and holes in the coating at temperatures below the glass transition temperature of PMMA. In other words, the introduction of the solvent molecules in between the polymer chains reduced the energy barrier for diffusion. As seen in Figure 3.5e,f,g, the opening and cracks in the coating are mostly removed after the DMF vapor treatment.
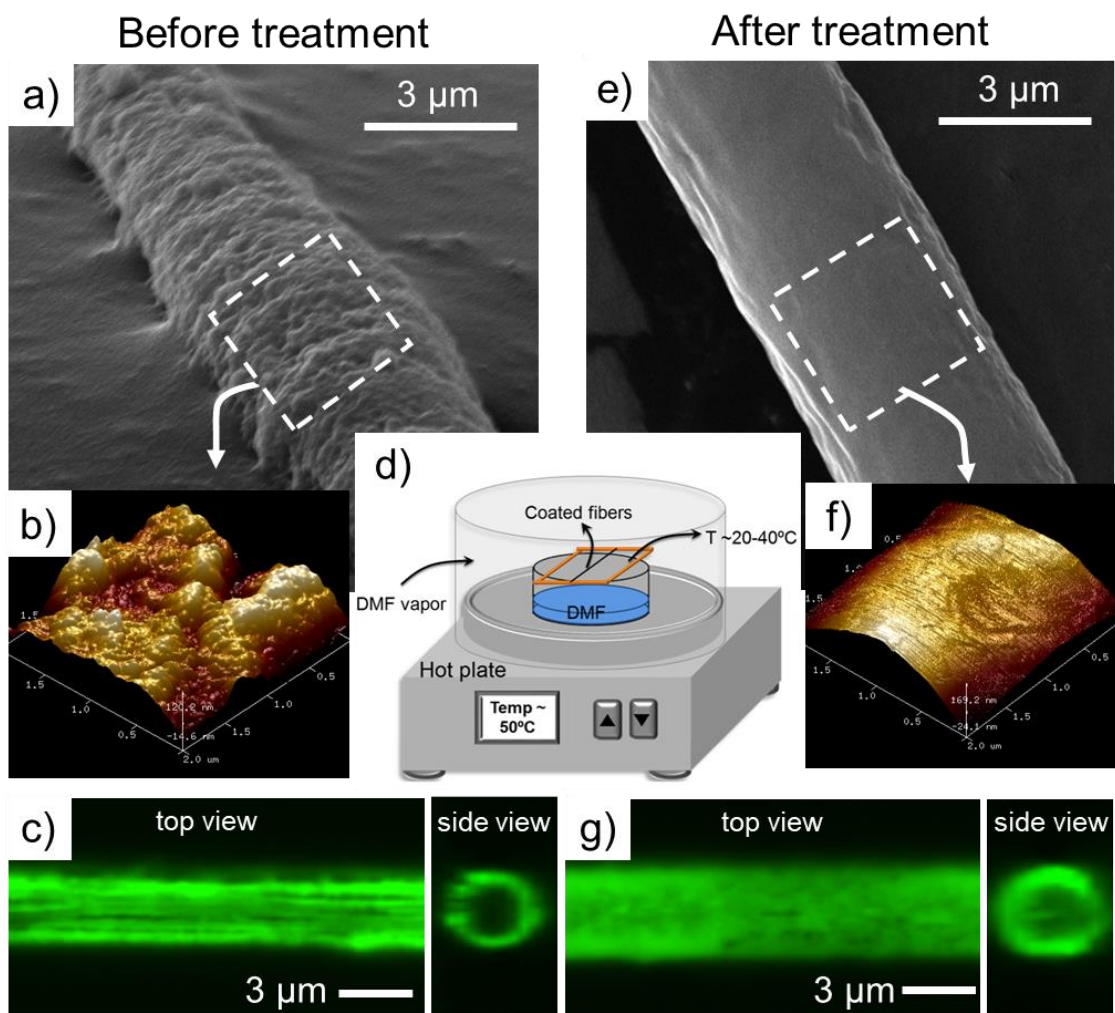
Figure 3.5. SEM and AFM images of the coating a), b) Before and e), f) After vapor treatment. Confocal fluorescence images of coating c) Before g) After vapor treatment. d) Schematic of the DMF vapor treatment which is used to eliminate surface defects, including incomplete coating and crack-like openings in the coating, in spray-coated skin of the fiber. Reprinted from [41] with permission.
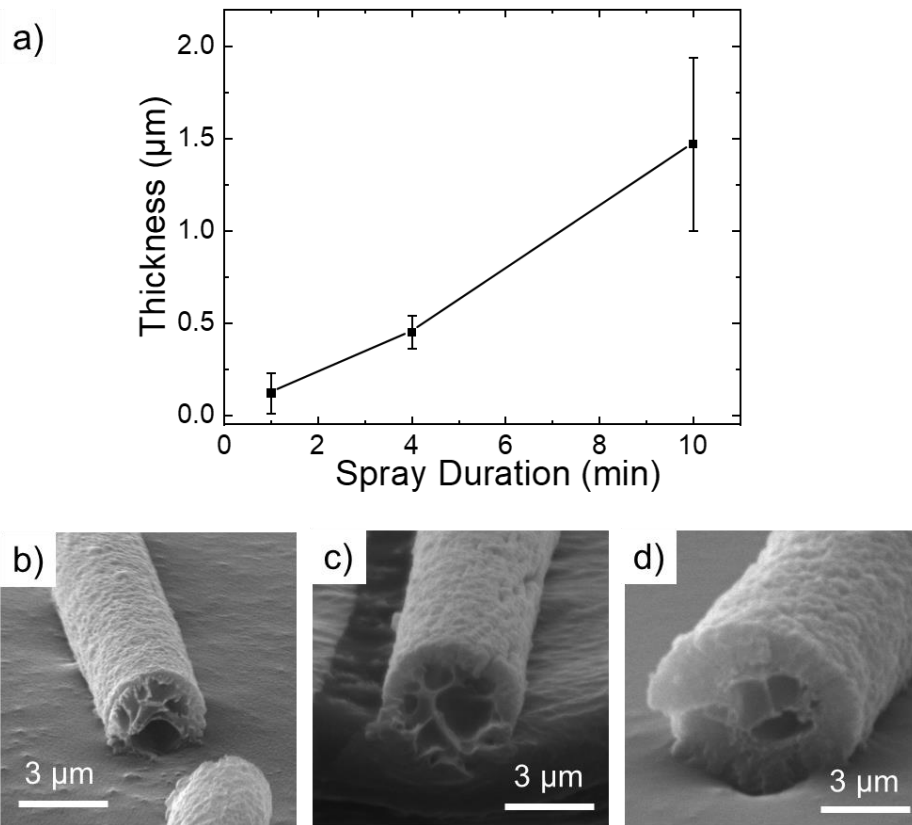
Figure 3.6 a) Coating thickness vs spray duration. SEM images for different spray coating duration: b) 1 min. c) 4 min. d) 10 min. For each coating time, coating thickness was measured on 10 fibers. Reprinted from [41] with permission.

3.2.3. Passive release of functional material

The passive release of the encapsulated material from the fiber when it was submerged in water (Figure 3.7a). Confocal fluorescence microscope was used to measure the release time of functional material from the fibers, an indicator of the total time required for BAC to be released after the fiber is exposed to water by tracing the fluorescent dye that was added to the BAC solution during loading (Figure 3.7b,c,d). To measure the release time, the images were first corrected for photo bleaching using

histogram matching method. After bleach correction, the average intensity of the fiber was normalized with respect to the fluorescent intensity before and after the release. The characteristic release time was measured as the time at which the slope of the fluorescent intensity vs. time curve is maximum, which correspond to an accelerated change in fluorescent contrast in the pores in the confocal images. The dye and the BAC have comparable diffusion constants in water and their molecules have comparable sizes. Thus, we expect similar mobility and release time for both.

To study the release with fluorescence microscopy, the following considerations need to be made. First, because the intensity of the fluorescence is highly dependent on the environment (e.g. ion concentration, pH), it will change with the penetration of water into the fiber, the local water content, and often water infiltration increases the fluorescent radiation. Second, photo bleaching may occur during the test which will lead to decreased intensity over time. Typical durations to observe a noticeable photo bleaching in our experiments are ~30 minutes to 1 hr. Based on these, when analyzing the release with fluorescence intensity, the image contrast at any particular time is a better indicator of the release than the variation of the intensity with time.

The release time for dry coated fiber was approximately 30 sec, whereas the release time for the uncoated fiber was below 2 sec (limited by imaging frame rate). Therefore, the dry coating does suppress the release of BAC. However, duo the surface defects on the dry coating, the coating does not mediate the diffusion of the functional material as intended and a relatively fast release rate was observed.

As discussed in previous section, the solvent vapor treatment can eliminate the surface defects, thus the release rate should increase significantly after the treatment. As a result, a corresponding 15 min release time, 30-x increase compared to a release time of 30 seconds for untreated coating (Figure 3.7c), confirmed the improvement in coating quality as a result of DMF vapor treatment. Our annealing procedure to remove surface cracks from the thermoplastic coating takes place at temperatures considerably below the glass transition temperature of PMMA (T_g). Hence, no degradation of functional materials is expected. The key to successful annealing of the coating in this method is proper timing. Exposure of the fiber to the DMF vapor for an extended period of time should be avoided, as it can lead to the diffusion of the DMF to the fiber itself (passed the skin), which can eventually dissolve the fiber and irreversibly lower its load bearing capacity.

Complementary to the above approach the release time can be controlled by changing the thickness of the coating. A thicker coating should result in a longer release time. To confirm this, two coating cycles (dry coating followed by DMF vapor treatment) were applied to increase the coating thickness. The resulting release time was nearly tripled to approximately 53 min (Figure 3.7d).
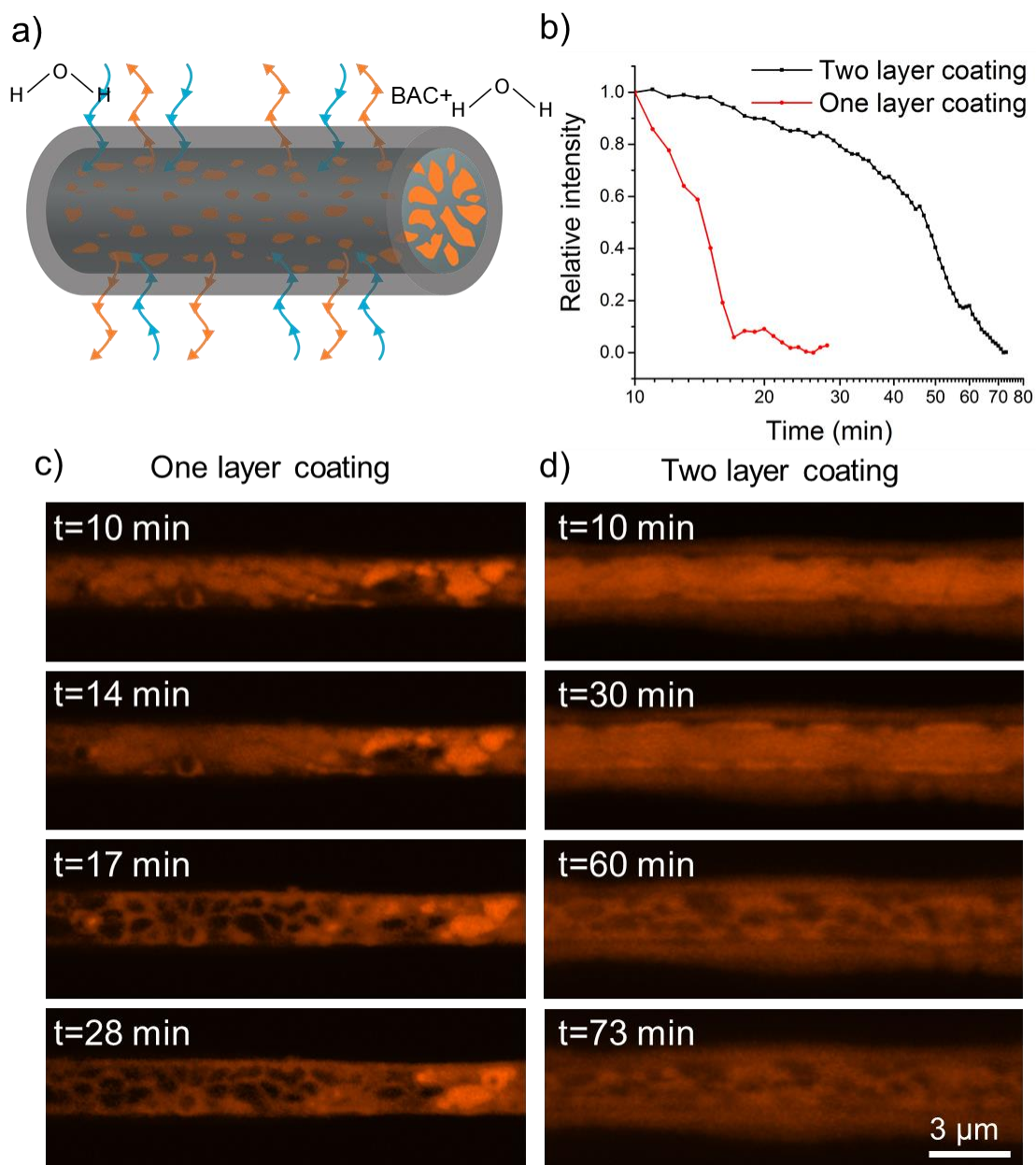
Figure 3.7 a) Schematic of controlled radial release which is based on diffusion of water molecules across the coating into the fiber, followed by dissolving the encapsulated salt and outward diffusion. b) Relative intensity of the fluorescent dye as a function of time for coated fibers, pointing to the controlled radial release of the salt which is a function of coating thickness. Time-lapse confocal fluorescence images of BAC release when the fiber is placed in an aqueous environment for c) One-layer coated fiber and d) Two-layer coated fiber at different times. Reprinted from [41] with permission.

The aforementioned release mechanisms are through the radial diffusion of water into the fiber across the coating, followed by dissolving the BAC and diffusing outward. In addition to the controlled radial release, the axially interconnected pore structure (thus, continuous encapsulated material within the fiber) allows for large volume release upon fiber fracture when the functional material is transported axially. To study the axial release, we fractured the fiber by loading it axially to failure and exposed the fractured surface of the BAC loaded fiber to water. The experiment was carried out under a confocal fluorescence microscope and the BAC and water were doped with fluorescent dyes, Rhodamine B and Fluorescein, respectively, to trace the motion of BAC and water. After exposing the fiber end to a water droplet, we observed a bright green fluorescing region that formed at the fractured end of the fiber, which grew away from the fractured end, indicating the inward water flow (Figure 3.8c). The velocity of waterfront as it entered the fiber axially seems to be much faster than capillary flow described by L-W equation. This is believed to be caused by the hydrophilicity of BAC which facilitates water penetration. The right-to-left water movement was accompanied by a left-to-right displacement of red dye (Rhodamine B), as it diffused out of the fiber through the penetrated water. Since Rhodamine B and BAC have similar diffusivity in water, the fluorescent intensity of the Rhodamine B represents the relative concentration of BAC in water, which points to the release of BAC from the fractured end of the fiber through the penetrated water.
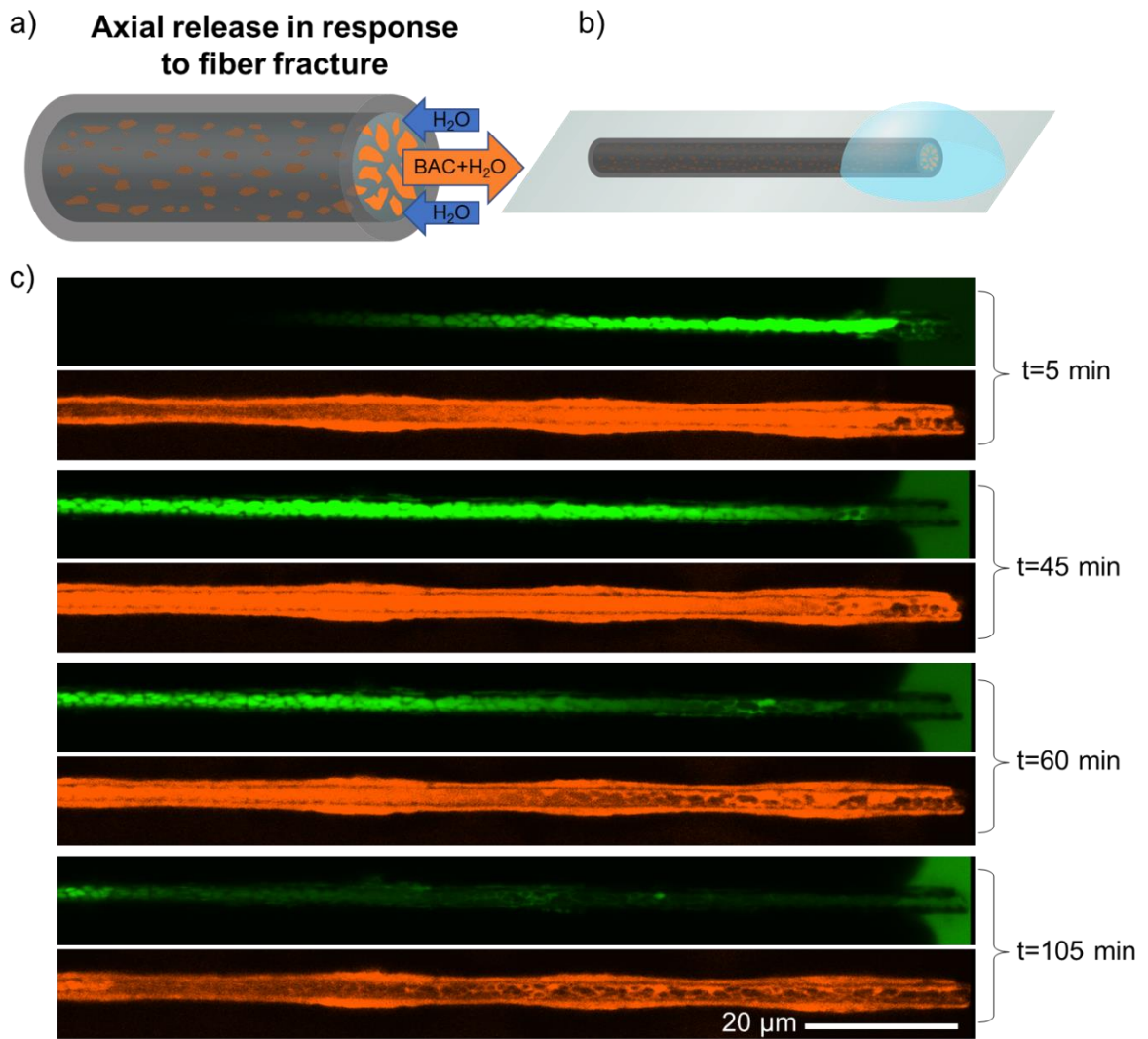
Figure 3.8 a) Schematic of axial release of BAC in response to fiber fracture which is based on the flow of water inside, dissolving the interior BAC and carrying it out. b) Schematic of axial release. c) Time-lapse confocal fluorescence images of axial release from fractured surface at different times, demonstrating the release of the salt within a considerable length of the fiber (~100 μm for a ~5 μm thick fiber). Reprinted from [41] with permission.

3.3. Conclusion

In this chapter, we have presented the successful demonstration of sequential fiber processing, encapsulation of functional materials and controlled release. This method may possibly allow a wide range of materials to be processed into porous fibers. This versatility is rooted in the sequential nature of the processing of the porous fibers, followed by loading the fiber with functional materials, followed by encapsulation for controlled release. We have demonstrated this concept on porous PMMA fibers, which were loaded with an antibacterial salt (BAC) and coated with sub-micron PMMA dry-sprayed coating.

The porous fibers were loaded with BAC that was introduced into the fiber via a carrier solvent. The estimated value of the density of the encapsulated functional material (BAC in this case) and its comparison with the bulk density of the material suggests that the loading process is as follows. First, the functional material dissolved in a carrier solvent (ethanol) enters the pores during the loading process and nearly entirely fills all the pores of the fiber. This is followed by solvent evaporation during which most of the BAC that is in the fiber as a part of the solution will remain there. The solvent evaporation may leave some nanoscale pores in the fiber, thus slightly lowering the apparent density of the loaded functional material. Moreover, our results point to the controllability of radial release by adjusting the coating thickness and morphology of the coating, radial release with a release time ranging from a few seconds to 53 minutes (more than 100x change in rate of release) was achieved. In addition, axial release of the encapsulated material was demonstrated as a means to release a considerable volume of the functional material (as much as 70-90% of the fiber total volume in some sections).

4. ENCAPSULATION AND ACTIVE RELEASE OF FUNCTIONAL MATERIAL IN CONDUCTIVE POROUS CARBON NANOFIBER

The feasibility of the proposed porous fiber platform for encapsulation and passive release of functional material was demonstrated in previous chapter. This sequential processing method allows for high mass loading of functional material in the porous fibers and also allows for controllable passive release. Furthermore, as discussed in Section 1.3, the other advantage of the porous fiber platform is the flexible release mechanism, including active and on-demand release when a conductive porous fiber is used as the host for encapsulation.

In this chapter, the encapsulation and active release of functional material using the porous CNFs developed in Section 2.3 will be presented in which electrical signals are used to regulate the release by means of Joule heating. First, porous CNF yarns consisting of multiple porous CNFs is fabricated. Functional material is loaded into the porous CNF yarn using carrier solvent similar to the method discussed in previous chapter. Next, a more efficient coating method for encapsulating the porous CNF yarn is studied. Finally, the active and on-demand release of the encapsulated functional material in response to electric signal is investigated. A setup was developed to monitor the temperature of the fiber in situ, by benefitting from the dependence of the fiber resistance on temperature. The active release mechanism, enabled by Joule heating the fibers, was investigated in detail. The permeability of the coating was measured as a function of the fiber temperature.

The results indicated an Arrhenius type of dependence, an indication of the diffusion-based release mechanism.

4.1. Existing method for active and on-demand release

Active and on-demand release of functional materials in response to environmental stimuli or applied electric signals, can open up new frontier in areas such as smart textile, autonomous composite, wound dressing and drug delivery. The on-demand drug delivery release technologies attracted great attention in in recent decade[162]. A few different mechanisms for on-demand release of bio-active agent has been studied for drug delivery purposes. These mechanisms will be reviewed in this section to shed light on the method to achieve active and on-demand release for a wide range of applications such as smart textiles and multifunctional composites.

In order to achieve active and on-demand release, the material which contain the encapsulated material need to change its permeability in respond to an external stimulus. Such stimuli include temperature, electrical field, light, magnetic field, chemical or a combination of them[162]. Temperature is usually the easiest way to control material property and it can usually be coupled with other stimuli such as light[163], electric field[164, 165] and magnetic field[166, 167] to activate the release. Several active and on-demand drug delivery systems have been developed based on this mechanism. In one study, reduced graphene oxide was embedded into electrospun poly(acrylic acid) nanofiber, antibiotics were loaded by soaking the nanofibers in antibiotics solution. The release of the antibiotics was activated by photothermal heating using a laser source, and the release rate of the

antibiotics were tunable through power density of the applied laser[163]. Another group of researchers utilized the Joule heating effect to achieve active and on-demand release of bio-active agent[164, 165]. In these methods, a conductive carbon ink was printed into a pattern or coated on non-conductive material containing thermoresponsive drug carriers, and the release was activated through electrical heating by running current through the conductive carbon ink. The magnetic thermal coupling was also explored for active release purpose.[167] In one study, nanofibers based on temperature-responsive polymer Poly(N - isopropylacrylamide) (PNIPAAm) and copolymer of PNIPAAm containing magnetic nanoparticles and bio-active agent was fabricated by electrospinning. The active release was triggered by applying an alternating magnetic field which heats up the magnetic nanoparticles. An 'on-off ' release of the bio-active agent from the nanofibers was demonstrated in response to the applied alternating magnetic field.

In the aforementioned approaches for on-demand drug delivery, the active and on-demand release behavior is highly material dependent, and the activation happens at a very narrow temperature range. For example, in the method utilizing Joule heating[164], the on-demand release relies on the sol-gel transition of PEGylated-chitosan at the critical temperature of ~37 °C.[164] Similarly, in the method based on magnetic heating[167], the on-demand release relies on the transition between swelling to deswelling state of PNIPAAm at the critical temperature of ~48 °C. These material related limitations impose a great limitation on material selection, and the narrow operational temperature range could potentially limit their application in other fields such as multifunctional composites and smart textiles. To address these limitations and develop a more widely applicable active

release platform, rather material agnostic methods needs to be developed. As discussed in Section 1.3, the porous fiber encapsulation platform offers greater freedom in material selection which is rooted in the sequential processing. In this chapter, we propose to study the on-demand release by controlling the diffusion rate by means of Joule heating of a conductive porous fiber. It is well known that diffusion coefficient in solid at different temperature can be well predicted by the Arrhenius equation[168, 169]: $D = D_0 \exp\left(-\dfrac{Q_d}{RT}\right)$.

As temperature increases during Joule heating, the diffusion coefficient will increase significantly which can be uesd to activate the release of functional material. In this work, this release mechanism will be studied in details to achieve active and on-demand release of functional material.

4.2. Experimental method

In order to increase the amount of functional material that can be loaded and released on demand, yarns of porous CNFs containing multiple fibers were fabricated and used instead of single CNF fiber. The larger mass of the functional material stored allows us to more reliably detect the material release. The porous CNFs fabricated with PAN:PMMA ratio of 1:1 and core/shell flow ratio of 1.4 from Section 2.3 is used. The individual CNFs have a hollow core and porous shell which served as a reservoir to store functional material.

4.2.1. Fabrication of carbon nanofiber yarns

The electrospinning was conducted using method mentioned in Section 2.3.1 with PAN:PMMA ratio of 1:1. The precursor fibers were collected using a grounded rotating disk (5 cm wide) with an angular velocity of 500rpm (take up velocity of 3.9 m/s). After electrospinning for 60 min, the precursor fibers ribbons were collected from the disk collector and the ribbons were cut into 15cm long, 4 mm wide ribbons. The 4 mm wide ribbons were twisted into yarns. To achieve this, one end of the ribbon was clamped, and the other end was attached to a motor shaft rotating at 60 rpm. The yarns were twisted with a twist of 330 turn per meter (tpm). Higher than 330 tpm twists were avoided as they resulted in fracture of the yarns. The yarns were then stabilized in a convection oven at 270 °C for 2 hrs in an air atmosphere. The stabilized yarns were then transferred to a tube furnace (MTI GSL-1700X) and carbonized in nitrogen atmosphere at 1100 °C for 1 hr to convert the polymer precursor into carbon. During the pyrolysis process, PAN phase turned into turbostratic carbon and PMMA left the system in the form of volatile species. As a result, hollow CNFs with porous shell were formed as previously discussed in Section 2.3.2.

4.2.2. Loading CNF yarns with functional materials

The functional material of choice in this study was Gentian violet (GV). GV was selected for several reasons: first, it is widely used antibacterial material with high solubility in water and alcohol.[170, 171] Second, GV solution have a distinctive violet color

which can be easily detected during the release test both visually or using UV-vis spectroscopy.

To load the CNF yarns with GV, a GV/ethanol solution was first made by dissolving GV in ethanol at a concentration of 55 wt%. The CNF yarns were soaked in the GV/ethanol solution for 30 sec. The GV/ethanol solution has low viscosity and it can easily wick into the porous CNF yarn and fill the pores. After soaking, the CNF yarn was taken out and dried for 10 mins at room temperature, during the drying, ethanol in the solution evaporates and left behind the solid GV loaded in the CNF yarns.

4.2.3. Encapsulation of loaded CNF yarn via dip coating

After loading CNF yarn with GV, a thin layer of Polycaprolactone (PCL) was coated on the yarn by dip coating for encapsulation. PCL was selected as coating materials due to its excellent biocompatibility[172] and low melting point (60 °C). To keep the loaded material in the CNF yarn during the coating process, the solvent of the coating material should be a non-solvent for the loaded material. Among various solvents which satisfy this condition, in this work, toluene was selected as solvent for PCL duo to the low solubility of GV in toluene. For this purpose, PCL with average molecular weight of ~14,000 (Sigma) and ~25,000 g/mol (Polysciences, Inc) was dissolved in toluene at 38 wt.%. The CNF yarn loaded with GV was dipped into the PCL/toluene solution and then pulled out from the solution vertically at a withdrawing speed of 3.7 mm/min. The pulling speed was controlled using a syringe pump as shown in Figure 4.1. After the dip coating,

the samples were dried for 10 mins at room temperature for the toluene in the coating to evaporate.
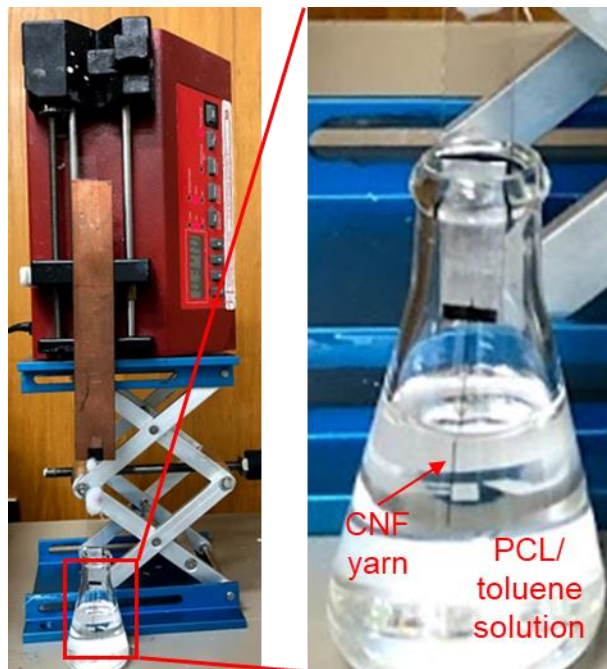
Figure 4.1 Experimental setup for dip coating on CNF yarn.

4.2.4. Characterization of the release profile

The active release profile of GV from bundle of porous CNFs was defined as the rate of the GV released in an aqueous environment, normalized by the initial GV content of the bundle as a function of time and the applied electric voltage. The main mechanism of release was an increase in permeability of the coating at elevated temperatures which are caused by Joule heating.

The release profile of GV was tested by immersing the GV loaded CNF yarn in DI water and measuring the concentration of GV with UV-vis spectroscopy. To prepare the sample for this test, the two ends of GV loaded CNF yarn was dipped into toluene to

86

remove the PCL coating therefore exposing the conductive CNF. Next, the tips of the yarn were attached to the copper electrodes on a glass substrate separated by 2 cm using silver conductive paint (SPI Supplies). The sample was dried for 12 hrs at room temperature for the silver conductive paint to reach optimum conductivity. A picture of the prepared sample is shown in Figure 4.2a.
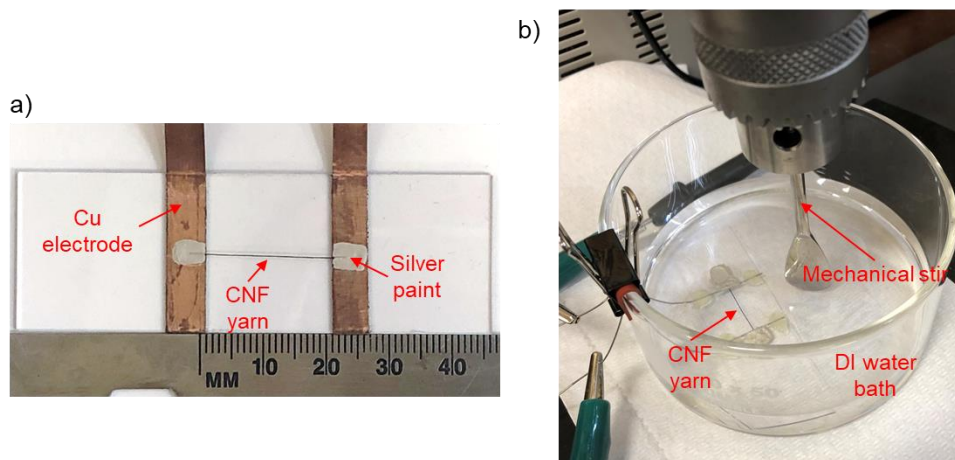
Figure 4.2 a) CNF yarn sample for release profile test, b) experimental setup for the release profile test.

The prepared sample was then immersed in water bath filled with 80 ml of water, as shown in Figure 4.2b. A mechanical stirrer was used to mix the solution at 500 rpm to uniformly disperse the GV within the solvent. As presented later in this chapter, the uniform dispersion of the GV assisted us in evaluating the quantity of the released material as a function of time.

To initiate the release, the temperature of the sample was increased by applying a voltage ranging from 0 to 20V across the sample using a DC power supply (RSR DC Power Supply HY3005F-3). A multimeter (Keithley 2110 5 1/2 Digit Multimeter) was

used to record the voltage across the CNF yarn and the electric current (I) through the CNF yarn. To determine the release profile, 3 ml samples of the solution were taken out at different times during the release experiment and the concentration of the released material was estimated via UV-vis spectroscopy. To keep the volume of the release medium constant, 3 ml of DI water was added into the medium after taking out each sample. The final concentration was calculated considering this dilution effect. The cumulative release (%) was then calculated as $\text{Cumulative release (\%)} = C_t / C_\yen$ where C_t is the concentration of GV at certain time and $C_\yen$ is the concentration when all GV is released, which is calculated using the average GV mass loaded in the yarn (2.03 ± 0.23 µg/ml).

To calculate the concentration of GV from the UV-vis spectra, a calibration curve was constructed: UV-vis absorption spectra of GV/water solution with varying concentration was measured by Shimadzu UV-2550 UV/VIS spectrophotometer from 400-700nm. The spectra are presented in Figure 4.3a. GV showed absorption peak at 590 nm, the peak absorption is plotted against the concentration in Figure 4.3a. As can be seen, the peak intensity followed Beer–Lambert law[173] which is a linear relationship between the absorption intensity and solution concentration.
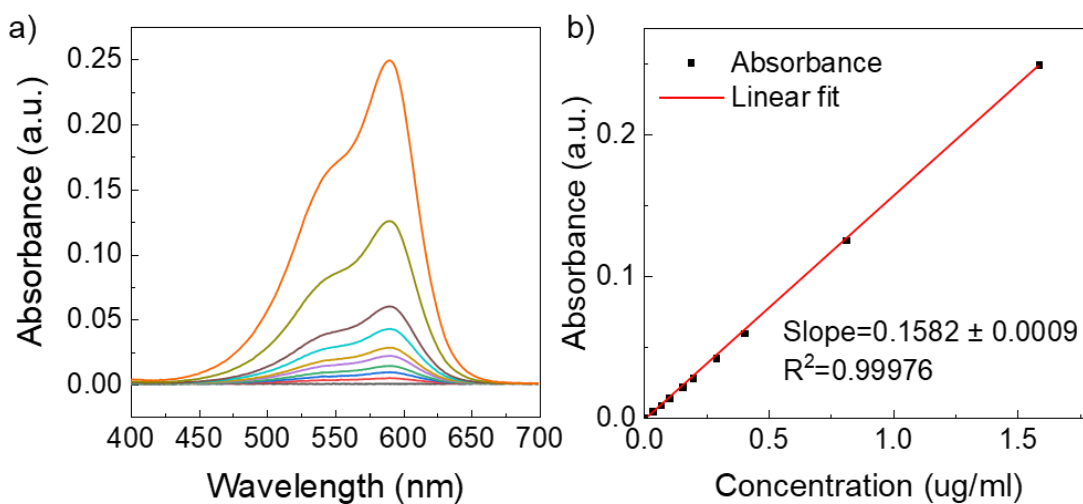
Figure 4.3 a) UV-vis spectra of GV at different concentration b) calibration curve of UV-vis.

4.3. Results and discussion

4.3.1. CNF yarn morphology

The morphology of the porous CNF yarns was characterized by SEM. As shown in Figure 4.4, the CNF yarn was uniform in diameter, the CNFs within the yarn were aligned along the longitudinal direction. The average yarn diameter measured on ten different samples was 154.9 ± 8.9 μm, which composed of CNFs with average outer diameter of 1.72 ± 0.44 μm. The cross-section of the CNF yarn is shown in Figure 4.4d-f. The CNF yarns have a hierarchical porous structure. Pores with different sizes can be observed at different location on the CNF yarns. Macropores with the size between 50 to 1000 nm exist both between different CNFs and also in the core of CNFs. Mesopores with size of 2 to 50 nm were observed in the shell of the CNFs. The pores and hollow cores are well developed due to the decomposition of PMMA during the carbonization process as

89

discussed in Section 2.3.2. Total porosity of the CNF yarn is estimated to be 70.2±5.7 % using the following equation:

$$P_{yarn} = \left(1 - \frac{\lambda}{\pi r^2 \rho}\right) \times 100\% \tag{4.1}$$

where λ is the linear density of the CNF yarn measured experimentally, the average λ between different ten samples was 95.2 ± 1.4 tex (1 tex = 1 g/km), ρ is the density of PAN based carbon fiber ($\rho = 1.7 \sim 1.9$ g/cm^3).
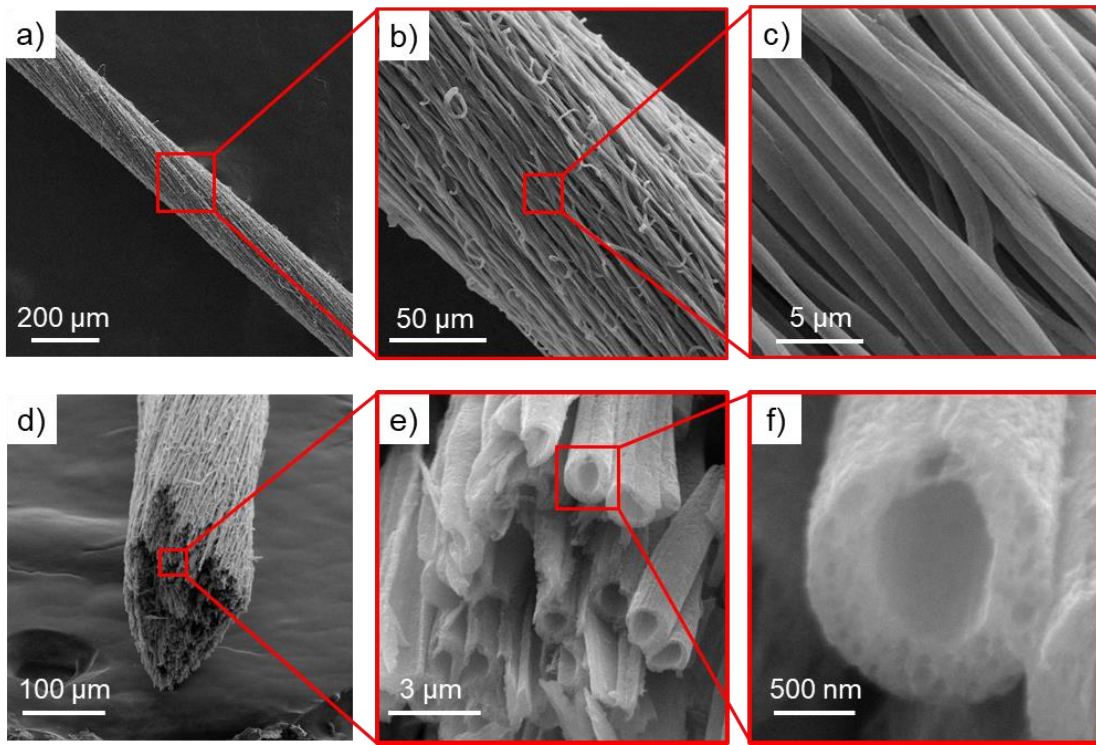
Figure 4.4 SEM image of the porous CNF yarn at different magnification

Electrical resistivity of the CNF yarn was also measured at room temperature. For this purpose, four probe resistance measurement was conducted on the CNF yarn to measure the resistance. The electrical resistivity of the CNF yarn is calculated using the following equation:

$$\rho_R = \frac{R \cdot \lambda}{\rho \cdot l} \tag{4.2}$$

where ρ_R is the electrical resistivity, R is the resistance of the CNF yarn, and l is the length

of the CNF yarn. The average ρ_R between five samples was measured to be $(87.6 \pm$

$7.8)*10^{-5}$ $\Omega.m$. The properties of the CNF yarns are summarized in Table 4.1.

Table 4.1 CNF yarn properties

Diameter (µm)	154.9±8.9
Linear density (tex)	95.2±1.4
Porosity (%)	70.2±5.7
Resistivity (10^{-5} $\Omega.m$)	87.6±7.8

4.3.2. GV loaded CNF yarn morphology

The GV loaded CNF yarn coated PCL (M_w~25000 g/mol) is characterized with

optical microscope and SEM as shown in Figure 4.5 and Figure 4.6. To image the cross-

section of the yarn, the yarns were cut with razor blade in liquid nitrogen. This was

intended to achieve a brittle failure, during which the cross section of the yarns remains

more or less unchanged. Before imaging, the yarns were coated with a 5 nm layer of Pt/Pd

using sputter coater (Cressington 208HR sputter coater) to prevent charging during

imaging. The morphology of the CNF yarn cross-section had a significant change after the

GV loading. The mesopores in the loaded CNF shell are completely filled with GV and

the macropores (core of porous CNF and pores between CNFs) are partially filled with

GV, as shown in Figure 4.6d, suggesting a capillary driven filling process.

The PCL coating was observed with both optical and SEM images. As shown in Figure 4.5 and Figure 4.6c and e, the coating thickness was uniform along the fiber length. The average coating thickness was determined by the difference of yarn diameter measured before and after the PCL coating. The average coating thickness measured on ten samples was 4.9 ± 0.5 µm.

To estimate the mass loading of GV in the CNF yarn, the weight of the CNF yarn before and after the GV loading was measured. The mass loading (%) is calculated as:

$$\text{mass loading}(\%) = \frac{\text{mass of GV}}{\text{mass of GV loaded yarn}} \tag{4.3}$$

The average mass loading of GV of five samples and was measured to be 47.4 ± 5.4 %. The linear density of GV loaded yarn was 171.2 ± 9.0 tex. And the average mass loaded of GV per unit length of the fiber was 81.1 ± 6.0 µg/mm.
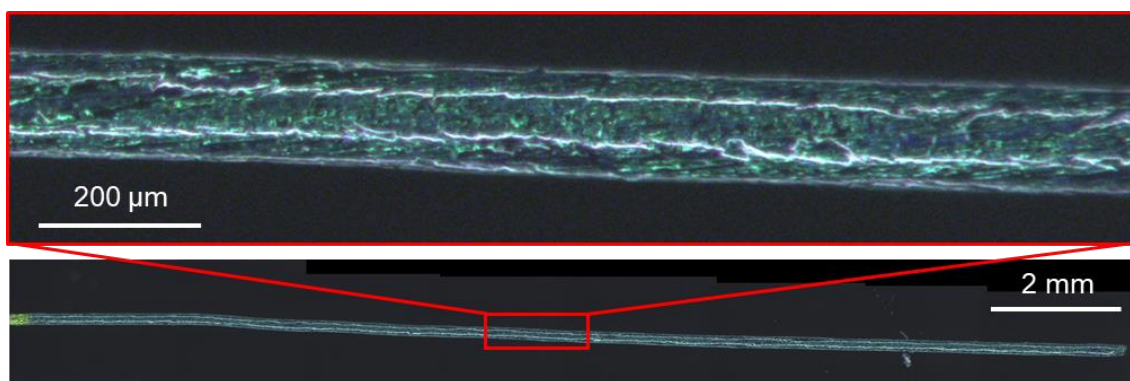
Figure 4.5 Optical image of the GV loaded yarn with PCL (Mw~25000) coating.
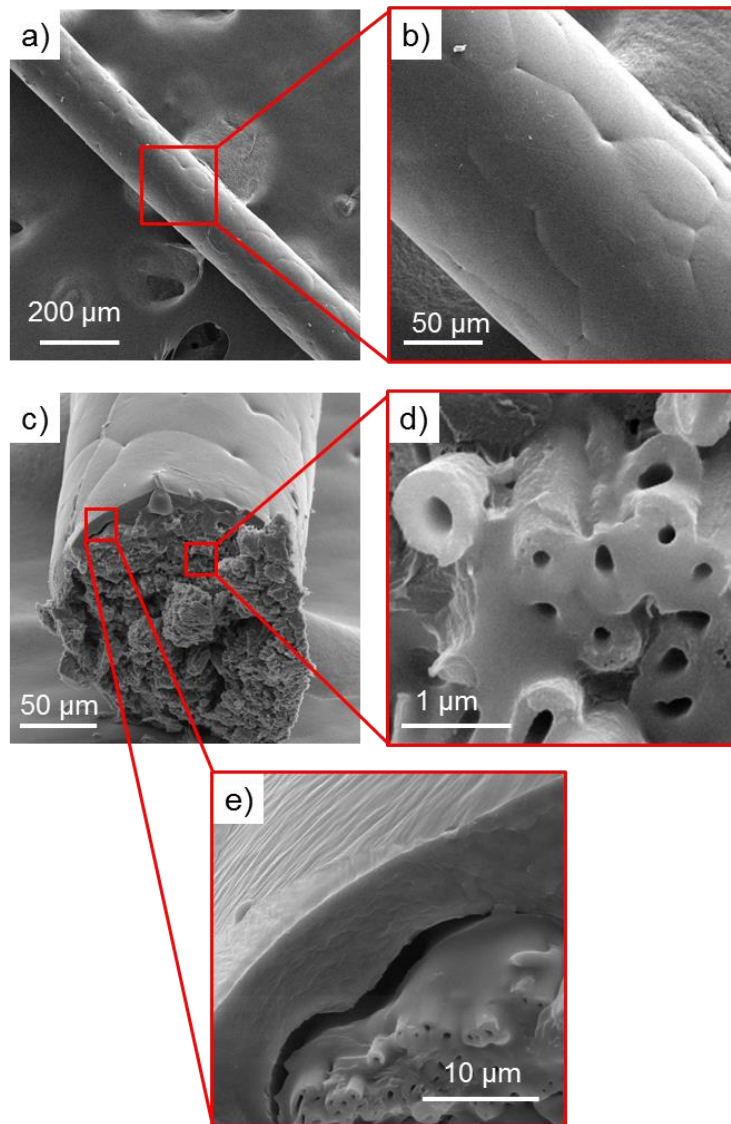
Figure 4.6 SEM image of the CNF yarn loaded with GV.

4.3.3. Measuring the temperature of the CNF yarn as a function of the applied voltage

An accurate measurement of the CNF yarn temperature with an applied power during the active release is important to understand the kinetics of release. However, to measure the temperature accurately on the small CNF yarn immersed in water using direct measurement such at thermal couple or IR thermal imaging is a very challenging task.

Therefore, other methods to determine the CNF yarn with and without the loaded material need to be analyzed.

Temperature of CNF yarn with no loaded material:

Temperature and resistance of a resistor is assumed to follow the well-known linear relationship:

$$R = R_{ref}[1 + \alpha(T - T_{ref})] \tag{4.4}$$

where α is the temperature coefficient of resistance, R_{ref} is the resistance at a reference temperature T_{ref}. The resistance of a conductor changes linearly with temperature. For semiconducting materials such as carbon and silicon, α is negative indicating the resistance decreased with increased temperature as more charge carriers are released at elevated temperatures. Given a known value of α, the temperature of the resistor can be calculated using this relationship by measuring the resistance of the resistor.

To measure α for the CNF yarns, a CNF yarn sample prepared by the method mentioned in previous section is placed in a water bath filled with DI water. The water bath is heated by a hot plate and stirred using a mechanical stir. The temperature of the water bath is measure by a thermal couple and the resistance of the CNF yarn is measure by four probe resistance measurement while the water bath is slowly heated from 23°C to 85°C. It is assumed that the fiber reaches thermal equilibrium with the water rapidly. Hence, the temperature of the fiber will be the same as the temperature of the water.

The temperature-resistance relationship of porous CNFs is shown in Figure 4.7. As expected, the resistance of CNF yarn decreases linearly with temperature. The average

94

and standard deviation of α measured on four different samples was -0.00119±0.00002

/°C. The negative value of α indicates the semi-conducting behavior of CNFs.
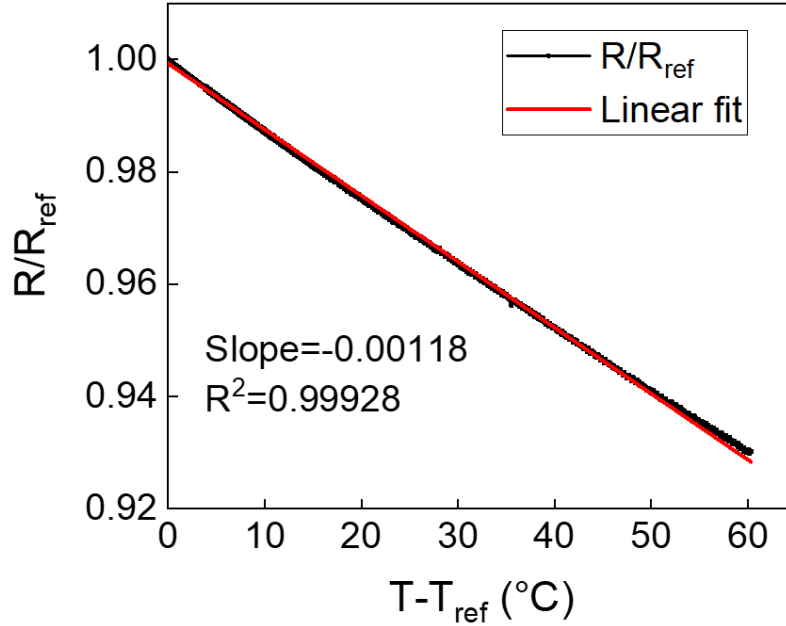
Figure 4.7 Temperature dependence of CNF resistance

      The measured value of α can be used to estimate the temperature of the CNFs as a

function of the applied voltage as follows. During Joule heating, a voltage (*V*) is applied

across the CNF yarn and the resulting current (*I*) through the CNF yarn is measured.

Therefore, the resistance of the yarn can be calculated as *V/I*, and the CNF temperature

during the Joule heating can be calculated with Equation (4.5) with the previously

measured *α*.

$$T = T_{ref} + \frac{1}{\alpha}\left(\frac{V}{IR_{ref}} - 1\right) \tag{4.5}$$

where *V* is the voltage applied across the CNF yarn, *I* is the current through the CNF yarn,

R_{ref} is the resistance of the CNF yarn measured at room temperature T_{ref}.

Temperature of CNF yarn with loaded material during release:

Determining the temperature of CNFs during the active release experiments by using the calibrated temperature-resistance relationship require the yarn to have a consistent resistance. It works well on CNF yarn without any loading of functional material. However, when the yarn is loaded with ionic compound, the release of the material can change the total resistance of the yarn which result in a deviation from the linear relationship. To address this problem, the heat transfer model the yarn with Joule heating need to be studied. Since the yarns are very long (aspect ratio > 100), the heat loss at the two ends is neglected, reducing the problem to an axisymmetric 2D problem. The schematic of the CNF yarn is shown in Figure 4.8 and the governing equation for steady state heat conduction is:
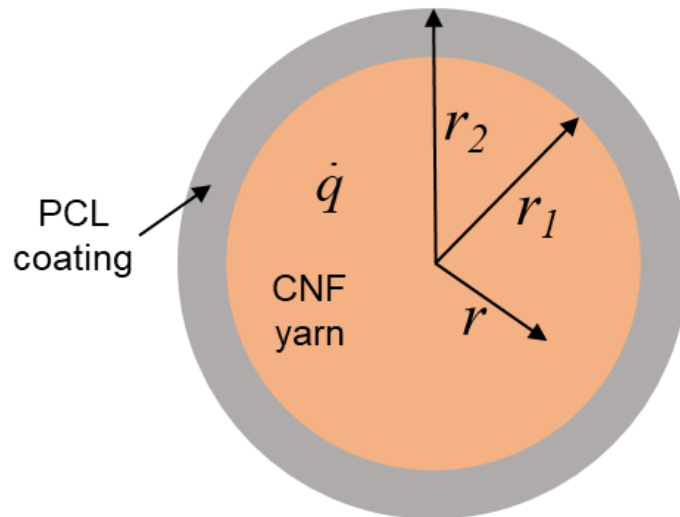
Figure 4.8 Schematic of CNF yarn

$$\frac{1}{r}\frac{d}{dr}(r\frac{dT_1}{dr})+\frac{\dot{q}}{k_1}=0 \quad (0 \le r < r_1)$$

(4.6)

$$\frac{1}{r}\frac{d}{dr}(r\frac{dT_2}{dr}) = 0 \qquad (r_1 \leq r < r_2) \tag{4.7}$$

where k_1 and k_2 are the thermal conductivity of the CNF yarn and the PCL coating,

$\dot{q} = \dfrac{P}{\pi r_1^2 l}$ is the heat generated per unit volume due to the applied power P in the yarn with

length l and radius of r_1.

The following boundary conditions are considered: at $r=0$, $\dfrac{dT_1}{dr} = 0$, this boundary

condition is applied to reflect the axisymmetric temperature distribution. At the $r = r_1$, the

heat flux is equal on both side of the interface, $k_1 \dfrac{dT_1}{dr} = k_2 \dfrac{dT_2}{dr}$ and the temperature is

continuous at the interface $T_1(r_1) = T_2(r_1)$. At $r = r_2$, the surface temperature of the yarn is

specified as $T_2(r_2) = T_s$. $T_s = T_\infty + \dfrac{P}{2\pi h r_2 l}$ can be then obtained by considering the

convection boundary condition: $h(2\pi r_2 l)(T_s - T_\infty) = P$, where h is the convection

coefficient and T_∞ is the environment temperature.

The solution to the above boundary value problem is:

$$T_1(r) = T_\infty + P\left(\frac{1}{2\rho l r_2 h} + \frac{1}{2\rho l k_2}\ln\frac{r_2}{r_1} + \frac{1}{4\rho l k_1}(1 - \frac{r^2}{r_1^2})\right) \tag{4.8}$$

$$T_2(r) = T_\infty + P\left(\frac{1}{2\rho l r_2 h} + \frac{1}{2\rho l k_2}\ln\frac{r_2}{r}\right) \tag{4.9}$$

The average temperature of the yarn and the coating is:

97

$$T_{core} = \frac{1}{r_1} \int_0^{r_1} T_1(r)\, dr = T_\infty + P\left(\frac{1}{2\rho l r_2 h} + \frac{1}{2\rho l k_2} \ln\frac{r_2}{r_1} + \frac{1}{6\rho l k_1} \right) \equiv T_\infty + cP \qquad (4.10)$$

$$T_{coating} = \frac{1}{r_2 - r_1} \int_{r_1}^{r_2} T_2(r)\, dr = T_\infty + P\left(\frac{1}{2\pi l r_2 h} + \frac{1}{2\pi l k_2} - \frac{r_1}{2\pi l k_2 (r_2 - r_1)} \ln\frac{r_2}{r_1} \right) \equiv T_\infty + \beta P \qquad (4.11)$$

As can be seen from the solution, the average temperature of the yarn and coating are both linear functions of P with factor χ and β which both depend on the sample geometry, thermal conductivity of the sample and convection coefficient. To determine χ experimentally, a CNF yarn was coated with PCL by the dip coating process mentioned in the previous section. Next, the sample was submerged in a water bath with a mechanical stir stirring at 500 rpm. The sample was heated with Joule heating, the yarn temperature was calculated with Equation (4.5) at varying power (calculated as $P = V \cdot I$) ranging from 0.5w to 1.5w. The results are shown in Figure 4.9a. As can be seen, the CNF yarn temperature reached steady state very quickly after applying the power and it went back to room temperature when the power was turned off. The temperature of yarn also showed good reversibility.
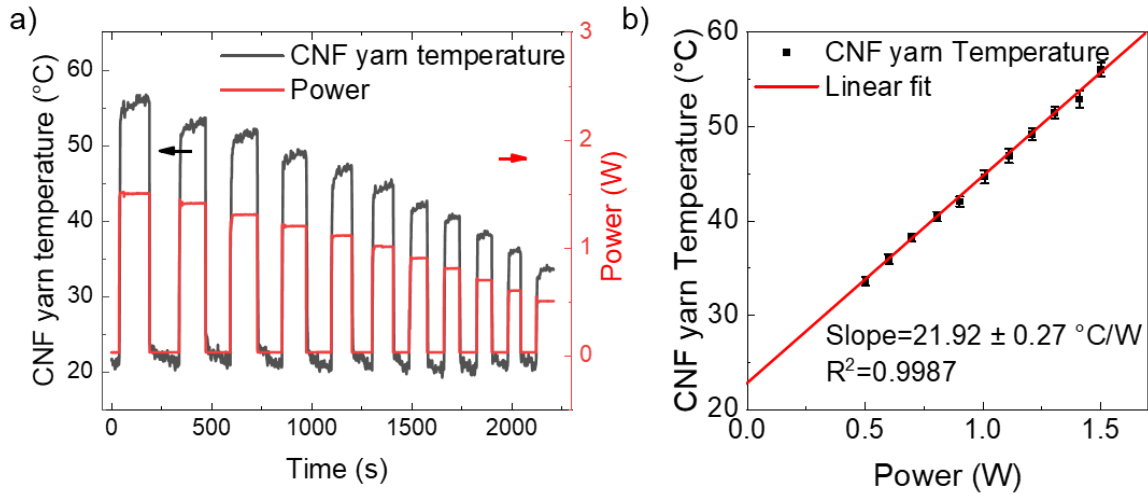
Figure 4.9 Temperature of CNF yarn at different applied power.

The temperature and power result is fitted with linear regression as shown in Figure 4.9b, χ in Equation (4.10) is equal to the slope of the T-P curve which is 21.92±0.27 °C/W. The convection coefficient can be calculated by the following equation using the calculated χ (refer to Equation (4.10)) and the yarn properties:

$$h = \frac{3k_1 k_2}{r_2\left(-k_2 + 6\pi k_1 k_2 \chi l - 3k_1 \ln\left(r_2 / r_1\right)\right)} \tag{4.12}$$

where r_1 and r_2 are the yarn radius before and after the PCL coating measured by optical microscope, $r_1 = 64.0 \pm 2.2$ μm and $r_2 = 69.0 \pm 1.8$ μm, $l = 2$cm, k_1 and k_2 are thermal conductivity of the CNF yarn and PCL coating, k_1 is estimated by the rule of mixture when the CNF yarn is filled with water: $k_1 = (1 - P_{yarn})k_{carbon} + P_{yarn}k_{water} = 3.54$ W/(m.K) where $k_{carbon} = 10.46$ W/(m.K) for PAN based carbon fiber and $k_{water} = 0.6$ W/(m.K), $k_2 = 0.18$ W/(m.K)[174]. As a result, the convection coefficient for this experiment condition is calculates to be 6460 ± 610 W/(m^2.K).

Factors that influence the convection coefficient include: the type of fluid flow (laminar or turbulence), fluid flow velocity, fluid properties, the surface roughness and the geometry of the object. Under the same the experimental condition (e.g. same mixer rpm, same relative position of the sample in the water bath), the fluid flow and fluid properties are constant. In addition, the geometry of the yarn and surface roughness of the coating are constant as the same processing condition were applied in different samples. Therefore, the convection coefficient is constant between different test and the temperature of the yarn and the coating can be calculated by Equation (4.10) and (4.11) using the convection coefficient obtained in this section.

4.3.4. Influence of molecular weight on the encapsulation

For the on-demand or active release, the loaded material should have very low release rate at deactivated state (ie., zero applied voltage or when the fiber is at room temperature) to minimize undesired release and a high release rate when it is activated. The purpose of the PCL coating is to suppress the release of the loaded material at room temperature. This will protect the loaded material from leaching out when the release is undesired. To evaluate the effectiveness of the PCL coating for this purpose, the release profile of GV with passive release of the GV loaded CNF yarns were studied at room temperature.

To this end, GV loaded CNF yarns was coated with PCL with two different molecular weight ($M_w\sim14000$ and 25000 g/mol). The passive release of GV at room temperature from these two samples are studied and the release profiles are shown in

Figure 4.10a. The release profiles for these two samples showed significant difference. For the yarn coated with low M_w PCL, 90.2% of the GV was released within 130 min. The yarn with high M_w PCL coat had a much lower release rate with only 10.0% release in 210 min. Optical images of the yarn after the release experiments are shown in Figure 4.10b,c, a crack was observed on the low M_w PCL coating along the entire length of the yarn whereas the high M_w coating is intact. The crack is the main reason for this large amount of undesired release of GV. The crack is likely formed due to the stress caused by the swelling of PCL in contact with water. The low M_w PCL has much lower mechanical properties compared to the high M_w PCL, it is noticeably weaker during the handling of the material, as received low M_w PCL can easily break into smaller pieces. Hence, the low M_w PCL is more prone to crack and is not suitable as the coating material. On the other hand, high M_w PCL serves the purpose of mediating the release of GV and is used for the rest of the study.
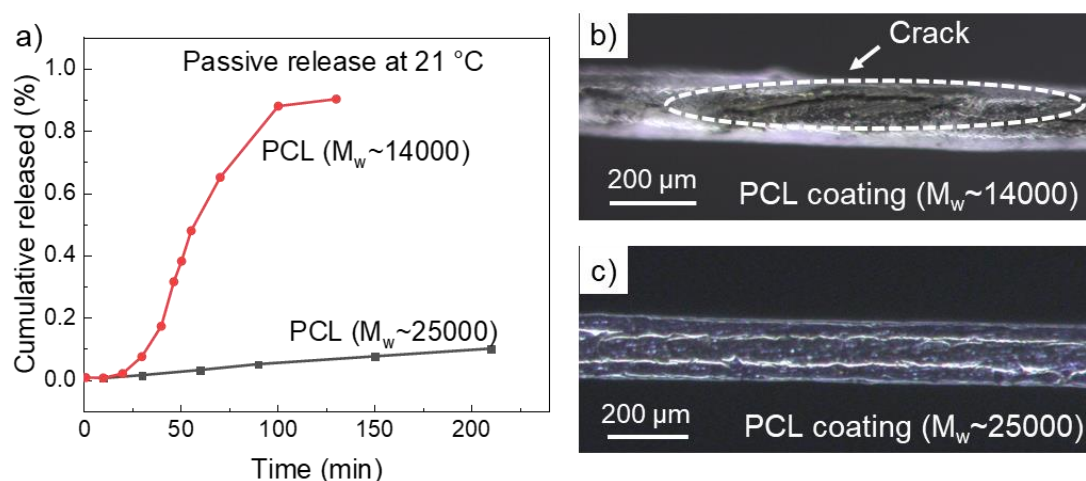
Figure 4.10 a) release profile of GV loaded CNF yarns with different PCL coating, b) and c) optical images of the yarn after the release test.

It is also worth noticing that the release kinetics changed when the crack is formed. The release profile with high M_w PCL followed linear relationship whereas in case of PCL coating with cracked formed, the release kinetics deviated from the linear relationship. This suggest different release mechanisms occurred in these two cases. The release mechanism will be discussed in detail in the next section.

4.3.5. Release mechanism of GV loaded CNF yarn

The release of GV from the yarn consists of three stages after submerging it in water. In the first stage, water penetrates into the yarn through the PCL coating and dissolve the loaded GV. Due to the high mass loading of GV in the yarn and limited solubility of GV in water (~50 mg/L), a saturated solution GV/water solution is quickly formed on the inner surface of the PCL coating and large portion of GV remained undissolved inside the yarn. In the second stage, the dissolved GV in the saturated solution partitions into the PCL coating and diffuse through the coating into the surrounding medium due to a concentration gradient. Since the diffusion of GV through PCL is much slower than the dissolution, the released GV in the saturated solution will be quickly replenished by the undissolved GV. Therefore, GV concentration inside the PCL coating stays constant at the saturation concentration. In the third stage, the solid phase is depleted and the concentration of the GV solution in the yarn start to decrease until all the GV is released.

Since the diffusion of GV (second stage) is much slower than the other two steps, the release rate is diffusion controlled. For this type of diffusion-controlled release

reservoir system, the model which describe the release is well studied by number of researchers[175-179]. During the second stage, the concentration gradient in the coating is nearly constant so the rate of GV flux is nearly constant. Therefore, the release of GV can be modeled as steady state diffusion and the cumulative mass of GV released is[175-178]:

$$M_t = \frac{2\rho l K C_s D}{\ln(r_2/r_1)}t \tag{4.13}$$

where l is the length of the yarn, D is the diffusion coefficient of GV in PCL, K is the partition coefficient of defined as the ratio of solubility of GV in the PCL to its solubility in the water, C_s is the saturation concentration in water, r_1 and r_2 are the radius of the yarn before and after the PCL coating and t is time of the release. In this stage, the cumulative amount of GV released increases linearly with time. In other words, the release rate is constant. This is also described as "zero-order release kinetics"[175].

During the third stage, due to the depletion of GV in the yarn, the concentration of GV in the yarn drop below saturation concentration. Unsteady state diffusion is thus used to model the release of GV, the cumulative amount of GV releases is[175]:

$$\frac{M_t}{M_\infty} = 1 - \exp\left[-\frac{(r_1 l + r_2 l + 2r_1 r_2)KD}{r_1^2 l(r_2 - r_1)}t\right] \tag{4.14}$$

where M_∞ is the total amount of GV in the system. During this stage, the release rate decays exponentially with time. Since the release rate is proportional to the concentration in the at the inner surface of the coating, this is described as "first order release kinetics".[175]

4.3.6. Active release of GV

The active release of GV from the GV loaded yarns is studied by applying different power (input voltage) to the yarn during the release test. The temperature distribution of the yarns are calculated using Equation (4.8) and (4.9) with the calibrated convection coefficient ($h = 6460 \pm 610$ W/(m^2.K)) and the parameters (P, r_1, r_2 and l) measured on different sample as shown in Table 4.2 (refer to Figure 4.8). Equation (4.8) and (4.9) are plotted using the above mention experimentally determined parameters as the temperature profiles as shown in Figure 4.11. Similarly, the average core temperature (T_{core}) and average coating temperature ($T_{coating}$) is calculated using Equation (4.10) and (4.11). The release profile is shown in Figure 4.12. Sample A3 after the active release was characterized using SEM as shown in Figure 4.13. Comparing with the SEM images (Figure 4.6) before the release, it is clear that the morphology of the coating is unchanged, no melting of the coating or cracks are observed. The GV absorbed in both macro pores and meso pores of the CNF yarn has been released.

Table 4.2 Parameters for active release experiments

Sample	Applied power (W)	r_1 (μm)	r_2 (μm)	T_{core} (°C)	$T_{coating}$ (°C)
Passive (A0)	0	64.1±2.3	69.0±1.8	21.0±0.1	21.0±0.1
A1	0.501±0.003	70.6±1.8	75.5±1.7	32.0±1.5	30.9±0.9
A2	1.040±0.014	68.6±2.7	73.5±2.6	43.4±2.1	41.0±1.2
A3	1.532±0.017	70.1±1.9	75.0±1.8	52.9±1.5	49.4±1.0
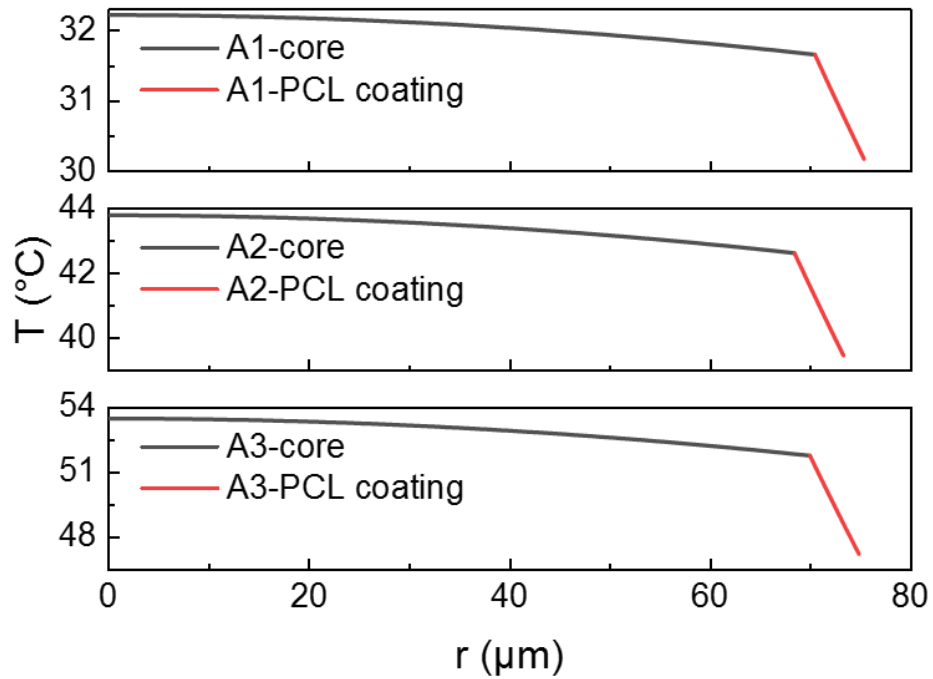
Figure 4.11 Radial temperature distribution of the active release sample calculated by the heat transfer model using experimentally calibrated parameters.
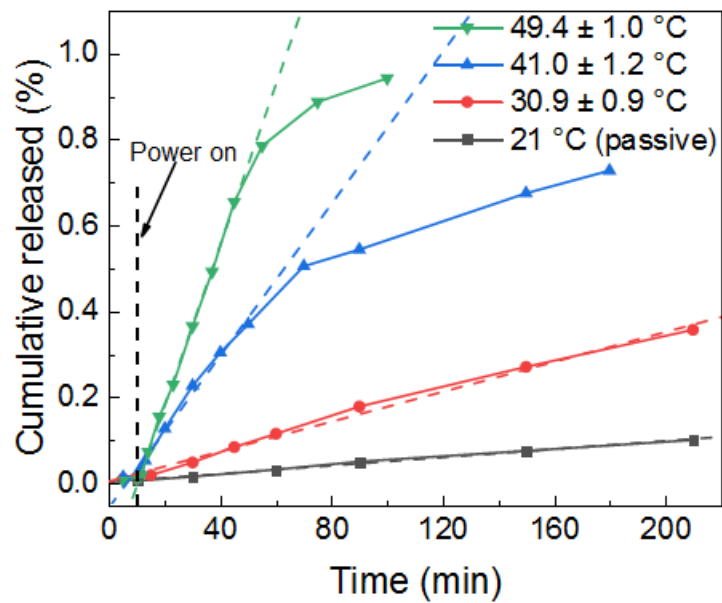
Figure 4.12 release profile of GV from passive and active release samples.

Table 4.3 Fitting parameter for linear region of release profiles

Sample	Slope	R^2	dM_t/dt (µg/min)
Passive	0.00048±0.00002	0.9946	0.078±0.003
A1	0.00174±0.00007	0.9919	0.282±0.011
A2	0.00883±0.00041	0.9915	1.432±0.066
A3	0.01867±0.00025	0.9991	3.028±0.041
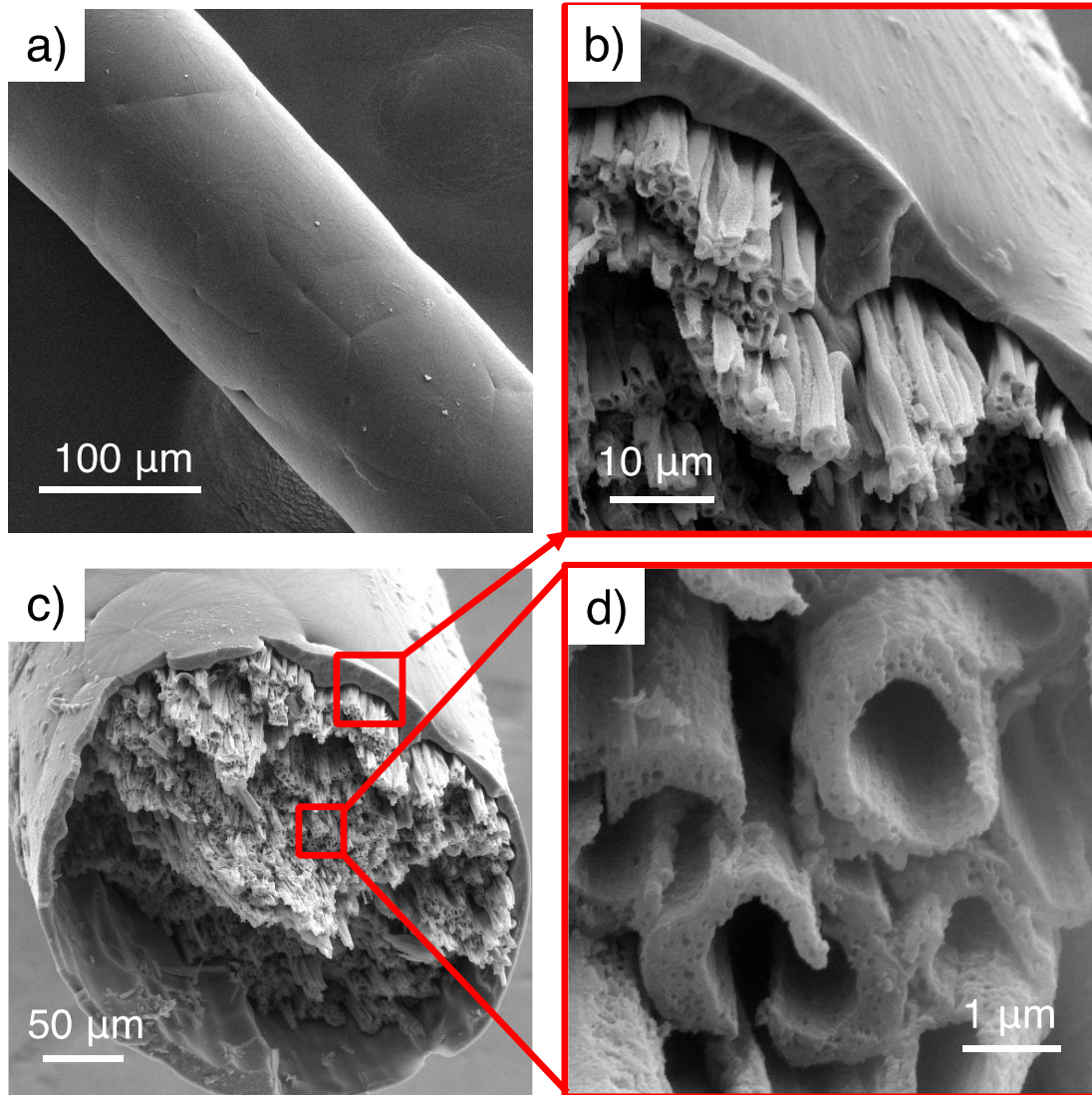
Figure 4.13 SEM images of the GV loaded CNF yarn (A3) after the active release experiment.

In the active release experiments, the power is turned on at t = 10min for all three samples. Within the first 10 min prior to turning the power on, all three samples showed very low release. For the active release at high temperature (41.0 and 49.4 °C), two regions can be observed on the release profiles: a linear region at lower cumulative release (<50%) and a non-linear region at higher cumulative release (>50%). This transition is expected which is due to the depletion of undissolved GV in the core as discussed in previous section. The linear portion of the release profiles are fitted with linear regression and the results are presented in Table 4.3. The release rate increased significantly with the temperature as shown in Figure 4.14a. From equation (4.13), the release rate in the linear release region can be estimated as:

$$\frac{dM_t}{dt} = \frac{2\rho l K C_s D}{\ln(r_2 / r_1)} \tag{4.15}$$

Factors that influence the release rate are the partition coefficient K, saturation concentration C_s and diffusion coefficient D. Among these factors, K and C_s for organic compound are mainly determined by the molecular structure and their change with respect to temperature will be neglected. Therefore, the release rate is mainly affected by the diffusion coefficient. The relationship of D and temperature is be described by the Arrhenius equation:

$$D = D_0 \exp\left(-\frac{Q_d}{RT}\right) \tag{4.16}$$

where D_0 is a temperature-independent preexponential (m²/s), Q_d is the activation energy for diffusion (J/mol), R is the gas constant 8.31 J/(mol.K) and T is the absolute temperature (K). Combining Equation **(4.15)**, **(4.16)**:

$$\ln\left(\frac{dM_t}{dt}\frac{\ln(r_2/r_1)}{l}\right) = \ln\left(2\rho KC_sD_0\right) - \frac{Q_d}{RT} \tag{4.17}$$

a)

b)
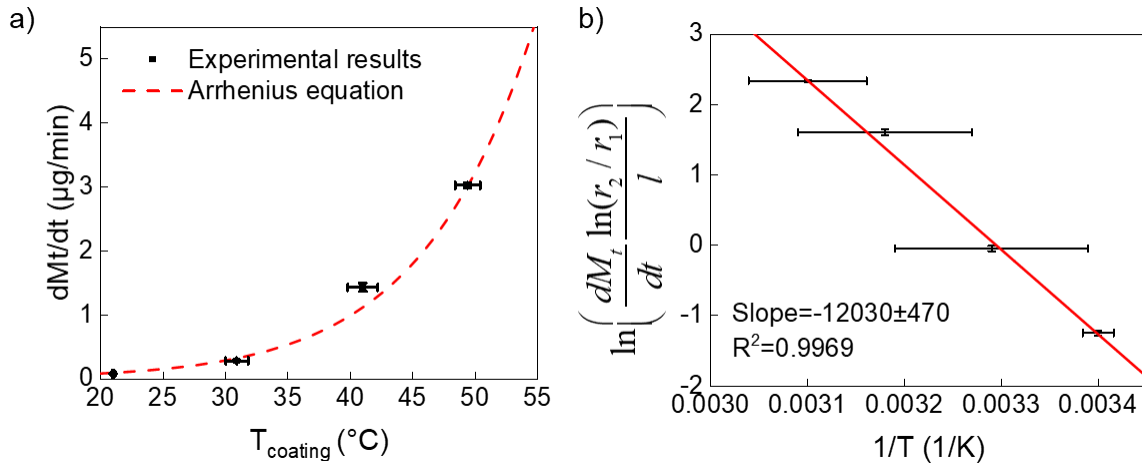
Figure 4.14 a) Release rate at different coating temperature, b) calculation of activation energy through Arrhenius equation, unit for the slope is (K.µg/(m.min))

The release rate from the four experiments are fitted using Equation **(4.17)** as shown in Figure 4.14b. The activation energy for diffusion of GV diffusion in PCL can be calculated with the slope and the result is 100.0 ± 3.9 kJ/mol. This result lies within the range of activation energy for diffusion of different species in PCL[180] and other polymers[181]. Using the Activation energy, the release rate at an unknown temperature can be easily estimated as shown by the dotted curve in Figure 4.14a.

4.4. Conclusion

In this chapter, we have successfully demonstrated the encapsulation and active release of functional material using porous CNFs as the host. Porous CNF yarns with average diameter of 154.9 ± 8.9 µm was first made by twisting the precursor fibers, followed by carbonization. The hierarchical porous structure of yarns was analyzed using

SEM. The functional material, GV, was loaded into the porous CNFs yarns through a carrier solvent and a remarkable mass loading of 47.4 ± 5.4 % was achieved. The method to encapsulate the yarn through dip coating PCL was also explored. A high molecular weight (25,000 g/mol) PCL is required to effectively encapsulate the functional material and prevent undesired release. The method to accurately determine the temperature of the yarns during the active release was analyzed utilizing the temperature-resistance relationship of CNFs and a heat transfer model. Active release of the functional material was achieved by heating up the yarn with Joule heating, which increased the permeability of the coating and facilitated the diffusion of the functional material through the PCL coating. The release profile was analyzed at different heating level. The results showed that the release rate can be very well controlled by the applied power. A ~39x increase in release rate was achieved by heated up the coating from room temperature to 49.4±1.0 °C. The change in release rate at different temperature followed the Arrhenius equation very well, and the activation energy for diffusion of GV in PCL was calculated to be 100.0 ± 3.9 kJ/mol from the release rate at different temperature which lies within the range of activation energy for diffusion of different species in polymers.

5. STRUCTURAL ENERGY STORAGE IN POROUS CNFS[*]

Structural energy storage materials refer to a broad category of multifunctional materials which can simultaneously provide load-bearing and energy storage to achieve weight reduction in weight-sensitive applications. This is an emerging field which has evolved out of the need for onboard energy sources in weight and volume sensitive applications, such as electric propulsion airplanes and electric cars. As previously discussed in Section 1.4, reliable and satisfactory performance in each function, load bearing or energy storage, requires peculiar material design with potential trade-offs between them. The porous CNFs showed high specific surface area and mechanical properties as presented in Section 2.3, this makes them good candidate for structural energy storage application. However, the trade-off between the energy storage and loading bearing in these porous CNFs is still unexplored.

In this chapter, the trade-offs between functionalities in an emerging class of nanomaterials, CNFs is unraveled. First, we will present our results on the effect of activation conditions on the morphology and microstructure of porous CNFs. Next, we will analyze the supercapacitor performance of porous CNFs as a function of activation conditions. In addition, we will present the experimental result of the mechanical properties of different porous CNFs, the mechanism of the reduction in mechanical

properties is analyzed. Finally, we will analyze the trade-off between energy storage and load-bearing capabilities of porous CNFs with multifunctional efficiency.

5.1. Experimental method

5.1.1. Activation of porous carbon nanofibers

The porous CNFs were fabricated following the method presented in Section 2.3 using PAN:PMMA ratio of 1:1. In order to further increase the SSA for the porous CNFs, they were activated using KOH. For this purpose, as prepared porous CNF ribbons were then soaked in KOH aqueous solution with concentration ranging from 1 M to 4 M for 3 hrs at room temperature, the ribbons were then taken out of the solution and dried in vacuum oven at 80 °C for 3 hrs. After drying, the ribbons were thermally treated in nitrogen atmosphere at 800 °C or 1000 °C for 30 min in a tube furnace. The activated porous CNF ribbons were washed with deionized water and dried in vacuum oven at 80 °C for 3 hrs.

5.1.2. Material characterization of activated porous carbon nanofibers

SEM images of the porous CNFs were obtained by FEI Quanta 600 FE-SEM at 20 kV. The cross-section of the porous CNFs was exposed by fracturing with a razor blade. To prepare the TEM samples, the porous CNFs were dispersed in water by bath ultrasonication for 5 mins, the porous CNF dispersion was then dropped on to TEM grid and dried at 80 °C for 30 min. TEM images of the porous CNFs were acquired with JEOL JEM-2010 TEM at 200 kV. N_2 adsorption isotherms were obtained at 77K with

Quantachrome Autosorb iQ. Porous CNFs were degassed at 250 °C for 4 hrs under vacuum before test. The Raman spectra were acquired with a Horiba Jobin-Yvon LabRam Raman confocal microscope using He−Ne laser (633 nm). The XPS spectra were acquired by an Omicron XPS/UPS system with Al X-ray source. To increase the stability of system, a CN10 charge neutralizer installed on this XPS system is used to minimize charging on samples. The porous CNFs were attached to the sample holder using double-side copper tape.

5.1.3. Mechanical characterization of activated porous carbon nanofibers

The mechanical properties of the porous CNFs were measured by single fiber tensile test using the method presented in Section 2.3.1.

5.1.4. Electrochemical characterization of activated porous carbon nanofibers

The capacitance of the porous CNF electrode is characterized by using a symmetric two-electrode cell set up. 6 M KOH aqueous solution was used at electrolyte. The specific capacitance of the working electrode is evaluated by cyclic voltammetry and constant current charge discharge technique using CH Instrument 700B Bipotentiostat. In cyclic voltammetry, the specific capacitance is calculated as $C_{\text{specific}} = 2 \cdot \dfrac{1}{2k \cdot m \cdot \Delta V} \oint IdV$, where I is the current, k is the scan rate (V/s), m is the weight of a single porous CNF electrode and ΔV is the scanning potential window. In constant current charge discharge test the specific capacitance is calculated as $C_{\text{specific}} = 2 \dfrac{I \cdot \Delta t}{m \cdot \Delta V}$, where I is the discharge current,

Δt is the discharge time, m is the weight of a single porous CNF electrode and ΔV is the discharge potential window. The current density is calculated as I/m.[182, 183]

5.2. Results and discussion

5.2.1. Morphology and structure of KOH-activated porous CNFs

The porous CNFs were fabricated by coaxial electrospinning of PAN/PMMA emulsion in the shell and PMMA in the core, followed by thermal stabilization at 270 °C for 2hrs and carbonization at 1100 °C for 60 min. The core of the precursor was entirely composed of PMMA, while the skin was composed of the PAN/PMMA emulsion. As shown in the previous sections, the PMMA in the PAN/PMMA emulsions forms islands in a continuous PAN phase in the precursor fibers. During the carbonization process at 1100 °C, the PMMA in the core and the islands of the PMMA in the shell were decomposed into gaseous phase and left behind the hollow core and porous skin.[49] The pristine porous CNFs were then activated with KOH to increase the surface area. The mass ratio of KOH to carbon and activation temperature significantly influenced the activation of carbon materials.[87, 184] Previous studies showed that the BET surface area of KOH-activated carbon material increases with the KOH/carbon mass ratio[75, 77, 184] and activation temperature up to 1000 °C.[87] In this study, KOH was introduced into the porous CNF mat by soaking the mat in the KOH solution. KOH solution concentrations of 1 M, 2 M and 4 M and the activation temperatures of 800 °C and 1000 °C were selected. The samples were labeled according to the activation conditions, i.e. KOH concentration and activation temperature.
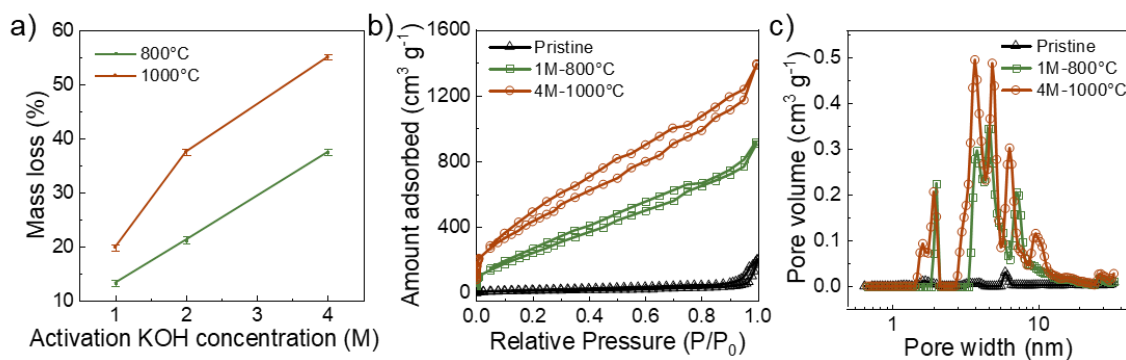
Figure 5.1. a) Mass loss ratio after KOH activation for different activation conditions, error bars represent the uncertainty of the electrode weight measurement, b) N2 adsorption isotherm and c) pore size distribution for pristine, 1M-800 °C and 4M-1000 °C porous CNFs. Reprinted from [72] with permission.

KOH activation both at higher temperature and higher KOH concentration increased the relative mass loss as shown in **Figure 5.1**. The activated porous CNFs with the lowest (1M-800 °C) and highest (4M-1000 °C) mass loss ratio were selected for further studies to reveal the effect of activation on the mechanical and electrochemical performance of porous CNFs structure.

Nitrogen adsorption isotherms of pristine, 1M-800 °C and 4M-1000 °C porous CNFs are shown in Figure 5.1b. The surface area was calculated with the Brunauer–Emmett–Teller (BET) theory. The BET surface area and total pore volume both increased significantly after the KOH activation as shown in Figure 5.1b & c and **Table 5.1**. The increased BET surface area (20 to 30 times) is a result of the partial etching of the porous CNFs during the KOH activation which leaves micro and meso pores.[184] The pore size distribution was calculated by Quenched Solid State Functional Theory (QSDFT) method as shown in Figure 5.1c. The pore size distribution showed a similar trend for both

activated samples. In the micropore region (< 2 nm), a peak at 2nm appeared for both 1M-800 °C and 4M-1000 °C activation. However, a different peak appeared at 1.5-1.8 nm in this range of pore width after 4M-1000 °C activation, indicating the generation of more micropores with more severe activation condition. In the mesopore region (2~50 nm), 1M-800 °C and 4M-1000 °C both showed similar peaks at 2-5 nm. The peak for 4M-1000 °C was slightly broader in smaller pore width region. Another peak appeared at 7 nm for 1M-800 °C sample, similar peak was also observed in 4M-1000 °C sample but it was shifted to 6.4 nm. In addition, a new peak was observed at 10 nm only after 4M-1000 °C activation, suggesting the generation of some large mesopores due to the more severe activation (the walls between some pores are likely removed, appearing as peaks corresponding to larger pores). The total pore volume of micropores and mesopores increased more than 4x after 1M-800 °C activation (compared to un-activated CNFs) and increased further by another ~50% with 4M-1000 °C activation. The average pore diameter decreased from 23.83 nm in pristine CNFs to 5.3 nm for 1M-800 °C activation and 4.91nm for 4M-1000 °C activation due to the generation of new micro and meso pores.

Table 5.1. Nitrogen adsorption results of porous CNFs. Reprinted from [72] with permission.

	BET surface area (m²/g)	Average pore diameter (nm)	Total pore volume (cm³/g)
Pristine	52.3	23.82	0.31
1M-800 °C	1059.0	5.30	1.40
4M-1000 °C	1753.9	4.91	2.15

The activated porous CNF mat and the electrode are flexible and showed good structural integrity as shown in **Figure 5.2**a-b. To understand the effect of the KOH activation on the morphology of the porous CNFs, the microstructure of pristine porous CNFs and activated porous CNFs (1M-800 °C and 4M-1000 °C) were studied using field emission scanning electron microscope (FE-SEM), transmission electron microscope (TEM), Raman spectroscopy, and X-ray photoelectron spectroscopy (XPS). The average diameter and shell thickness measured from SEM images (with 30 samples per case) are shown in Figure 5.2d. The average diameter for pristine, 1M-800 °C and 4M-1000 °C porous CNFs was 2.13±0.40 μm, 1.75±0.35 μm and 1.46±0.32 μm, respectively, and their average shell thickness were 0.31±0.06 μm, 0.31±0.06 μm and 0.28±0.06 μm, respectively. The porous CNF diameter decreased after the activation by ~17.8 % after activation at 1M-800 °C and 31.5 % after activation at 4M-1000 °C. However, the shell thickness experienced much smaller changes after activation. The average shell thickness remained nearly the same after 1M-800 °C activation and decreased by 11.2 % after 4M-1000 °C activation. This result suggests the inner and outer diameter shrank at comparable rates. With the reduction in diameter, the average cross-section area for the porous CNFs decreased by 19% for 1M-800 °C and 40% for 4M-1000 °C activation. Due to the nature of electrospinning, the CNF diameter and shell thickness measurements had considerable variations. However, qualitatively, the reduction in cross-section area was relatively close to the mass loss (13.2% for 1M-800 °C and 55.0% for 4M-1000 °C). This is expected, since the main mechanism for the reduction in the cross-section area is the removal of the material from the boundaries of the pores.

116

Surface morphology of the porous CNFs also changed during the activation. The surface of the pristine porous CNFs is relatively smooth with very few surface pores on the CNF surfaces, Figure 5.2e. Surface morphology of the porous CNFs changes significantly during the activation. After the KOH activation, the number of surface pores noticeably increased, Figure 5.2j & o. The images of the cross section of the CNFs revealed further differences between activated and pristine (no activation) CNFs. On the cross-section of the pristine CNFs, mesopores with nearly circular and regular shapes were observed. These mesopores were formed due to the decomposition of PMMA islands in the emulsion during the carbonization process.[49] The mesopores were separate from each other since they originated mostly from disconnected PMMA islands in the emulsion. As seen from the SEM images, the mesopores in the porous CNFs were a mixture of open and closed pores. There is a higher probability for the mesopores near a free surface (i.e. the outer and inner surface of the shell) to be connected to the surface pores. The mesopores maintained their size and shapes with smooth boundaries after mild activation in the 1M-800 °C sample (13.2 % mass loss) as shown in Figure 5.2k & m (marked by yellow circles). However, a higher portion of mesopores became open due to higher density of surface pores which were observed on the surface. As the activation condition became more severe in the 4M-1000 °C sample, higher mass of the CNFs was removed (55.0 % mass loss). The mesopores were thus enlarged and became more irregular in shape due to inhomogeneous microstructure which favors inhomogeneous etching, Figure 5.2p & r (marked by yellow circles). This can in principle lead to partial removal of the walls between pores and the merger of smaller pores into larger ones. This coalescence could

117

be one of the reasons for the new peak which appeared at ~10 nm in the pore size distribution for 4M-1000 °C (Figure 5.1c).

In addition to the change of pore structure, KOH activation also affected the interlayer spacing of graphitic turbostratic domains, the interlayer spacing (measured from TEM images from five samples in each case) increased from 0.379±0.008 nm to 0.494±0.005 nm for the highly activated 4M-1000 °C sample as shown in Figure 5.2i, n & s. This result is in line with result from the literature[87]. The increase in the interlayer spacing is a results of intercalation of the reduced potassium during the KOH activation.[87, 184] During the KOH activation, the potassium (K) in KOH is reduced to metallic K at high temperature, which intercalate into the carbon lattices therefore expanding the interlayer spacing. After the activation, K is washed away by soaking the CNFs in water, as confirmed by XPS data (no K_2p peaks were detected in XPS spectra), the expanded carbon lattices cannot return to their original structural thus the higher interlayer spacing was remained.[184]
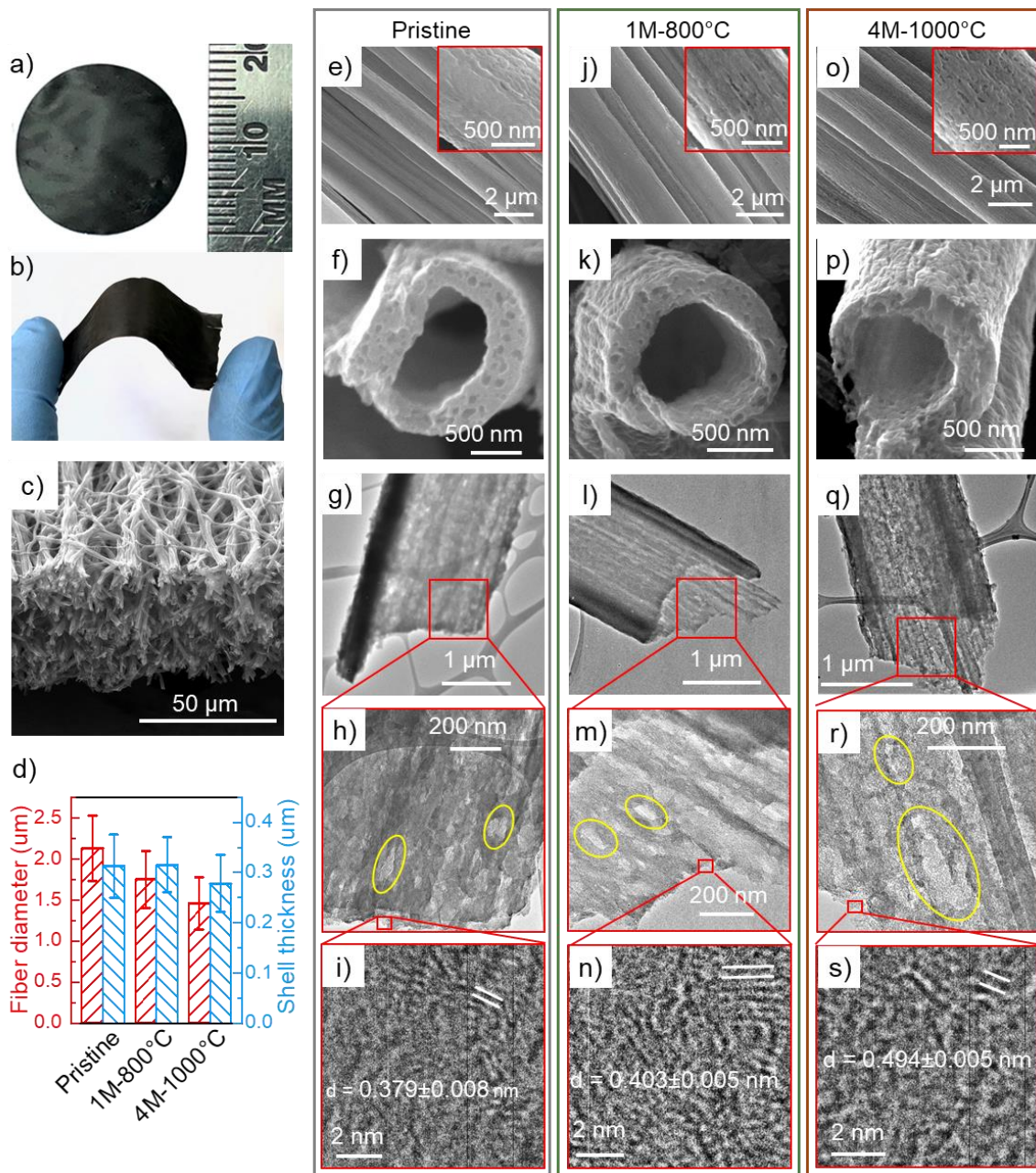
Figure 5.2. a) porous CNF electrode, b) bending of the activated porous CNF mat showing good structural integrity, c) SEM image of the cross-section of the activated porous CNF mat, d) fiber diameter and shell thickness for pristine, 1M-800 °C and 4M-1000 °C porous CNFs, surface morphology of e) pristine, j) 1M-800 °C and o) 4M-1000 °C porous CNFs, cross-sectional SEM images of f) pristine, k) 1M-800 °C and p) 4M-1000 °C porous CNFs and TEM images with different magnification of g), h), i) pristine, l), m), n) 1M-800 °C and q), r), s) 4M-1000 °C porous CNFs. Reprinted from [72] with permission.
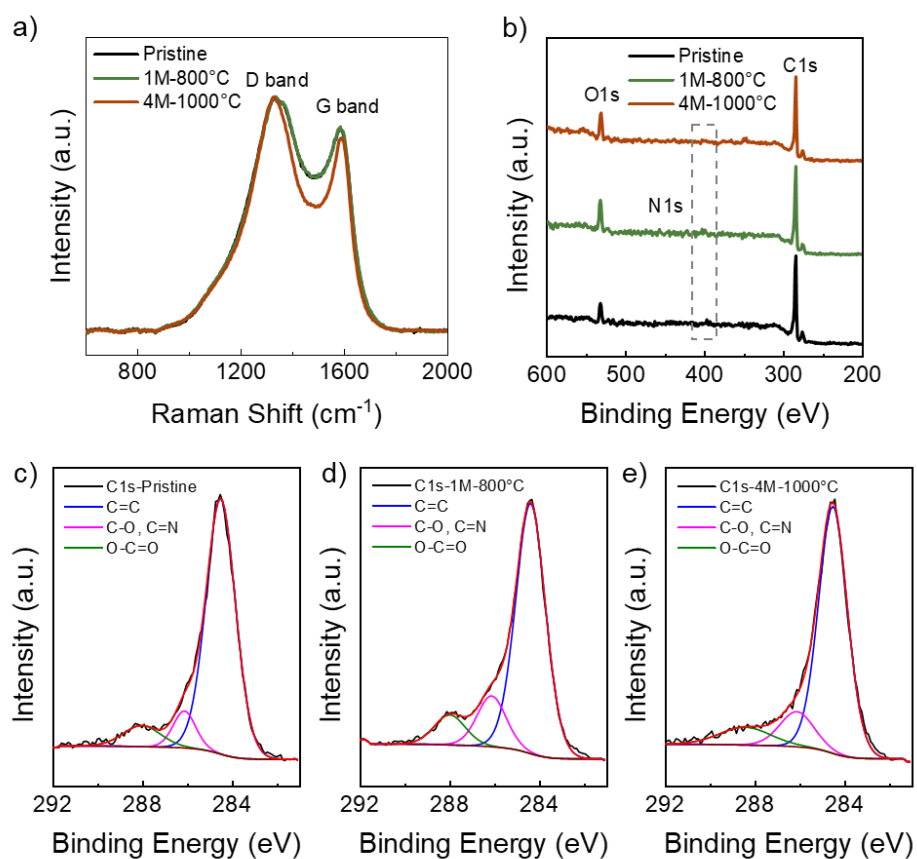
Figure 5.3. a) Raman spectra of pristine, 1M-800 °C and 4M-1000 °C porous CNFs, the pristine and 1M-800 °C spectra are overlapped, b) XPS spectra of pristine, 1M-800 °C and 4M-1000 °C porous CNFs, C1s peak of c) pristine, d) 1M-800 °C and e) 4M-1000 °C porous CNFs. Reprinted from [72] with permission.

Table 5.2. Chemical composition of porous CNFs. Reprinted from [72] with permission.

sample	I_D/I_G	C (at %)	N (at %)	O (at %)	C1s		
					C-O, C=N (%)	C=C (%)	O-C=O (%)
pristine	1.163±0.010	90.1	1.7	8.2	8.7	82.0	9.2
1M-800 °C	1.150±0.027	84.5	1.9	13.6	15.0	75.5	9.5
4M-1000 °C	1.211±0.012	84.4	0.7	14.9	13.0	77.1	9.9

Raman spectra of pristine, 1M-800 °C and 4M-1000 °C treated porous CNFs are presented in **Figure 5.3**a. Raman spectra were collected at four different spots on each sample, and the spectra were normalized and averaged to reduce noise. All three samples had two peaks at ~1336 and ~1580 cm^{-1}, which correspond to the disorder (D) band and the graphitic (G) band, respectively. The intensity ratio of D and G bands (I_D/I_G) is an indication of the level of structural disorder in carbon materials.[144] The average I_D/I_G is 1.163±0.010, 1.150±0.027 and 1.211±0.012 for pristine, 1M-800 °C and 4M-1000 °C, respectively. The Raman data points to sp^3 C atoms as defects, which can be in the form of both the functional groups on the surface (with -N or -O) and C-C. The latter mainly reflects the formation of the turbostratic domains that grow in the material during carbonization. The I_D/I_G for activated CNFs are very close to pristine CNFs, suggesting no relative loss in the graphitic structure of the CNFs as a result of the activation. Similar result was also reported in literature[90].

The surface chemical composition of the pristine and KOH-activated porous CNFs was analyzed by XPS, as shown in Figure 5.3b-e. Strong C 1s, O 1s and a weak N 1s peaks were presented in all the survey scans (Figure 5.3b). The chemical composition for pristine and activated porous CNF is shown in **Table** 5.2. The oxygen content increased from 8.2 at% in the pristine sample to 13.6 at% in the 1M-800 °C sample and increased further to 14.9 at% in the 4M-1000 °C. The deconvoluted C 1s spectra for three samples are shown in Figure 5.3c-e. Three peaks were presented in the deconvoluted spectra, the peak at 284.5 eV represents graphitic carbon, the peak at 286.1-286.3 eV represents C-O and C=N groups and the peak at ~288.5 eV represents O-C=O group.[185] The percentage of different

groups (as shown in **Table** 5.2) was calculated as the relative area under the deconvoluted peaks. As seen from the result, the percentage of O-C=O group showed a slight increase after the activation, whereas the percentage of C-O and C=N group showed a more significant increase. Since the nitrogen content did not increase after the activation, it is safe to assume that the percentage of C=N group did not increase. Consequently, the increase in C-O and C=N percentage is mainly due to the added C-O groups on the surface of CNFs. Moreover, since the increase in O-C=O percentage is very small, the added C-O group should account for most of the measured increase in the overall oxygen content after activation. Similar results on the increase of C-O content after KOH activation were also reported by other researchers.[90, 186] The Raman data does not suggest a major change in the D/G peak and defect density as a result of etching, suggesting that the functional groups grow on the boundaries of the graphitic domains where sp^3 hybridized C atoms are present. The reactions between KOH and carbon is summarized in Table 5.3. Moreover, as a result of the higher content of oxygen containing groups, the porous CNFs mat and the electrode became more hydrophilic after KOH activation, possessing higher wettability in aqueous electrolyte.

Table 5.3 Reaction between KOH and carbon at different temperature[184]. Reprinted from [184] with permission.

Reaction	Temperature
$6KOH + 2C$ (in CNFs) $\rightarrow 2K + 3H_2 + 2K_2CO_3$	400-600 °C
$K_2CO_3 \rightarrow K_2O + CO_2$	> 700 °C
$CO_2 + C$ (in CNFs) $\rightarrow 2CO$	> 700 °C
$K_2CO_3 + 2C \rightarrow 2K + 3CO$	> 700 °C
$C + K_2O \rightarrow 2K + CO$	> 700 °C

5.2.2. Electrochemical performance of KOH-activated porous CNFs

To evaluate the energy storage capability of the activated porous CNFs, the electrochemical performance of the samples was studied by cyclic voltammetry (CV) and galvanostatic charge/discharge in a symmetric two electrode system using 6 M KOH aqueous solution as electrolyte. The porous CNF electrodes are binder free and were used as-is after the KOH activation. The CV curves were obtained at various scan rates of 2 mV/s to 100 mV/s for different activation conditions (Figure 5.4 and Table 5.4). The CV curves for 1M-800 °C and 4M-1000 °C porous CNFs (**Figure 5.5**a) were nearly rectangular, indicating a capacitive behavior due to electrostatic double layer.[77]

Table 5.4 Specific capacitance of different porous CNFs. Reprinted from [72] with permission.

Scan rate (mV/s)	Specific capacitance (F/g)						
	Pristine	1M-800°C	2M-800°C	4M-800°C	1M-1000°C	2M-1000°C	4M-1000°C
100	16.5	105.7	117.3	130.5	100.7	130.5	149.8
75	17.8	108.3	120.6	133.8	103.1	133.5	154.8
50	19.5	109.7	124.3	139.8	106.5	137.5	159.8
25	22.7	116.8	130.7	147.8	111.9	142.5	167.0
10	27.3	123.8	137.9	154.6	119.0	149.6	175.5
5	31.0	129.3	142.8	160.8	124.3	155.2	181.9
2	36.3	138.2	147.6	168.7	131.2	163.2	191.3
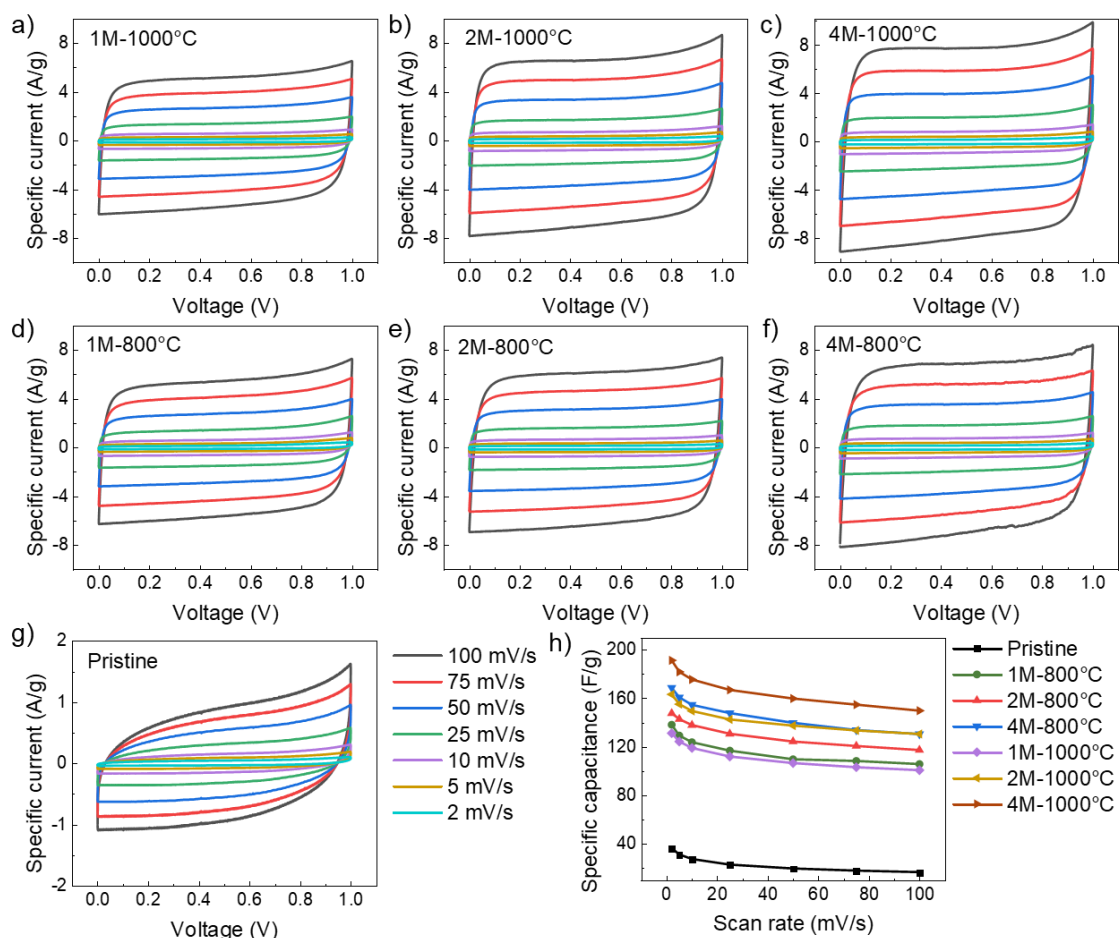
Figure 5.4 CV curves at different scanning rate of a) 1M-1000 °C, b) 2M-1000 °C, c) 4M-1000 °C, d) 1M-800 °C, e) 1M-800 °C, f) 4M-800 °C and g) pristine porous CNFs, h) specific capacitance of different porous CNFs vs scan rate. Reprinted from [72] with permission.

The specific capacitance decreased with increasing scan rate as shown in Figure 5.4h and Figure 5.5b. The highest specific capacitance (in each case obtained at 2 mV/s) was 36.4 F/g, 138.2 F/g and 191.3 F/g for pristine, 1M-800 °C and 4M-1000 °C porous CNFs, respectively. It is well established that the specific capacitance of carbon-based supercapacitors is dependent on the BET surface area and the content of C-O type oxygen groups. The specific capacitance scales linearly with the BET surface area and C-O

content enhance the capacitance.[90, 186] The significant improvement of specific capacitance after activation can be attributed to both increased BET surface area and the C-O content. Since all the activated samples had comparable contents of the functional groups, the enhancement of capacitance for the 4M-1000 °C sample should mainly have come from the increase in specific surface area.
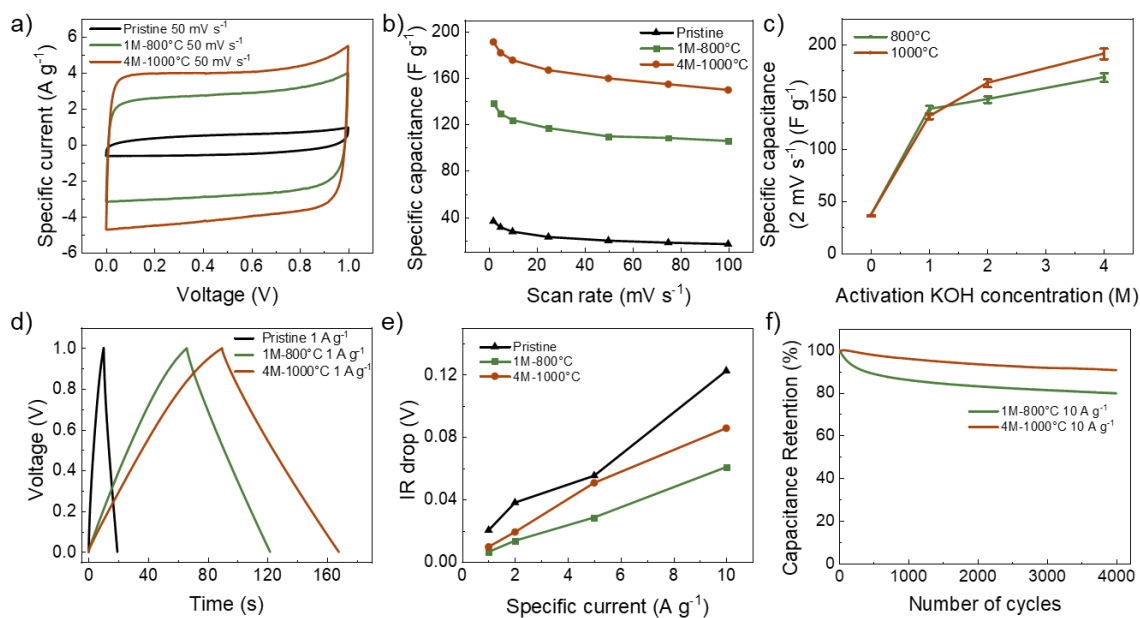
Figure 5.5. a) CV curves of pristine, 1M-800 °C and 4M-1000 °C porous CNFs with a scan rate of 50 mV/s, b) specific capacitance of pristine, 1M-800 °C and 4M-1000 °C porous CNFs at different scan rate, c) specific capacitance for different activation condition with a scan rate of 2 mV/s, error bars represent the uncertainty of the electrode weight measurement, d) galvanostatic charge/discharge curves for pristine, 1M-800 °C and 4M-1000 °C porous CNFs with a current density of 1A/g, e) IR drop (voltage drop due to the equivalent series resistance) for pristine, 1M-800 °C and 4M-1000 °C porous CNFs with different current density and f) capacitance retention of 1M-800 °C and 4M-1000 °C porous CNFs after 4000 cycles. Reprinted from [72] with permission.

The KOH-activated porous CNFs showed good rate capability at high scan rate, the specific capacitance retained 76.5% and 78.3% when the scan rate is increased to 100 mV/s. This is due to the wide pore size distribution from both mesopores and micropores

where the mesopores act as pathways for ion diffusion which helps the porous CNFs to maintain high capacitance at high scan rate.[89, 187] The specific capacitance evaluated at 2 mV/s for different activation conditions is shown in Figure 5.5c. The specific energy is calculated by $E = \dfrac{C \cdot V^2}{8 \cdot 3.6}$ and specific power is calculated by $P = \dfrac{E}{V / k} \cdot 3600$, where C is the specific capacitance in F/g, E is specific energy in Wh/kg, V is the voltage scanning window in V, k is the scaning rate in V/s and P is the specific power in W/kg. The specific capacitance and specific energy (Figure 5.6) both increased with higher activation KOH concentration and activation temperature, and the highest capacitance was reached with 4M-1000 °C activation.
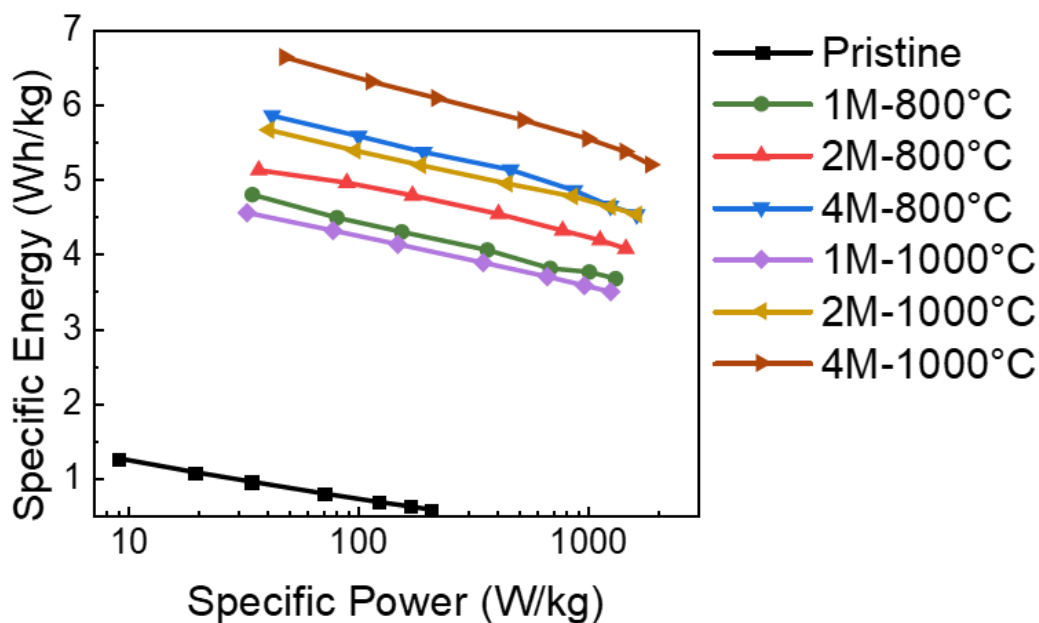
Figure 5.6 Ragone plot for 1M-1000 °C, 2M-1000 °C, 4M-1000 °C, 1M-800 °C, 1M-800 °C, 4M-800 °C and pristine porous CNFs. Reprinted from [72] with permission.

126

The capacitive behavior was confirmed by the linear galvanostatic charge/discharge (CD) curves as shown in Figure 5.5d and Figure 5.7. The specific capacitance at current density of 1A/g for pristine, 1M-800 °C and 4M-1000 °C porous CNFs was 18.5 F/g, 122.8 F/g and 158.0 F/g respectively. The voltage drop (IR drop) at the onset of the discharge curve at different current densities is shown in Figure 5.5e and Figure S3h in Supporting Information. The IR drop is small in all cases, suggesting that the test cells have very low equivalent series resistance (ESR). The KOH-activated porous CNFs showed lower IR drop compared to the pristine porous CNFs, which can be attributed to the improved hydrophilicity for the activated porous CNFs as discussed earlier.
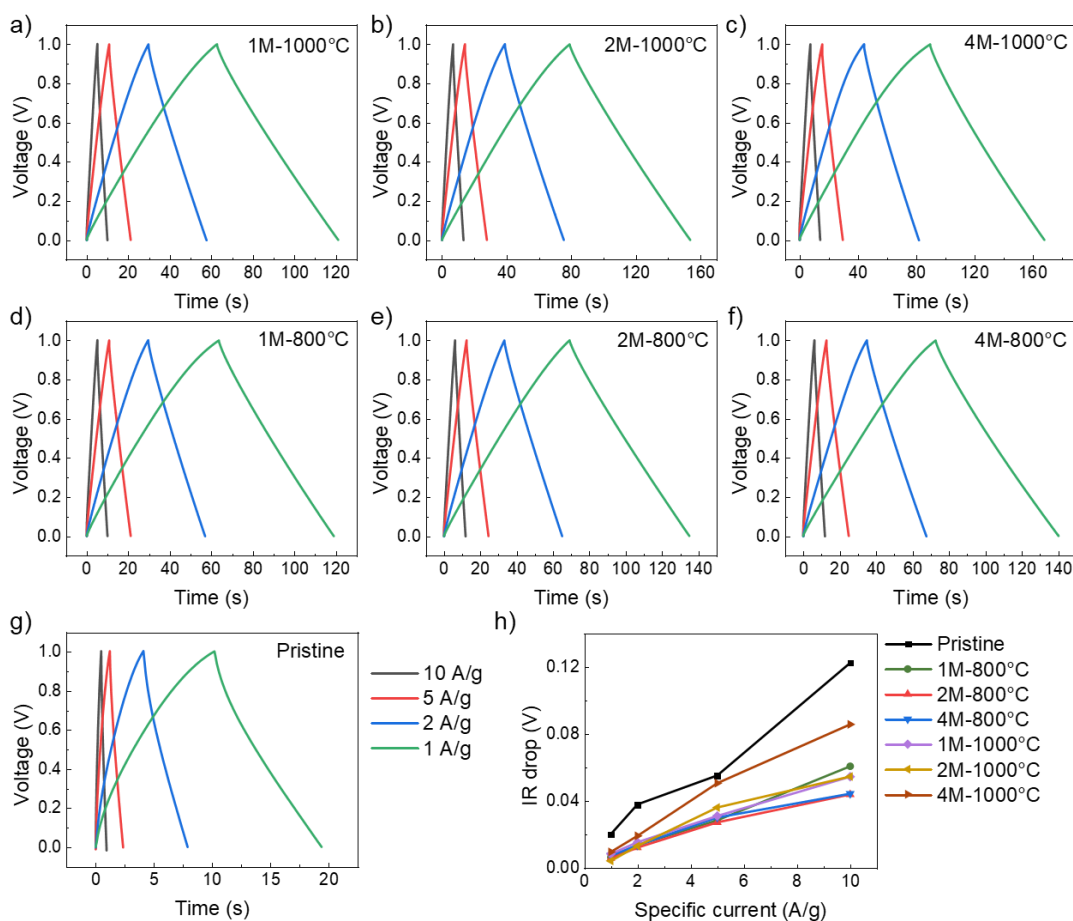
Figure 5.7 Galvanostatic charge/discharge curves at different current density of a) 1M-1000 °C, b) 2M-1000 °C, c) 4M-1000 °C, d) 1M-800 °C, e) 1M-800 °C, f) 4M-800 °C and g) pristine porous CNFs, h) IR drop for different porous CNFs vs specific current. Reprinted from [72] with permission.

The cycling stability of activated porous CNFs was investigated by galvanostatic charge/discharge for up to 4000 cycles. The results suggest that the activated porous CNFs have promising cycling stability, as shown in Figure 5.5f. The 1M-800 °C porous CNFs maintained 80% of the initial capacitance after 4000 cycles at 10 A/g, whereas the 4M-1000 °C porous CNFs retained 91% under the same test condition.
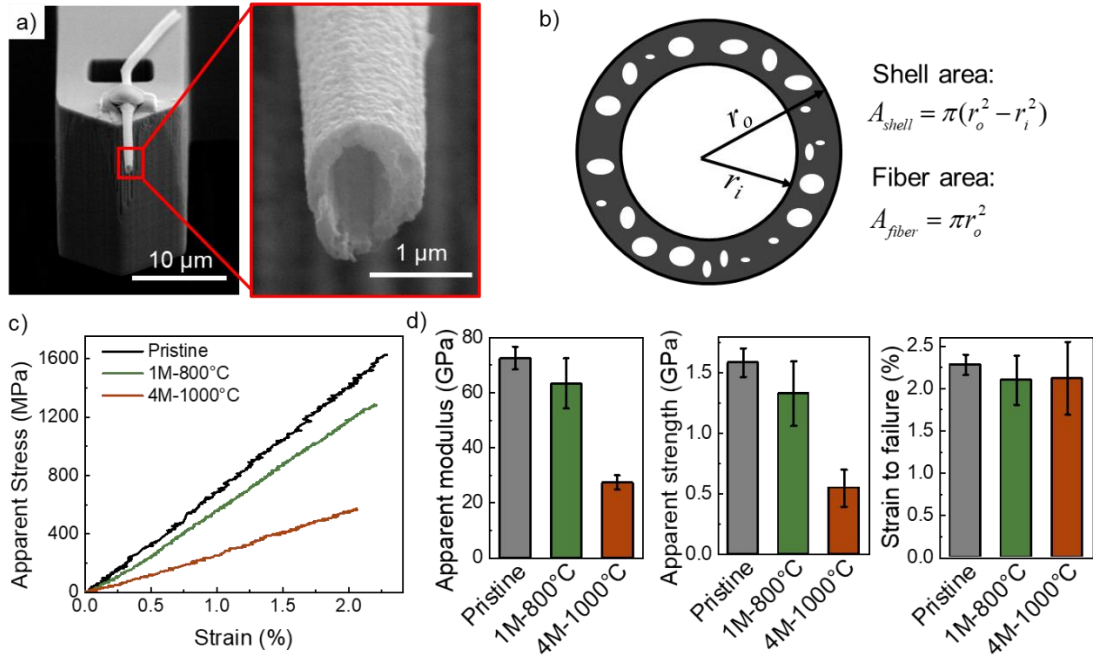
Figure 5.8. a) porous CNF fracture surface after the tensile test, b) schematic for the porous CNF, c) stress-strain curve for pristine, 1M-800 °C and 4M-1000 °C porous CNFs, d) apparent modulus, apparent strength and strain to failure for pristine, 1M-800 °C and 4M-1000 °C porous CNFs. Reprinted from [72] with permission.

5.2.3. Mechanical property of porous CNFs

Single fiber tensile tests were performed on the pristine, 1M-800 °C and 4M-1000 °C porous CNFs to evaluate the load-bearing capability of the porous CNFs. Four porous CNFs were tested in each case. Fracture surfaces (as shown in **Figure 5.8**a) of the porous CNFs were observed in SEM to measure the shell area (A_{shell}) and fiber area (A_{fiber}), as shown in the schematic in Figure 5.8b. The apparent stress was calculated as $S_{apparent} = F / A_{shell}$, and the engineering stress was calculated as $S_{apparent} = F / A_{fiber}$ where F represent the force experience by the porous CNFs. The apparent stress excludes the hollow core to reflect the material properties (it does not exclude the area of the pores

within the shell from the total area), whereas the engineering stress takes into account the hollow core, thus making the engineering strength a more realistic property to be considered for real applications. The apparent stress-strain curves remained linear until fracture in all three cases (Figure 5.8c), i.e., a brittle fracture behavior. As expected, the KOH activation reduced the mechanical properties by eliminating load-bearing material from porous CNFs as shown in Figure 5.8d and **Table 5.5**. The apparent modulus and strength decreased by 12.6% and 16.2% for 1M-800 °C activation, and 62.3% and 65.5% for 4M-1000 °C activation, respectively. The strain to failure for both KOH-activated porous CNFs remained relatively close to the pristine porous CNFs

The reduction in mechanical properties after KOH activation can be attributed to the following three mechanisms. First, KOH activation will increase the porosity and reduce the load-bearing area. Second, pores can cause stress concentration which will reduce the strength. Third, KOH activation increased the interlayer spacing in the graphitic turbostratic domains by introducing defects as discussed in section 2.1. This could slightly reduce the mechanical properties of the turbostratic domains. The porosity generated during the activation is proportional to the mass loss ratio. Close examination of the mechanical properties and mass loss ratio suggests that the modulus and strength reduction follow a similar trend as the mass loss ratio. For 1M-800 °C activation, the modulus reduction of 12.6% is very close to the 13.2% mass loss, suggesting that the reduction in modulus is mainly due to a loss in load-bearing area (first mechanism), whereas the 16.2% decrease in apparent strength is slightly larger than the mass loss, suggesting a small contribution of stress concentration (second mechanism) and change in turbostratic

130

domains (third mechanism). The latter effect is expected because according to a previous study, the stress concentration around the pores are strongly related to the pore shape.[49] Since the 1M-800 °C activation condition was mild, the pore structure and shape were preserved (Figure 5.2i & j) and the d-spacing had a small increase, as discussed in section 2.1. However, in the case of 4M-1000 °C, the respective 62.3% and 65.5% reduction in modulus and strength are higher than the 55.0% mass loss, indicating that in addition to the increase in porosity, the stress concentration around pores and change in turbostratic domains may have contributed to the loss in the apparent strength and modulus. During 4M-1000 °C activation, the pores grew in size and became more irregular (Figure 5.2l & m), as discussed in section 2.1. These irregular pore walls increase the stress concentration. In addition, the d spacing in the turbostratic domains increased significantly, which could also contribute to the reduction in mechanical properties. The strain to failure experienced much smaller reduction compared to strength and modulus, 8.1% for 1M-800 °C and 7.2% for 4M-1000 °C. This is because strain to failure is a material property which is independent of the reduction in load-bearing area. In other words, it is only affected by stress concentration and change of the turbostratic domains, which both had small contribution to the reduction of the mechanical properties.

Table 5.5. Mechanical properties of porous CNFs. Reprinted from [72] with permission.

| | Mass loss (%) | Strength (GPa) | | Reduction | Modulus (GPa) | | Reduction | Strain to failure (%) | Reduction |
		Apparent	Eng		Apparent	Eng			
Pristine	N.A.	1.59 ± 0.12	0.96 ± 0.07	0	72.6 ± 4.1	44.0 ± 2.5	0	2.28 ± 0.12	0
1M-800 °C	13.2	1.33 ± 0.27	0.80 ± 0.16	16.2%	63.4 ± 9.1	38.1 ± 5.5	12.6%	2.10 ± 0.29	8.1%
4M-1000 °C	55.0	0.55 ± 0.15	0.32 ± 0.09	65.5%	27.4 ± 2.6	15.9 ± 1.5	62.3%	2.12 ± 0.43	7.2%

5.2.4. Trade-off between energy storage and load-bearing

A specific capacitance vs strength plot (**Figure 5.9**a) was used to compare different porous CNFs and activated CFs. The capacitance increased by four times reaching 138.2 F/g after the 1M-800 °C activation with only 16.2% decrease in strength. The greatest specific capacitance of 191.3 F/g was achieved with 4M-1000 °C activation which is close to capacitance of graphene-based supercapacitors. However, this increase of capacitance comes at the cost of greater strength reduction (65.5%). While the strength of activated porous CNFs is slightly lower than activated CFs, the capacitance of activated porous CNFs is two orders of magnitude higher.

It is important to note that the mechanical properties of the porous CNFs are based on single fiber tensile tests, which may not fully represent the properties of a CNF mat. The mechanical properties of a mat are dependent on many other factors such as the fiber alignment, linear density and surface condition of the fibers (e.g. sizing, bonding with a matrix or bonding between fibers). The discussion of mechanical properties of CNF mat is more complicated and beyond the scope of this work. For a fair comparison, the results presented here for CNFs are compared with those on single fiber properties of CFs. During the KOH activation, the chemical reaction happens on the surface of the carbon material. In the case of CFs, the interior of the CFs is very difficult to be activated without severe material loss on the periphery and degradation of the mechanical properties, resulting in a low SSA and capacitance. In the case of porous CNFs, there are abundant surfaces from mesopores and hollow core for the chemical reaction to take place, resulting in much higher SSA and capacitance (Figure 5.9b) with a mild activation. As a result, comparing

to activated CFs[75], the capacitance increased by 73 times (from 2.63 F/g to 191.3 F/g) with only 86% decrease in apparent strength (from 3960 MPa to 550 MPa). This shows the great potential of using activated porous CNFs as structural supercapacitor electrode materials.

To analyze the trade-off between energy storage and load-bearing properties, a measure of multifunctional efficiency η_{mf} [47, 59] can be defined as:

$$\eta_{mf} = \eta_e + \eta_s = \frac{\sigma_{mf}}{\sigma_0} + \frac{C_{mf}}{C_0}$$,where σ_{mf} and C_{mf} are the strength and specific capacitance of the multifunctional material and σ_0 and C_0 are the strength and specific capacitance of a typical reference material. The factor η_{mf} must be larger than 1.0 in order for the multifunctional material to save weight in the system. Although the multifunctional efficiency lacks objectivity because the chosen reference materials are not standardized, it does provide insight when comparing different cases. For the purpose of discussion, the specific capacitance of active carbon (125 F/g) is selected as the typical electrode material,[188] and the strength of T300 carbon fiber (3500 MPa, single fiber strength) is selected as the typical load-bearing material. The η_{mf} for pristine, 1M-800 °C and 4M-1000 °C porous CNFs based on the engineering strength is 0.57, 1.33 and 1.62 respectively suggesting that the 4M-1000 °C activated porous CNFs are most favored for structural supercapacitors.
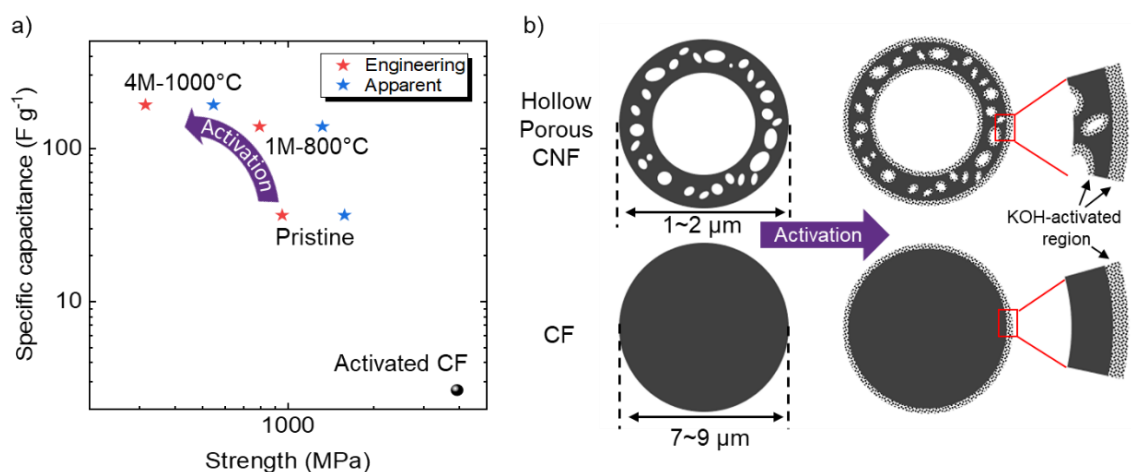
Figure 5.9. a) Specific capacitance vs strength plot for porous CNFs and activated CFs, porous CNFs from this work are marked by red stars (engineering strength) and blue stars (apparent strength), b) schematic showing difference between for activation of porous CNFs and CFs. Reprinted from [72] with permission.

5.3. Conclusion

In this chapter, porous CNFs were activated with KOH with different concentrations and activation temperatures. BET specific surface area for 1M-800 °C and 4M-1000 °C-treated porous CNFs increased by 20x and 34x to 1059.0 m^2/g and 1753.9 m^2/g comparing to pristine porous CNFs (52.3 m^2/g), respectively. The significant increase in SSA is due to the meso and micro pores generated during the KOH activation. Microstructural analysis revealed that the mesopore structure were preserved in 1M-800 °C activation and the mesopores grew in size in 4M-1000 °C activation. The interlayer spacing in the turbostratic domains also shows significant increase after activation. The activated porous CNFs showed excellent mechanical and energy storage capabilities. A clear trade-off between the energy storage and load-bearing capacities is demonstrated for the pristine and activated porous CNFs with different activation conditions. The specific

134

capacitance increased by 4x and 5x, reaching 138.2 F/g and 191.3 F/g for 1M-800 °C and 4M-1000 °C porous CNFs comparing to pristine porous CNFs (36.4 F/g) with a 16.2 % and 65.5 % decrease in strength and a 12.6 % and 62.3 % decrease in modulus for 1M-800 °C and 4M-1000 °C porous CNFs respectively. The multifunctional efficiency for 1M-800 °C and 4M-1000 °C porous CNFs increased to 1.33 and 1.62, indicating a good combination of load-bearing and energy storage functions as structural supercapacitor electrode material. These results suggest that the 4M-1000 °C porous CNFs is more favorable for structural energy storage application.

6. SUMMARY AND FUTURE DIRECTIONS

6.1. Summary

The overarching goal of this work was to establish the science and technology of using porous nanofiber as host for encapsulation and passive/active release of functional materials in response to external stimuli and structural energy storage.

The work was carried out in two phases. In the first phase, we established a broadly applicable porous fiber encapsulation platform based on sequential processing: In Chapter 2, the fabrication method and processing condition to achieve high mass loading of functional material in both non-conductive and conductive porous fibers were identified. Non-conductive porous PMMA fibers were fabricated through electrospinning by inducing phase separation. The microstructure of porous PMMA fibers fabricated with different solvent volatility and relative humidity suggest a clear nucleation and growth (NG) to spinodal decomposition (SD) transition by increasing relative humidity. Porous PMMA fibers with high porosity and interconnected pores to achieve high loading of functional material was obtained by promoting SD. Conductive porous CNFs were fabricated through electrospinning PAN/PMMA bicomponent fibers followed by selective removal of the sacrificial PMMA phase during carbonization. Porous CNFs with high porosity was fabricated by with PAN:PMMA ratio of 1:2 and a core/shell flow ratio of 1.4.

The influence of porous structure on the mechanical properties of the porous CNFs was discussed in Chapter 2. The modulus, strength, and the strain to failure of the porous CNFs was 65.0±6.2GPa, 1.28±0.14GPa and 2.1±0.3% respectively. When compared with

CNFs with no pores, modulus, strength, and the strain to failure of porous CNFs decreased by 13.9±2.1%, 35.5±4.9% and 25.8%±4.5% when pores were introduced in CNFs. This reduction in mechanical properties is attributed to both stress concentrations around pores and the loss in loading bearing area. Continuum mechanics models of the porous shell CNF were built to study the influence of the pore geometry on the strength of porous CNF. Pore curvature along the loading direction was identified to have the most significant influence on the strength.

A platform to encapsulate functional materials inside porous fibers and release them controllably was developed in Chapter 3. This platform is based on sequential processing of the porous fibers, followed by filling the fiber with functional materials and encapsulation through a polymer coating. We demonstrated the success of this platform in controllable release of antibacterial salt from porous PMMA fibers that were processes according to Chapter 2. The porous PMMA fibers were filled with high mass loading of an antibacterial salt (BAC) via a carrier solvent and capillary driven flow and encapsulated with a sub-micron PMMA coating via spray coating. Controllable radial release with a release time ranging from a few seconds to 53 minutes (more than 100x change in rate of release) was achieved by adjusting the coating thickness and modify the coating morphology via a solvent vapor treatment. In addition, axial release of the encapsulated material was demonstrated as a means to release a large volume of the functional material in response to fiber fracture.

In Chapter 4, active release of functional material using electric signal was demonstrated using conductive porous CNFs developed in Chapter 2. Porous CNF yarns

137

with a hierarchical porous structure was first made by twisting the precursor fibers. The antibacterial material, GV, was loaded into the porous CNFs yarns through a carrier solvent and a very high mass loading of 47.4 ± 5.4 % was achieved. A thin PCL coating was applied on the yarn to suppress the release of GV at deactivated state. Active release of the functional material was achieved by heating up the yarn via Joule heating which facilitate the diffusion of the functional material through the PCL coating. The release rate increased significantly with applied power, a ~39x increase in release rate was achieved by heating up the coating from room temperature to 49.4±1.0 °C. The change in release rate at different temperature followed the Arrhenius equation, and the activation energy for diffusion of GV in PCL was calculated to be 100.0 ± 3.9 kJ/mol.

The second phase of the project focused on use of the porous CNFs as structural energy storage material. In Chapter 5, porous CNFs were activated with KOH with different concentrations and activation temperatures. BET specific surface area for 1M-800 °C and 4M-1000 °C-treated porous CNFs increased by 20x and 34x to 1059.0 m^2/g and 1753.9 m^2/g comparing to pristine porous CNFs (52.3 m^2/g). A clear trade-off between the energy storage and load-bearing capacities was discovered for porous CNFs with different specific surface area. The specific capacitance increased by 4x and 5x, reaching 138.2 F/g and 191.3 F/g for 1M-800 °C and 4M-1000 °C porous CNFs comparing to pristine porous CNFs (36.4 F/g). with a 16.2 % and 65.5 % decrease in strength (1.33 ± 0.27 GPa and 0.55 ± 0.15 GPa) and a 12.6 % and 62.3 % decrease in modulus (63.4 ± 9.1 GPa and 27.4 ± 2.6 GPa) for 1M-800 °C and 4M-1000 °C porous CNFs comparing to pristine porous CNFs (strength of 1.59 ± 0.12 GPa and modulus of 72.6 ± 4.1 GPa). The

multifunctional efficiency increased from 0.57 for pristine CNFs to 1.33 and 1.62 for 1M-800 °C and 4M-1000 °C activated porous CNFs, indicating a good combination of load-bearing and energy storage functions in activated porous CNFs as structural energy storage materials. These results also suggest that the 4M-1000 °C porous CNFs is more favorable for structural energy storage application.

6.2. Future directions

With respect to material encapsulation, as demonstrated in this work, a wide range of materials from electrically conductive to nonconductive can be used as porous fiber host for the functional material, allowing passive and active release of functional material. This could open up new possibility in smart textiles and autonomous composites. One future direction can be focused on the implementation of this platform in developing self-healing composite which can repair microcracks on demand. In the existing methods for self-healing composites based on microcapsules and microvascular network, the healing can only be initiated by cracks which damages the microcapsules or the microvascular networks. Usually the reservoirs of healing agents can only be damaged by large cracks. Using the porous CNF based encapsulation platform, porous CNFs containing self-healing agent such as dicyclopentadiene (DCPD) can be embedded into composites. When microcracks are detected, the DCPD can then be released using an electric signal to repair the microcracks.

Although the porous CNFs showed decent mechanical properties, there is still room for improvement. In chapter 2, The pore curvature was identified to be the critical

139

factor which influences the strength of the porous CNFs, another future direction is to design the porous CNFs with optimized pore shape which could minimize the penalty for the existence of the porous structure on the mechanical properties. Hot drawing has been proved to significantly improve the mechanical properties of regular electrospun CNFs by inducing polymer chain alignment. In the case of porous CNFs, the effect of hot drawing is not limited to improving the intrinsic property of the carbon, it can also control the pore shape which could potentially lead to the design of more resilient porous CNFs.

With respect to structural energy storage, porous CNFs also showed a promising trade-off between the energy storage and load-bearing, which laid the foundation for their application in structural energy storage structures. However, the mechanical properties in this work were limited to single fibers. When it comes to a larger scale for the electrode or the entire energy storage device, the trade-off remains unexplored. One future direction is to fabricate a composite structure using the porous CNF as reinforcement and electroactive polymers such as polyaniline (PANI) as matrix to provide both high energy storage and good mechanical property on the scale of electrode or structural component.

REFERENCES

1.   Coyle, S.; Wu, Y. Z.; Lau, K. T.; De Rossi, D.; Wallace, G.; Diamond, D., Smart nanotextiles: A review of materials and applications. *Mrs Bull* **2007,** *32* (5), 434-442.

2.   Mondal, S., Phase change materials for smart textiles - An overview. *Appl Therm Eng* **2008,** *28* (11-12), 1536-1550.

3.   Casper, C. L.; Yamaguchi, N.; Kiick, K. L.; Rabolt, J. F., Functionalizing electrospun fibers with biologically relevant macromolecules. *Biomacromolecules* **2005,** *6* (4), 1998-2007.

4.   Ignatova, M.; Rashkov, I.; Manolova, N., Drug-loaded electrospun materials in wound-dressing applications and in local cancer treatment. *Expert Opin Drug Deliv* **2013,** *10* (4), 469-83.

5.   Sy, J. C.; Klemm, A. S.; Shastri, V. P., Emulsion as a Means of Controlling Electrospinning of Polymers. *Adv. Mater.* **2009,** *21* (18), 1814-+.

6.   Chew, S. Y.; Wen, J.; Yim, E. K. F.; Leong, K. W., Sustained release of proteins from electrospun biodegradable fibers. *Biomacromolecules* **2005,** *6* (4), 2017-2024.

7.   Arbab, S.; Noorpanah, P.; Mohammadi, N.; Zeinolebadi, A., Exploring the effects of non-solvent concentration, jet-stretching and hot-drawing on microstructure formation of poly(acrylonitrile) fibers during wet-spinning. *Journal of Polymer Research* **2011,** *18* (6), 1343-1351.

8.   Zamani, M.; Prabhakaran, M. P.; Ramakrishna, S., Advances in drug delivery via electrospun and electrosprayed nanomaterials. *Int. J. Nanomed.* **2013,** *8*, 2997-3017.

9.   Hu, X.; Liu, S.; Zhou, G.; Huang, Y.; Xie, Z.; Jing, X., Electrospinning of polymeric nanofibers for drug delivery applications. *J Control Release* **2014,** *185*, 12-21.

10.   Doan, T. Q.; Leslie, L. S.; Kim, S. Y.; Bhargava, R.; White, S. R.; Sottos, N. R., Characterization of core-shell microstructure and self-healing performance of electrospun fiber coatings. *Polymer* **2016,** *107*, 263-272.

11.   Wu, X.-F.; Rahman, A.; Zhou, Z.; Pelot, D. D.; Sinha-Ray, S.; Chen, B.; Payne, S.; Yarin, A. L., Electrospinning core-shell nanofibers for interfacial toughening and self-healing of carbon-fiber/epoxy composites. *J. Appl. Polym. Sci.* **2013,** *129* (3), 1383-1393.

12.   Sinha-Ray, S.; Pelot, D. D.; Zhou, Z. P.; Rahman, A.; Wu, X. F.; Yarin, A. L., Encapsulation of self-healing materials by coelectrospinning, emulsion electrospinning, solution blowing and intercalation. *J. Mater. Chem.* **2012,** *22* (18), 9138.

13.   Mitchell, T. J.; Keller, M. W., Coaxial electrospun encapsulation of epoxy for use in self-healing materials. *Polymer International* **2013,** *62* (6), 860-866.

14.   Bodmeier, R.; Mcginity, J. W., Polylactic Acid Microspheres Containing Quinidine Base and Quinidine Sulfate Prepared by the Solvent Evaporation Technique .2. Some Process Parameters Influencing the Preparation and Properties of Microspheres. *Journal of Microencapsulation* **1987,** *4* (4), 289-297.

15.   White, S. R.; Sottos, N. R.; Geubelle, P. H.; Moore, J. S.; Kessler, M. R.; Sriram, S. R.; Brown, E. N.; Viswanathan, S., Autonomic healing of polymer composites. *Nature* **2001,** *409* (6822), 794-7.

16.   Toncheva, A.; Paneva, D.; Maximova, V.; Manolova, N.; Rashkov, I., Antibacterial fluoroquinolone antibiotic-containing fibrous materials from poly(L-lactide-co-D,L-lactide) prepared by electrospinning. *Eur. J. Pharm. Sci.* **2012,** *47* (4), 642-51.

17.   Chew, S. Y.; Wen, J.; Yim, E. K.; Leong, K. W., Sustained release of proteins from electrospun biodegradable fibers. *Biomacromolecules* **2005,** *6* (4), 2017-24.

18.   Xu, X.; Yang, L.; Xu, X.; Wang, X.; Chen, X.; Liang, Q.; Zeng, J.; Jing, X., Ultrafine medicated fibers electrospun from W/O emulsions. *J Control Release* **2005,** *108* (1), 33-42.

19.   Sun, Z.; Fan, C.; Tang, X.; Zhao, J.; Song, Y.; Shao, Z.; Xu, L., Characterization and antibacterial properties of porous fibers containing silver ions. *Appl Surf Sci* **2016,** *387*, 828-838.

20.   Jeevani, T., Nanotextiles-a broader perspective. *Journal of Nanomedicine & Nanotechnology* **2012,** *2011*.

21.   Feng, J.; Hontanon, E.; Blanes, M.; Meyer, J.; Guo, X.; Santos, L.; Paltrinieri, L.; Ramlawi, N.; Smet, L. C.; Nirschl, H.; Kruis, F. E.; Schmidt-Ott, A.; Biskos, G., Scalable and Environmentally Benign Process for Smart Textile Nanofinishing. *ACS Appl Mater Interfaces* **2016,** *8* (23), 14756-65.

22.   Sun, Z. C.; Zussman, E.; Yarin, A. L.; Wendorff, J. H.; Greiner, A., Compound core-shell polymer nanofibers by co-electrospinning. *Adv. Mater.* **2003,** *15* (22), 1929-+.

23.   Jiang, H.; Hu, Y.; Li, Y.; Zhao, P.; Zhu, K.; Chen, W., A facile technique to prepare biodegradable coaxial electrospun nanofibers for controlled release of bioactive agents. *J Control Release* **2005,** *108* (2-3), 237-43.

24.   Ji, W.; Sun, Y.; Yang, F.; van den Beucken, J. J.; Fan, M.; Chen, Z.; Jansen, J. A., Bioactive electrospun scaffolds delivering growth factors and genes for tissue engineering applications. *Pharmaceutical research* **2011,** *28* (6), 1259-72.

25.   Li, D.; Xia, Y., Electrospinning of Nanofibers: Reinventing the Wheel? *Adv. Mater.* **2004,** *16* (14), 1151-1170.

26.   Esfahani, H.; Jose, R.; Ramakrishna, S., Electrospun Ceramic Nanofiber Mats Today: Synthesis, Properties, and Applications. *Materials (Basel)* **2017,** *10* (11).

27.   Haslauer, C. M.; Moghe, A. K.; Osborne, J. A.; Gupta, B. S.; Loboa, E. G., Collagen-PCL sheath-core bicomponent electrospun scaffolds increase osteogenic differentiation and calcium accretion of human adipose-derived stem cells. *J Biomater Sci Polym Ed* **2011,** *22* (13), 1695-712.

28.   Bhardwaj, N.; Kundu, S. C., Electrospinning: a fascinating fiber fabrication technique. *Biotechnol Adv* **2010,** *28* (3), 325-47.

29.   Buzgo, M.; Mickova, A.; Rampichova, M.; Doupnik, M., Blend electrospinning, coaxial electrospinning, and emulsion electrospinning techniques. In *Core-Shell Nanostructures for Drug Delivery and Theranostics*, 2018; pp 325-347.

30.   Yu, D. G.; Zhou, J.; Chatterton, N. P.; Li, Y.; Huang, J.; Wang, X., Polyacrylonitrile nanofibers coated with silver nanoparticles using a modified coaxial electrospinning process. *Int J Nanomedicine* **2012,** *7*, 5725-32.

31.   Dong, H.; Wang, D.; Sun, G.; Hinestroza, J. P., Assembly of Metal Nanoparticles on Electrospun Nylon 6 Nanofibers by Control of Interfacial Hydrogen-Bonding Interactions. *Chem. Mater.* **2008,** *20* (21), 6627-6632.

32.   Kenawy, E. R.; Bowlin, G. L.; Mansfield, K.; Layman, J.; Simpson, D. G.; Sanders, E. H.; Wnek, G. E., Release of tetracycline hydrochloride from electrospun poly(ethylene-co-vinylacetate), poly(lactic acid), and a blend. *J Control Release* **2002,** *81* (1-2), 57-64.

33.   Toncheva, A.; Paneva, D.; Manolova, N.; Rashkov, I., Electrospun poly(L-lactide) membranes containing a single drug or multiple drug system for antimicrobial wound dressings. *Macromolecular Research* **2011,** *19* (12), 1310-1319.

34.   Hong, K. H.; Park, J. L.; Sul, I. H.; Youk, J. H.; Kang, T. J., Preparation of antimicrobial poly(vinyl alcohol) nanofibers containing silver nanoparticles. *J. Polym. Sci. Pt. B-Polym. Phys.* **2006,** *44* (17), 2468-2474.

35.   Qi, H. X.; Hu, P.; Xu, J.; Wang, A. J., Encapsulation of drug reservoirs in fibers by emulsion electrospinning: Morphology characterization and preliminary release assessment. *Biomacromolecules* **2006,** *7* (8), 2327-2330.

36.   Yazgan, G.; Popa, A. M.; Rossi, R. M.; Maniura-Weber, K.; Puigmarti-Luis, J.; Crespy, D.; Fortunato, G., Tunable release of hydrophilic compounds from hydrophobic nanostructured fibers prepared by emulsion electrospinning. *Polymer* **2015,** *66*, 268-276.

37.   Park, J. H.; Braun, P. V., Coaxial electrospinning of self-healing coatings. *Adv Mater* **2010,** *22* (4), 496-9.

38.   Lee, M. W.; An, S.; Jo, H. S.; Yoon, S. S.; Yarin, A. L., Self-Healing Nanofiber-Reinforced Polymer Composites. 1. Tensile Testing and Recovery of Mechanical Properties. *ACS Appl Mater Interfaces* **2015,** *7* (35), 19546-54.

39.   Lee, M. W.; An, S.; Jo, H. S.; Yoon, S. S.; Yarin, A. L., Self-healing Nanofiber-Reinforced Polymer Composites. 2. Delamination/Debonding and Adhesive and Cohesive Properties. *ACS Appl Mater Interfaces* **2015,** *7* (35), 19555-61.

40.   Puppi, D.; Chiellini, F., Drug release kinetics of electrospun fibrous systems. In *Core-Shell Nanostructures for Drug Delivery and Theranostics*, 2018; pp 349-374.

41.   Chen, Y.; Boyd, J. G.; Naraghi, M., Porous fibres with encapsulated functional materials and tunable release. *J Microencapsul* **2017,** *34* (4), 383-394.

42.   Chien, A.-T.; Cho, S.; Joshi, Y.; Kumar, S., Electrical conductivity and Joule heating of polyacrylonitrile/carbon nanotube composite fibers. *Polymer* **2014,** *55* (26), 6896-6905.

43.   Hayes, S. A.; Lafferty, A. D.; Altinkurt, G.; Wilson, P. R.; Collinson, M.; Duchene, P., Direct electrical cure of carbon fiber composites. *Advanced Manufacturing: Polymer & Composites Science* **2015,** *1* (2), 112-119.

44.   Vrentas, J. S.; Duda, J. L., Diffusion in polymer–solvent systems. II. A predictive theory for the dependence of diffusion coefficients on temperature, concentration, and molecular weight. *Journal of Polymer Science: Polymer Physics Edition* **1977,** *15* (3), 417-439.

45.   Brandt, W. W., Model Calculation of the Temperature Dependence of Small Molecule Diffusion in High Polymers. *J Phys Chem-Us* **1959,** *63* (7), 1080-1084.

46.   Benson, J.; Kovalenko, I.; Boukhalfa, S.; Lashmore, D.; Sanghadasa, M.; Yushin, G., Multifunctional CNT-polymer composites for ultra-tough structural supercapacitors and desalination devices. *Adv. Mater.* **2013,** *25* (45), 6625-32.

47.   Chan, K. Y.; Jia, B.; Lin, H.; Hameed, N.; Lee, J. H.; Lau, K. T., A critical review on multifunctional composites as structural capacitors for energy storage. *Compos. Struct.* **2018,** *188*, 126-142.

48.   Gonzalez, C.; Vilatela, J. J.; Molina-Aldareguia, J. M.; Lopes, C. S.; LLorca, J., Structural composites for multifunctional applications: Current challenges and future trends. *Prog. Mater Sci.* **2017,** *89*, 194-251.

49.   Chen, Y.; Cai, J.; Boyd, J. G.; Kennedy, W. J.; Naraghi, M., Mechanics of Emulsion Electrospun Porous Carbon Fibers as Building Blocks of Multifunctional Materials. *ACS Appl. Mater. Interfaces* **2018,** *10* (44), 38310-38318.

50.   Kjell, M. H.; Jacques, E.; Zenkert, D.; Behm, M.; Lindbergh, G., PAN-Based Carbon Fiber Negative Electrodes for Structural Lithium-Ion Batteries. *J. Electrochem. Soc.* **2011,** *158* (12), A1455-A1460.

51.   Liu, P.; Sherman, E.; Jacobsen, A., Design and fabrication of multifunctional structural batteries. *J. Power Sources* **2009,** *189* (1), 646-650.

52.   Snyder, J. F.; Carter, R. H.; Wetzel, E. D., Electrochemical and mechanical behavior in mechanically robust solid polymer electrolytes for use in multifunctional structural batteries. *Chem. Mater.* **2007,** *19* (15), 3793-3801.

53.   Asp, L. E.; Greenhalgh, E. S., Structural power composites. *Compos. Sci. Technol.* **2014,** *101*, 41-61.

54.   Snyder, J. F.; Wong, E. L.; Hubbard, C. W., Evaluation of Commercially Available Carbon Fibers, Fabrics, and Papers for Potential Use in Multifunctional Energy Storage Applications. *J. Electrochem. Soc.* **2009,** *156* (3), A215-A224.

55.   Senokos, E.; Ou, Y.; Torres, J. J.; Sket, F.; Gonzalez, C.; Marcilla, R.; Vilatela, J. J., Energy storage in structural composites by introducing CNT fiber/polymer electrolyte interleaves. *Sci. Rep.* **2018,** *8* (1), 3407.

56.   Wang, G.; Zhang, L.; Zhang, J., A review of electrode materials for electrochemical supercapacitors. *Chem Soc Rev* **2012,** *41* (2), 797-828.

57.   Malik, R.; Zhang, L.; McConnell, C.; Schott, M.; Hsieh, Y. Y.; Noga, R.; Alvarez, N. T.; Shanov, V., Three-dimensional, free-standing polyaniline/carbon nanotube composite-based electrode for high-performance supercapacitors. *Carbon* **2017,** *116*, 579-590.

58.   Sheng, L. Z.; Chang, J.; Jiang, L. L.; Jiang, Z. M.; Liu, Z.; Wei, T.; Fan, Z. J., Multilayer-Folded Graphene Ribbon Film with Ultrahigh Areal Capacitance and High Rate Performance for Compressible Supercapacitors. *Adv. Funct. Mater.* **2018,** *28* (21).

59.   Kwon, S. R.; Harris, J.; Zhou, T.; Loufakis, D.; Boyd, J. G.; Lutkenhaus, J. L., Mechanically Strong Graphene/Aramid Nanofiber Composite Electrodes for Structural Energy and Power. *Acs Nano* **2017,** *11* (7), 6682-6690.

60.   Weng, Z.; Su, Y.; Wang, D. W.; Li, F.; Du, J. H.; Cheng, H. M., Graphene-Cellulose Paper Flexible Supercapacitors. *Adv. Energy. Mater.* **2011,** *1* (5), 917-922.

61.   Wang, D. W.; Li, F.; Zhao, J.; Ren, W.; Chen, Z. G.; Tan, J.; Wu, Z. S.; Gentle, I.; Lu, G. Q.; Cheng, H. M., Fabrication of Graphene/Polyaniline Composite Paper via In Situ Anodic Electropolymerization for High-Performance Flexible Electrode. *Acs Nano* **2009,** *3* (7), 1745-52.

62.   Yu, M. F.; Files, B. S.; Arepalli, S.; Ruoff, R. S., Tensile loading of ropes of single wall carbon nanotubes and their mechanical properties. *Phys. Rev. Lett.* **2000,** *84* (24), 5552-5.

63.   Peng, B.; Locascio, M.; Zapol, P.; Li, S.; Mielke, S. L.; Schatz, G. C.; Espinosa, H. D., Measurements of near-ultimate strength for multiwalled carbon nanotubes and irradiation-induced crosslinking improvements. *Nat. Nanotechnol.* **2008,** *3* (10), 626-31.

64.   Coleman, J. N.; Khan, U.; Blau, W. J.; Gun'ko, Y. K., Small but strong: A review of the mechanical properties of carbon nanotube–polymer composites. *Carbon* **2006,** *44* (9), 1624-1652.

65.   Papageorgiou, D. G.; Kinloch, I. A.; Young, R. J., Mechanical properties of graphene and graphene-based nanocomposites. *Prog. Mater Sci.* **2017,** *90*, 75-127.

66.   Xu, J. M.; Zhang, D., Multifunctional structural supercapacitor based on graphene and geopolymer. *Electrochim. Acta* **2017,** *224*, 105-112.

67.   Ma, Y.; Li, P.; Sedloff, J. W.; Zhang, X.; Zhang, H.; Liu, J., Conductive graphene fibers for wire-shaped supercapacitors strengthened by unfunctionalized few-walled carbon nanotubes. *Acs Nano* **2015,** *9* (2), 1352-9.

68.   Che, J. F.; Chen, P.; Chan-Park, M. B., High-strength carbon nanotube buckypaper composites as applied to free-standing electrodes for supercapacitors. *J. Mater. Chem. A* **2013,** *1* (12), 4057-4066.

69.   Lee, J. A.; Shin, M. K.; Kim, S. H.; Kim, S. J.; Spinks, G. M.; Wallace, G. G.; Ovalle-Robles, R.; Lima, M. D.; Kozlov, M. E.; Baughman, R. H., Hybrid

149

nanomembranes for high power and high energy density supercapacitors and their yarn application. *Acs Nano* **2012,** *6* (1), 327-34.

70.   Senokos, E.; Reguero, V.; Cabana, L.; Palma, J.; Marcilla, R.; Vilatela, J. J., Large-Area, All-Solid, and Flexible Electric Double Layer Capacitors Based on CNT Fiber Electrodes and Polymer Electrolytes. *Adv. Mater. Technol.* **2017,** *2* (7).

71.   Lee, J. A.; Shin, M. K.; Kim, S. H.; Cho, H. U.; Spinks, G. M.; Wallace, G. G.; Lima, M. D.; Lepro, X.; Kozlov, M. E.; Baughman, R. H.; Kim, S. J., Ultrafast charge and discharge biscrolled yarn supercapacitors for textiles and microdevices. *Nat. Commun.* **2013,** *4*, 1970.

72.   Chen, Y.; Amiri, A.; Boyd, J. G.; Naraghi, M., Promising Trade‐Offs Between Energy Storage and Load Bearing in Carbon Nanofibers as Structural Energy Storage Devices. *Adv. Funct. Mater.* **2019,** *29* (33).

73.   Greenhalgh, E. S.; Ankersen, J.; Asp, L. E.; Bismarck, A.; Fontana, Q. P. V.; Houlle, M.; Kalinka, G.; Kucernak, A.; Mistry, M.; Nguyen, S.; Qian, H.; Shaffer, M. S. P.; Shirshova, N.; Steinke, J. H. G.; Wienrich, M., Mechanical, electrical and microstructural characterisation of multifunctional structural power composites. *J. Compos. Mater.* **2014,** *49* (15), 1823-1834.

74.   Shirshova, N.; Qian, H.; Shaffer, M. S. P.; Steinke, J. H. G.; Greenhalgh, E. S.; Curtis, P. T.; Kucernak, A.; Bismarck, A., Structural composite supercapacitors. *Compos. Pt. A-Appl. Sci. Manuf.* **2013,** *46*, 96-107.

75.   Qian, H.; Diao, H.; Shirshova, N.; Greenhalgh, E. S.; Steinke, J. G.; Shaffer, M. S.; Bismarck, A., Activation of structural carbon fibres for potential applications in multifunctional structural supercapacitors. *J. Colloid Interface Sci.* **2013,** *395*, 241-8.

76.   Carlson, T.; Asp, L. E., Structural carbon fibre composite/PET capacitors – Effects of dielectric separator thickness. *Compos. Part B-Eng.* **2013,** *49*, 16-21.

77.   Zhu, Y.; Murali, S.; Stoller, M. D.; Ganesh, K. J.; Cai, W.; Ferreira, P. J.; Pirkle, A.; Wallace, R. M.; Cychosz, K. A.; Thommes, M.; Su, D.; Stach, E. A.; Ruoff, R. S., Carbon-based supercapacitors produced by activation of graphene. *Science* **2011,** *332* (6037), 1537-41.

78.   Bae, S. H.; Jeon, C.; Oh, S.; Kim, C. G.; Seo, M.; Oh, I. K., Load-bearing supercapacitor based on bicontinuous PEO-b-P(S-co-DVB) structural electrolyte integrated with conductive nanowire-carbon fiber electrodes. *Carbon* **2018,** *139*, 10-20.

79.   Deka, B. K.; Hazarika, A.; Kim, J.; Park, Y.-B.; Park, H. W., Multifunctional CuO nanowire embodied structural supercapacitor based on woven carbon fiber/ionic liquid–polyester resin. *Compos. Pt. A-Appl. Sci. Manuf.* **2016,** *87*, 256-262.

80.   Javaid, A.; Irfan, M., Multifunctional structural supercapacitors based on graphene nanoplatelets/carbon aerogel composite coated carbon fiber electrodes. *Mater. Res. Express.* **2018,** *6* (1).

81.   Qian, H.; Kucernak, A. R.; Greenhalgh, E. S.; Bismarck, A.; Shaffer, M. S., Multifunctional structural supercapacitor composites based on carbon aerogel modified high performance carbon fiber fabric. *ACS Appl. Mater. Interfaces* **2013,** *5* (13), 6113-22.

82.   Zhang, B. A.; Kang, F. Y.; Tarascon, J. M.; Kim, J. K., Recent advances in electrospun carbon nanofibers and their application in electrochemical energy storage. *Prog. Mater Sci.* **2016,** *76*, 319-380.

83.   Tran, C.; Kalra, V., Fabrication of porous carbon nanofibers with adjustable pore sizes as electrodes for supercapacitors. *J. Power Sources* **2013,** *235*, 289-296.

84.   Le, T. H.; Yang, Y.; Yu, L.; Gao, T. J.; Huang, Z. H.; Kang, F. Y., Polyimide-based porous hollow carbon nanofibers for supercapacitor electrode. *J. Appl. Polym. Sci.* **2016,** *133* (19), n/a-n/a.

85.   He, T. S.; Su, Q. Y.; Yildiz, Z.; Cai, K. D.; Wang, Y. J., Ultrafine Carbon Fibers with Hollow-Porous Multilayered Structure for Supercapacitors. *Electrochim. Acta* **2016,** *222*, 1120-1127.

86.   Kim, C.; Yang, K. S., Electrochemical properties of carbon nanofiber web as an electrode for supercapacitor prepared by electrospinning. *Appl. Phys. Lett.* **2003,** *83* (6), 1216-1218.

87.   Yoon, S. H.; Lim, S.; Song, Y.; Ota, Y.; Qiao, W. M.; Tanaka, A.; Mochida, I., KOH activation of carbon nanofibers. *Carbon* **2004,** *42* (8-9), 1723-1729.

88.   Kim, C., Electrochemical characterization of electrospun activated carbon nanofibres as an electrode in supercapacitors. *J. Power Sources* **2005,** *142* (1-2), 382-388.

89.   Zhi, M. J.; Liu, S. H.; Hong, Z. L.; Wu, N. Q., Electrospun activated carbon nanofibers for supercapacitor electrodes. *Rsc Adv* **2014,** *4* (82), 43619-43623.

90.   Barranco, V.; Lillo-Rodenas, M. A.; Linares-Solano, A.; Oya, A.; Pico, F.; Ibanez, J.; Agullo-Rueda, F.; Amarilla, J. M.; Rojo, J. M., Amorphous Carbon Nanofibers and

Their Activated Carbon Nanofibers as Supercapacitor Electrodes. *J Phys. Chem. C* **2010,** *114* (22), 10302-10307.

91.   Cai, J. Z.; Naraghi, M., The formation of highly ordered graphitic interphase around embedded CNTs controls the mechanics of ultra-strong carbonized nanofibers. *Acta Mater.* **2019,** *162*, 46-54.

92.   Cai, J. Z.; Naraghi, M., Non-intertwined graphitic domains leads to super strong and tough continuous 1D nanostructures. *Carbon* **2018,** *137*, 242-251.

93.   Chawla, S.; Cai, J. Z.; Naraghi, M., Mechanical tests on individual carbon nanofibers reveals the strong effect of graphitic alignment achieved via precursor hot-drawing. *Carbon* **2017,** *117*, 208-219.

94.   Bognitzki, M.; Czado, W.; Frese, T.; Schaper, A.; Hellwig, M.; Steinhart, M.; Greiner, A.; Wendorff, J. H., Nanostructured fibers via electrospinning. *Adv. Mater.* **2001,** *13* (1), 70-+.

95.   Megelski, S.; Stephens, J. S.; Chase, D. B.; Rabolt, J. F., Micro- and nanostructured surface morphology on electrospun polymer fibers. *Macromolecules* **2002,** *35* (22), 8456-8466.

96.   Casper, C. L.; Stephens, J. S.; Tassi, N. G.; Chase, D. B.; Rabolt, J. F., Controlling surface morphology of electrospun polystyrene fibers: Effect of humidity and molecular weight in the electrospinning process. *Macromolecules* **2004,** *37* (2), 573-578.

97.   Dayal, P.; Liu, J.; Kumar, S.; Kyu, T., Experimental and theoretical investigations of porous structure formation in electrospun fibers. *Macromolecules* **2007,** *40* (21), 7689-7694.

98.   Dayal, P.; Kyu, T., Porous fiber formation in polymer-solvent system undergoing solvent evaporation. *Journal of Applied Physics* **2006,** *100* (4), 043512.

99.   Yang, Y.; Centrone, A.; Chen, L.; Simeon, F.; Hatton, T. A.; Rutledge, G. C., Highly porous electrospun polyvinylidene fluoride (PVDF)-based carbon fiber. *Carbon* **2011,** *49* (11), 3395-3403.

100.   Medeiros, E. S.; Mattoso, L. H. C.; Offeman, R. D.; Wood, D. F.; Orts, W. J., Effect of relative humidity on the morphology of electrospun polymer fibers. *Can J Chem* **2008,** *86* (6), 590-599.

101.   Fashandi, H.; Karimi, M., Pore formation in polystyrene fiber by superimposing temperature and relative humidity of electrospinning atmosphere. *Polymer* **2012,** *53* (25), 5832-5849.

102.   Kim, G. T.; Lee, J. S.; Shin, J. H.; Ahn, Y. C.; Hwang, Y. J.; Shin, H. S.; Lee, J. K.; Sung, C. M., Investigation of pore formation for polystyrene electrospun fiber: Effect of relative humidity. *Korean J Chem Eng* **2005,** *22* (5), 783-788.

103.   Pai, C.-L.; Boyce, M. C.; Rutledge, G. C., Morphology of Porous and Wrinkled Fibers of Polystyrene Electrospun from Dimethylformamide. *Macromolecules* **2009,** *42* (6), 2102-2114.

104.   Cao, S.; Hu, B.; Liu, H., FABRICATION OF NANO-POROUS STRUCTURED POLYLACTIDE (PLLA) FIBERS THROUGH ELECTROSPINNING. *Acta Polym Sin* **2010,** (10), 1193-1198.

105.   Lin, J.; Ding, B.; Yu, J., Direct fabrication of highly nanoporous polystyrene fibers via electrospinning. *ACS Appl Mater Interfaces* **2010,** *2* (2), 521-8.

106.   Li, L.; Jiang, Z.; Li, M. M.; Li, R. S.; Fang, T., Hierarchically structured PMMA fibers fabricated by electrospinning. *Rsc Adv* **2014,** *4* (95), 52973-52985.

107.   Bae, H.-S.; Haider, A.; Selim, K. M. K.; Kang, D.-Y.; Kim, E.-J.; Kang, I.-K., Fabrication of highly porous PMMA electrospun fibers and their application in the removal of phenol and iodine. *Journal of Polymer Research* **2013,** *20* (7).

108.   Nayani, K.; Katepalli, H.; Sharma, C. S.; Sharma, A.; Patil, S.; Venkataraghavan, R., Electrospinning Combined with Nonsolvent-Induced Phase Separation To Fabricate Highly Porous and Hollow Submicrometer Polymer Fibers. *Industrial & Engineering Chemistry Research* **2012,** *51* (4), 1761-1766.

109.   Huang, L. W.; Bui, N. N.; Manickam, S. S.; McCutcheon, J. R., Controlling Electrospun Nanofiber Morphology and Mechanical Properties Using Humidity. *J. Polym. Sci. Pt. B-Polym. Phys.* **2011,** *49* (24), 1734-1744.

110.   Yu, X.; Xiang, H.; Long, Y.; Zhao, N.; Zhang, X.; Xu, J., Preparation of porous polyacrylonitrile fibers by electrospinning a ternary system of PAN/DMF/H2O. *Materials Letters* **2010,** *64* (22), 2407-2409.

111.   Liu, W.; Huang, C.; Jin, X., Tailoring the grooved texture of electrospun polystyrene nanofibers by controlling the solvent system and relative humidity. *Nanoscale Res Lett* **2014,** *9* (1), 350.

112.   Lu, P.; Xia, Y., Maneuvering the internal porosity and surface morphology of electrospun polystyrene yarns by controlling the solvent and relative humidity. *Langmuir* **2013,** *29* (23), 7070-8.

113.   Zheng, J.; Zhang, H.; Zhao, Z.; Han, C. C., Construction of hierarchical structures by electrospinning or electrospraying. *Polymer* **2012,** *53* (2), 546-554.

114.   Fashandi, H.; Karimi, M., Characterization of porosity of polystyrene fibers electrospun at humid atmosphere. *Thermochim Acta* **2012,** *547*, 38-46.

115.   Demir, M. M., Investigation on glassy skin formation of porous polystyrene fibers electrospun from DMF. *Express Polymer Letters* **2010,** *4* (1), 2-8.

116.   Li, Y.; Lim, C. T.; Kotaki, M., Study on structural and mechanical properties of porous PLA nanofibers electrospun by channel-based electrospinning system. *Polymer* **2015,** *56*, 572-580.

117.   Srinivasarao, M.; Collings, D.; Philips, A.; Patel, S., Three-dimensionally ordered array of air bubbles in a polymer film. *Science* **2001,** *292* (5514), 79-83.

118.   Honarbakhsh, S.; Pourdeyhimi, B., Scaffolds for drug delivery, part I: electrospun porous poly(lactic acid) and poly(lactic acid)/poly(ethylene oxide) hybrid scaffolds. *J Mater Sci* **2011,** *46* (9), 2874-2881.

119.   Guo, H. F.; Laxminarayan, A.; Caneba, G. T.; Solc, K., Morphological-Studies of Late-Stage Spinodal Decomposition in Polystyrene-Cyclohexanol System. *J. Appl. Polym. Sci.* **1995,** *55* (5), 753-759.

120.   Kim, C.; Jeong, Y. I.; Ngoc, B. T. N.; Yang, K. S.; Kojima, M.; Kim, Y. A.; Endo, M.; Lee, J.-W., Synthesis and characterization of porous carbon nanofibers with hollow cores through the thermal treatment of electrospun copolymeric nanofiber webs. *Small* **2007,** *3* (1), 91-95.

121. Zhang, Z. Y.; Li, X. H.; Wang, C. H.; Fu, S. W.; Liu, Y. C.; Shao, C. L., Polyacrylonitrile and Carbon Nanofibers with Controllable Nanoporous Structures by Electrospinning. *Macromol Mater Eng* **2009,** *294* (10), 673-678.

122. Moon, S.; Choi, J.; Farris, R. J., Highly porous polyacrylonitrile/polystyrene nanofibers by electrospinning. *Fiber Polym* **2008,** *9* (3), 276-280.

123. Lee, S.; Lee, K.; Moon, G. D.; Won, Y. S.; Yoon, Y. J.; Park, S. S.; Kim, Y. R.; Jeong, U., Preparation of macroporous carbon nanofibers with macroscopic openings in the surfaces and their applications. *Nanotechnology* **2009,** *20* (44), 445702.

124. Ji, L.; Lin, Z.; Medford, A. J.; Zhang, X., Porous carbon nanofibers from electrospun polyacrylonitrile/SiO2 composites as an energy storage material. *Carbon* **2009,** *47* (14), 3346-3354.

125. Liu, H.; Cao, C.-Y.; Wei, F.-F.; Jiang, Y.; Sun, Y.-B.; Huang, P.-P.; Song, W.-G., Fabrication of Macroporous/Mesoporous Carbon Nanofiber Using CaCO3Nanoparticles as Dual Purpose Template and Its Application as Catalyst Support. *The Journal of Physical Chemistry C* **2013,** *117* (41), 21426-21432.

126. Ji, L. W.; Lin, Z.; Medford, A. J.; Zhang, X. W., Porous carbon nanofibers from electrospun polyacrylonitrile/SiO2 composites as an energy storage material. *Carbon* **2009,** *47* (14), 3346-3354.

127. Qie, L.; Chen, W. M.; Wang, Z. H.; Shao, Q. G.; Li, X.; Yuan, L. X.; Hu, X. L.; Zhang, W. X.; Huang, Y. H., Nitrogen-doped porous carbon nanofiber webs as anodes for lithium ion batteries with a superhigh capacity and rate capability. *Adv. Mater.* **2012,** *24* (15), 2047-2050.

128.   Lee, B. S.; Son, S. B.; Park, K. M.; Lee, G.; Oh, K. H.; Lee, S. H.; Yu, W. R., Effect of pores in hollow carbon nanofibers on their negative electrode properties for a lithium rechargeable battery. *ACS Appl Mater Interfaces* **2012,** *4* (12), 6702-6710.

129.   Lee, B. S.; Son, S. B.; Park, K. M.; Yu, W. R.; Oh, K. H.; Lee, S. H., Anodic properties of hollow carbon nanofibers for Li-ion battery. *J. Power Sources* **2012,** *199*, 53-60.

130.   Lai, C. C.; Lo, C. T., Preparation of Nanostructural Carbon Nanofibers and Their Electrochemical Performance for Supercapacitors. *Electrochim. Acta* **2015,** *183*, 85-93.

131.   Xi, J. Y.; Qiu, X. P.; Li, J.; Tang, X. Z.; Zhu, W. T.; Chen, L. Q., PVDF-PEO Blends Based Microporous Polymer Electrolyte: Effect of Peo on Pore Configurations and Ionic Conductivity. *J. Power Sources* **2006,** *157* (1), 501-506.

132.   Zander, N. E.; Strawhecker, K. E.; Orlicki, J. A.; Rawlett, A. M.; Beebe, T. P., Jr., Coaxial electrospun poly(methyl methacrylate)-polyacrylonitrile nanofibers: atomic force microscopy and compositional characterization. *Journal of Physical Chemistry B* **2011,** *115* (43), 12441-12447.

133.   Peng, M.; Li, D.; Shen, L.; Chen, Y.; Zheng, Q.; Wang, H., Nanoporous Structured Submicrometer Carbon Fibers Prepared via Solution Electrospinning of Polymer Blends. *Langmuir* **2006,** *22* (22), 9368-9374.

134.   Kim, C.; Jeong, Y. I.; Ngoc, B. T.; Yang, K. S.; Kojima, M.; Kim, Y. A.; Endo, M.; Lee, J. W., Synthesis and Characterization of Porous Carbon Nanofibers With Hollow Cores Through the Thermal Treatment of Electrospun Copolymeric Nanofiber Webs. *Small* **2007,** *3* (1), 91-95.

135.   Ji, L.; Saquing, C.; Khan, S. A.; Zhang, X., Preparation and characterization of silica nanoparticulate-polyacrylonitrile composite and porous nanofibers. *Nanotechnology* **2008,** *19* (8), 085605.

136.   Wang, L. F.; Pai, C. L.; Boyce, M. C.; Rutledge, G. C., Wrinkled surface topographies of electrospun polymer fibers. *Appl. Phys. Lett.* **2009,** *94* (15), 151916.

137.   Arshad, S. N.; Naraghi, M.; Chasiotis, I., Strong carbon nanofibers from electrospun polyacrylonitrile. *Carbon* **2011,** *49* (5), 1710-1719.

138.   Naraghi, M.; Chasiotis, I.; Kahn, H.; Wen, Y.; Dzenis, Y., Novel method for mechanical characterization of polymeric nanofibers. *Review of Scientific Instruments* **2007,** *78* (8), 085108.

139.   Peng, Y. T.; Lo, C. T., Electrospun porous carbon nanofibers as lithium ion battery anodes. *Journal of Solid State Electrochemistry* **2015,** *19* (11), 3401-3410.

140.   Liu, Y. D.; Kumar, S., Recent Progress in Fabrication, Structure, and Properties of Carbon Fibers. *Polym Rev* **2012,** *52* (3-4), 234-258.

141.   <ANotherReviewNotveryUseful.pdf>.

142.   Sing, K., The use of nitrogen adsorption for the characterisation of porous materials. *Colloids and Surfaces a-Physicochemical and Engineering Aspects* **2001,** *187*, 3-9.

143.   Wang, Y.; Serrano, S.; Santiago-Aviles, J. J., Raman Characterization of Carbon Nanofibers Prepared Using Electrospinning. *Synthetic Metals* **2003,** *138* (3), 423-427.

144.   Zussman, E.; Chen, X.; Ding, W.; Calabri, L.; Dikin, D. A.; Quintana, J. P.; Ruoff, R. S., Mechanical and structural characterization of electrospun PAN-derived carbon nanofibers. *Carbon* **2005,** *43* (10), 2175-2185.

145.   Kim, C.; Park, S. H.; Cho, J. K.; Lee, D. Y.; Park, T. J.; Lee, W. J.; Yang, K. S., Raman Spectroscopic Evaluation of Polyacrylonitrile-Based Carbon Nanofibers Prepared by Electrospinning. *Journal of Raman Spectroscopy* **2004,** *35* (11), 928-933.

146.   Dai, L. C.; Guo, W. L.; Wang, X., Stress concentration at an elliptic hole in transversely isotropic piezoelectric solids. *International Journal of Solids and Structures* **2006,** *43* (6), 1818-1831.

147.   Naraghi, M.; Chawla, S., Carbonized Micro- and Nanostructures: Can Downsizing Really Help? *Materials (Basel)* **2014,** *7* (5), 3820-3833.

148.   Penev, E. S.; Artyukhov, V. I.; Yakobson, B. I., Basic structural units in carbon fibers: Atomistic models and tensile behavior. *Carbon* **2015,** *85*, 72-78.

149.   Reynolds, W. N.; Sharp, J. V., Crystal Shear Limit to Carbon-Fiber Strength. *Carbon* **1974,** *12* (2), 103-110.

150.   Tagawa, T.; Miyata, T., Size Effect on Tensile Strength of Carbon Fibers. *Materials Science and Engineering A* **1997,** *238* (2), 336-342.

151.   Chen, X. D.; Wu, S. X.; Zhou, J. K., Influence of porosity on compressive and tensile strength of cement mortar. *Constr Build Mater* **2013,** *40*, 869-874.

152.   Balshin, M. Y. In *Relation of Mechanical Properties of Powder Metals and Their Porosity and the Ultimate Properties of Porous Metal-Ceramic Materials*, Doklady Akademii Nauk SSSR, 1949; pp 831-834.

153. Ryshkewitch, E., Compression Strength of Porous Sintered Alumina and Zirconia .9. To Ceramography. *Journal of the American Ceramic Society* **1953,** *36* (2), 65-68.

154. Hasselman, D. P., Griffith Flaws and Effect of Porosity on Tensile Strength of Brittle Ceramics. *Journal of the American Ceramic Society* **1969,** *52* (8), 457-+.

155. Haynes, R., Effect of Porosity Content on the Tensile Strength of Porous Materials. *Powder Metallurgy* **2014,** *14* (27), 64-70.

156. Gibson, L. J.; Ashby, M. F., *Cellular solids: structure and properties*. Cambridge university press: 1999.

157. Soden, P. D.; Hinton, M. J.; Kaddour, A. S., Lamina Properties, Lay-Up Configurations and Loading Conditions for a Range of Fibre-Reinforced Composite Laminates. *Compos. Sci. Technol.* **1998,** *58* (7), 1011-1022.

158. Gjermo, P.; Baastad, K. L.; Rolla, G., The plaque=inhibiting capacity of 11 antibacterial compounds. *J Periodontal Res* **1970,** *5* (2), 102-9.

159. Simoncic, B.; Tomsic, B., Structures of Novel Antimicrobial Agents for Textiles - A Review. *Textile Research Journal* **2010,** *80* (16), 1721-1737.

160. Washburn, E. W., The dynamics of capillary flow. *Phys Rev* **1921,** *17* (3), 273-283.

161. Jud, K.; Kausch, H. H.; Williams, J. G., Fracture-Mechanics Studies of Crack Healing and Welding of Polymers. *J Mater Sci* **1981,** *16* (1), 204-210.

162. Chen, M.; Li, Y. F.; Besenbacher, F., Electrospun nanofibers-mediated on-demand drug release. *Adv Healthc Mater* **2014,** *3* (11), 1721-32.

163.   Altinbasak, I.; Jijie, R.; Barras, A.; Golba, B.; Sanyal, R.; Bouckaert, J.; Drider, D.; Bilyy, R.; Dumych, T.; Paryzhak, S.; Vovk, V.; Boukherroub, R.; Sanyal, A.; Szunerits, S., Reduced Graphene-Oxide-Embedded Polymeric Nanofiber Mats: An "On-Demand" Photothermally Triggered Antibiotic Release Platform. *ACS Appl Mater Interfaces* **2018,** *10* (48), 41098-41106.

164.   Tamayol, A.; Hassani Najafabadi, A.; Mostafalu, P.; Yetisen, A. K.; Commotto, M.; Aldhahri, M.; Abdel-Wahab, M. S.; Najafabadi, Z. I.; Latifi, S.; Akbari, M.; Annabi, N.; Yun, S. H.; Memic, A.; Dokmeci, M. R.; Khademhosseini, A., Biodegradable elastic nanofibrous platforms with integrated flexible heaters for on-demand drug delivery. *Sci Rep* **2017,** *7* (1), 9220.

165.   Mostafalu, P.; Kiaee, G.; Giatsidis, G.; Khalilpour, A.; Nabavinia, M.; Dokmeci, M. R.; Sonkusale, S.; Orgill, D. P.; Tamayol, A.; Khademhosseini, A., A Textile Dressing for Temporal and Dosage Controlled Drug Delivery. *Adv. Funct. Mater.* **2017,** *27* (41).

166.   Wang, B.; Zheng, H.; Chang, M. W.; Ahmad, Z.; Li, J. S., Hollow polycaprolactone composite fibers for controlled magnetic responsive antifungal drug release. *Colloids Surf B Biointerfaces* **2016,** *145*, 757-767.

167.   Kim, Y.-J.; Ebara, M.; Aoyagi, T., A Smart Hyperthermia Nanofiber with Switchable Drug Release for Inducing Cancer Apoptosis. *Adv. Funct. Mater.* **2013,** *23* (46), 5753-5761.

168.   Arrhenius, S., Über die Dissociationswärme und den Einfluss der Temperatur auf den Dissociationsgrad der Elektrolyte. *Zeitschrift für physikalische Chemie* **1889,** *4* (1), 96-116.

169. Laidler, K. J., The development of the Arrhenius equation. *J Chem Educ* **1984,** *61* (6), 494.

170. Noimark, S.; Bovis, M.; MacRobert, A. J.; Correia, A.; Allan, E.; Wilson, M.; Parkin, I. P., Photobactericidal polymers; the incorporation of crystal violet and nanogold into medical grade silicone. *Rsc Adv* **2013,** *3* (40), 18383-18394.

171. Boulos, R. A., Antimicrobial dyes and mechanosensitive channels. *Antonie Van Leeuwenhoek* **2013,** *104* (2), 155-67.

172. Pohlmann, A. R.; Fonseca, F. N.; Paese, K.; Detoni, C. B.; Coradini, K.; Beck, R. C.; Guterres, S. S., Poly(-caprolactone) microcapsules and nanocapsules in drug delivery. *Expert Opin Drug Deliv* **2013,** *10* (5), 623-38.

173. Swinehart, D., The beer-lambert law. *J Chem Educ* **1962,** *39* (7), 333.

174. Agari, Y.; Ueda, A., Thermal-Conductivity of Poly(Vinyl Chloride) Polycaprolactone Blends. *J. Polym. Sci. Pt. B-Polym. Phys.* **1994,** *32* (1), 59-62.

175. Siepmann, J.; Siepmann, F., Modeling of diffusion controlled drug delivery. *J Control Release* **2012,** *161* (2), 351-62.

176. Siepmann, J.; Siepmann, F., Mathematical modeling of drug delivery. *Int J Pharm* **2008,** *364* (2), 328-43.

177. Fundamentals and Applications of Controlled Release Drug Delivery.

178. Controlled Release A Quantitative Treatment.

179. The Mathematics of Diffusion.

180.   Siparsky, G. L.; Voorhees, K. J.; Dorgan, J. R.; Schilling, K., Water transport in polylactic acid (PLA), PLA/ polycaprolactone copolymers, and PLA/polyethylene glycol blends. *Journal of environmental polymer degradation* **1997,** *5* (3), 125-136.

181.   Dole, P.; Feigenbaum, A. E.; De La Cruz, C.; Pastorelli, S.; Paseiro, P.; Hankemeier, T.; Voulzatis, Y.; Aucejo, S.; Saillard, P.; Papaspyrides, C., Typical diffusion behaviour in packaging polymers - application to functional barriers. *Food Addit Contam* **2006,** *23* (2), 202-11.

182.   Zhang, S. L.; Pan, N., Supercapacitors Performance Evaluation. *Adv. Energy. Mater.* **2015,** *5* (6).

183.   Stoller, M. D.; Ruoff, R. S., Best practice methods for determining an electrode material's performance for ultracapacitors. *Energy Environ. Sci.* **2010,** *3* (9), 1294-1301.

184.   Wang, J. C.; Kaskel, S., KOH activation of carbon-based materials for energy storage. *J. Mater. Chem.* **2012,** *22* (45), 23710-23725.

185.   Chiang, Y. C.; Lee, C. Y.; Lee, H. C., Surface chemistry of polyacrylonitrile- and rayon-based activated carbon fibers after post-heat treatment. *Mater. Chem. Phys.* **2007,** *101* (1), 199-210.

186.   Bleda-Martinez, M. J.; Macia-Agullo, J. A.; Lozano-Castello, D.; Morallon, E.; Cazorla-Amoros, D.; Linares-Solano, A., Role of surface chemistry on electric double layer capacitance of carbon materials. *Carbon* **2005,** *43* (13), 2677-2684.

187.   Zhi, M. J.; Yang, F.; Meng, F. K.; Li, M. Q.; Manivannan, A.; Wu, N. Q., Effects of Pore Structure on Performance of An Activated-Carbon Supercapacitor Electrode Recycled from Scrap Waste Tires. *ACS Sustainable Chem. Eng.* **2014,** *2* (7), 1592-1598.

188.   Gamby, J.; Taberna, P. L.; Simon, P.; Fauvarque, J. F.; Chesneau, M., Studies and characterisations of various activated carbons used for carbon/carbon supercapacitors. *J. Power Sources* **2001,** *101* (1), 109-116.